X-ray Phase-Contrast multiscale-Tomography for the 3D quantitative investigation of the spinal cord neuronal arrangements for preclinical application

Michela Fratini[a,b], Inna Bukreeva[b], Gaetano Campi[c], Francesco Brun[a], Peter Modregger[d], Maddalena Mastrogiacomo[f], Herwig Requardt[g], Federico Giove[h] , Alberto Bravin[g] & Alessia Cedola[a]

[a]Istituto di Nanotecnologia-Laboratorio di Soft and Living Matter, CNR, Roma ,00195, Italia
[b]IRCCS Fondazione Santa Lucia,Roma, 00144, Italia
[c]Istituto di Cristallografia, CNR, Monterotondo Roma, 00015, Itallia.
[d]Swiss Light Source, Paul Scherrer Institut, Villigen, 5232, Switzerland & Centre d'Imagerie BioMedicale, Ecole Polytechnique Federale de Lausanne, Lausanne,1015 ,Switzerland
[f]Dipartimento di Medicina Sperimentale, Università di Genova, Genova, 16132 Italia
[g]European Synchrotron Radiation Facility, ESRF, Grenoble, 38043, France,
[h] Museo Storico della Fisica e Centro Studi e Ricerche Enrico Fermi, Roma , 00184, Italia

e-mail: michela.fratini@gmail.com

Keywords: (X-ray phase contrast Tomography, neuronal network, spatial statistical analysis, motorneuron)

Major efforts have been focused on the precise anatomical delineation of the neuronal network (NN), which is important for improving our understanding of the effects of pathological processes, such as spinal cord injury or neurodegenerative disease. In this framework, it appears essential to define morphological and topological quantitative parameters characterizing a healthy neuronal network architecture, to understand changes of these features in any part of the central nervous system (CNS) in diseased samples. Indeed, the quantitative analysis of the single elements in different districts is a crucial task. However, conventional 3D imaging techniques do not have enough spatial resolution and contrast to allow for a quantitative investigation of the neuronal network. In order to characterize quantitatively the neuronal network architecture, an improvement in the performance of 3D imaging tools at high spatial resolution is required. Multiple technologies [1-3] have been used to understand the 3D morphology of individual neurons, glia and axons within the brain and the spinal cord (SC). However, up to now, little progress has been made on understanding the arrangement of neurons in 3D space and the functional role of this arrangement, due to the limited field of view and/or low spatial resolution of currently available imaging tools. A recent work demonstrated that X-ray Phase-Contrast multiscale-Tomography allows for simultaneously image the 3D distribution of the small capillary network and of the neuronal network in an entire mouse spinal cord, covering a spatial range from millimeters to hundreds of nanometers without any aggressive sample preparation or sectioning [4]. However, this work provided only a qualitative description of the neuronal microanatomy. A tool for a 3D quantitative imaging of the SC neuronal network would considerably improve our knowledge of the effects of pathological processes, such as spinal SC injuries and neurological diseases. In the literature, several mathematical approaches have been used to quantify the neuronal patterning in 2D [5] and recently for neuroanatomical structures in 3D space [6]. The use of statistical analysis for the investigation of neuronal positioning has been explored extensively in the retina, where some classes of neurons are located with nearly crystalline order [7]. However, statistical analysis has not been applied to the CNS yet. We developed and applied a tool based on a spatial statistical analysis of the motor neurons to obtain quantitative information on their 3D arrangement in the healthy-mice spinal cord. Then, we applied this tool to different SC pathologies, such as injury and multiple sclerosis model. We investigated the healthy-mouse neuronal architecture by imaging the 3D distribution of the neuronal-network with a spatial resolution of 640 nm. Thanks to the high spatial resolution and large field of view, we were able to perform a detailed quantitative analysis of the neuronal network. We analyzed the reconstructed volume of the axial section of the SC ventral horn (about 1 mm thick), reported in figure1. This region includes groups of cells that form motor nuclei in the Lamina IX [8]. Figure 1B,C,D shows the potentiality of the technique: the neuronal network is imaged in sagittal cross section, showing a 500 µm thick volume relative to the selected Region Of Interest (ROI) in the ventral horn (red box in Fig.1A). The longitudinal distribution of white matter and the motor neurons pool (or motor nucleus) in the ventral horn are discernible [8]. Spatial statistical analysis was employed to obtain quantitative information about motor neurons arrangement at different levels of the spinal cord. To this end, we defined the following parameters, to effectively characterize the neurons spatial distribution: 1)*Clustering length and degree*, that tell us whether the neurons are aggregated (clustering) or dispersed (anti-clustering) in comparison to a Complete State of Randomness described by a homogenous Poisson process. 2)A *regularity factor*, given by the Voronoi tessellation, describing whether neurons are located in a more or less uniform way [5]. Since these characteristic parameters of the neuronal microanatomy are expected to change in pathological conditions, we applied the spatial statistical analysis to detect and quantitatively characterize the modification of the motor neurons networks in different pathological system.

1. Denk W. et al. J. Neurosci. Methods 54, 151–162 (1994).
2. Collins C. E., et al. PNAS 107, 15927–15932 (2010).
3. Ertürk A. et al. Nat. Med. 18, 166–171 (2012).
4. Fratini M. et al. Sci. Rep. 5 (2015).]
5. Diggle P. J. Statistical analysis of spatial point patterns. Vol. 2 (Academic-Press, 1983).
6. Leite-Almeida H. et al. J. Neurosci. Meth. 163, 17–23 (2007).
7. Reese B. In Eye, Retina, and Visual Systems of the Mouse (MIT Press 2008).
8. Watson C., Paxinos G. & Kayalioglu G. The spinal cord: a Christopher and Dana Reeve Foundation text and atlas. (Academic press, 2009).

The Italian Ministry of Health Young Researcher Grant 2013 (GR-2013-02358177) and European project VOXEL (HORIZON 2020-Fet Open; Project reference: 665207) are acknowledged for financial support

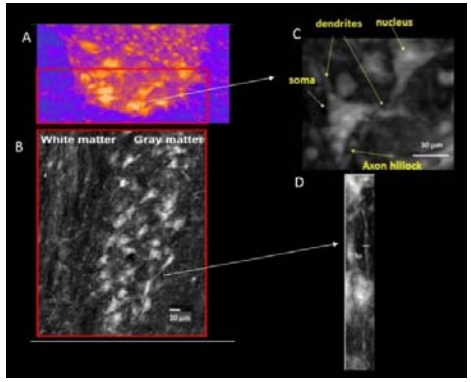

Figure 1. (A) Axial cross section of the spinal cord ventral horn at the thoracic level. The image was segmented to show the neurons (dark yellow) and the neuron fibers (light violet). (B) 500 μm thick volume in sagittal view, of the spinal cord relative to the selected ROI in (A) (red box). (C) A magnified image of one neuron fiber connection selected in a motor nucleus. (D) A magnification of the interaction between two motor neurons in the red box in A

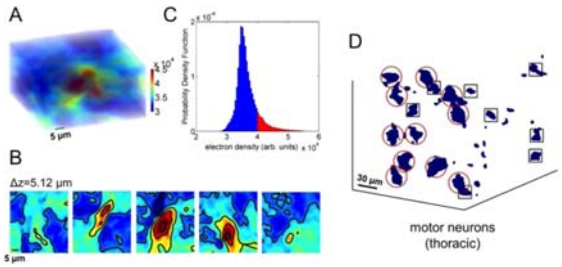

Figure 2. (A) Rendering of the electronic density of a typical single motor neuron in the thoracic region. (B) The contour plots identify the nucleus (region with higher intensity) in the (A) slabs sectioned at different levels. Each slice corresponds to a thickness of 5.12 µm. (C) The Probability density distribution of the motor neurons. The red areas represent values of density searched by the positioning algorithm (see Methods). (D) 3D spatial arrangement of motor neurons in a volume of about 0.5 × 107 µm3 in the thoracic spinal cord region. We note different size populations allowing us to distinguish the motor neurons (enclosed in red circles) from other cells whose size is compatible with glia (enclosed in black squares)

Study of the spinal cord and brainstem functional activation in response to a controlled motor task using fMRI

Laura Maugeri[a], Marta Moraschi[b], P. Summers[c], S. Favilla[c], A. Cedola[d] C.A. Porro[c]
Michela Fratini[a,d], Federico Giove[b],
[a] Fondazione Santa Lucia IRCCS, Rome, 00179, Italy
[b] Museo Storico della Fisica e Centro Studi e Ricerche Enrico Fermi, Rome, 00184, Italy
[c], University of Modena and Reggio Emilia, 41125 Modena, Italy
[d] CNR-NANOTEC , Rome 00185, Italy
e-mail: maugeri83@gmail.com
Keywords: (Spinal cord, brainstem, isometric motor task, fMRI, motor pathway, physiological artefacts)

Functional Magnetic Resonance Imaging (fMRI) has become one of the most powerful tools in neuroscience research, with fMRI based on BOLD (Blood Oxygen level dependent) contrast [1,2] having gained a primary role in the study of human brain, both for the characterization of its activity in physiological conditions and playing an increasing role in clinical practice. Moreover, several fMRI studies of the human Spinal Cord (SC) and Brainstem in response to thermal, sensory, motor and painful stimuli have been reported [3-5], and substantial efforts have been devoted to develop appropriate methodologies [6]. Nonetheless, the application of fMRI to the SC and Brainstem remains confined to a few laboratories,
Brainstem and SC fMRI may be of immediate application in neuroradiology, specifically for the assessment and follow-up of spinal injuries, pain, and neurodegenerative diseases, as well as for the development and evaluation of new therapies. Indeed, a non-invasive tool capable of monitoring neural function, and thus complementing the available structural information, is crucially needed in these fields.
Preliminary studies of people with SC injury and multiple sclerosis have demonstrated altered activity in the brainstem and in the SC depending on the injury severity or disease state [7,8]. From the clinical perspective however, it is important to recognize that SC fMRI has been demonstrated for group analyses but there are still sources of variability or uncertainty that count against its use for individual studies. Once these sources of variability and errors are characterized and understood, it is expected that methods can be adapted to optimize the sensitivity of SC fMRI in the study and assessment of individuals.
The vagaries of the SC and brainstem fMRI activation patterns and of their characteristics can be explained, at least in part, by a poor control of physiological noise [9] and the limited overall quality of the functional series, due to geometrical distortion, signal loss, and poor contrast to noise ratio. The relevant solutions can be found in the combination of optimized experimental procedures at acquisition stage, and well-adapted procedures in post-processing. In this framework, we have developed an analysis protocol to study the motor pathway activation on spinal cord (SC) and Brainstem, aimed to solve some of the problems related to physiological and movements artifacts in SC and Brainstem fMRI. The study, performed in healthy subjects, was carried out using an ad hoc isometric motor task.
fMRI data were acquired using a neurovascular coil array, on a 3T scanner (Achieva, Philips Medical Systems, Best, The Netherlands). Healthy subjects (15 for SC fMRI and 7 for Brainstem fMRI) performed a block-designed motor task. Subjects were asked to press a force-sensitive device between their first and second finger, until a visual feedback confirmed that the target force was reached. Each run included alternating 30s rest and motor task epochs, during which target forces of either 10%, 20% or 50% of the subject's own maximal sustained force (MSF) were required in a pseudorandom order. The actual developed force was digitized and recorded. For each subject, 3 gradient-echo EPI runs were acquired (TE=25 ms, flip angle 75°, TR=2500ms, 20 parasagittal slices, 1.5 mm thick). fMRI data underwent optimized image pre-processing protocol (RETROICOR [9] and CompCor physiological noise reduction [10], masking, motion correction, slice timing, smoothing). (figure1)

In particular, we review two model-based approaches to remove the physiological noise, that rely on externally acquired respiratory and cardiac signals (RETROICOR) as well as data-driven approaches (ComCor) that estimate and correct for noise using the data themselves and without the need of recording physiological parameters. Subject specific activations were obtained by using a statistical analysis based on a general linear model (GLM). A GLM fitting was realized by using realignment parameters, denoising components and force parameters as confounding variables and a t-test was carried out by choosing as threshold a p_value of 0.001. In this way, voxels whose p-values are below 0.001 are color-coded to signify that they contain significant task-related signal. Custom Matlab routines incorporating spm8 and afni functions were used. We found a congruent task-related fMRI response in SC and Brainstem networks. Brainstem itself is an intermediate center of the motor system, receiving input from the cerebral cortex and sending pathways to spinal cord circuits. Thus, Brainstem data are of support for the study of the spinal cord activation.
Positive signal changes were mostly detected at C4–C7 vertebral levels (figure2A) and in the Brainstem and cerebral cortex (fig2B).

[1] Ogawa, S., et al.,. Proc Natl Acad Sci U S A 87 (24):, (1990) 9868-72.
[2] Logothetis, N.K., et al., Nature 412 (6843), 2001. 150-157.
[3]Stroman PW, et al. Magnetic Resonance Imaging 26 (2008) 809–814.
[4] Stroman PW. Magnetic resonance imaging 2009; 27(10):1333-2.
[5] Maieron M, et al. The Journal of neuroscience: the official journal of the Society for Neuroscience 2007;27(15):4182-4190
[6] Stroman, P.W., et al., Neuroimage, 2014. 84: p. 1070-1081.
[7] Stroman, Patrick W., et al. Journal of neurotrauma 33.15 (2016): 1450-1460.
[8] Wheeler-Kingshott, C., et al,. Neuroimage, 2014. 84: p. 1082-1093.
[9]Fratini, M., et al., Journal of Magnetic Resonance Imaging, 2014. 40(4): p. 770-777.
[10]Behzadi Y. et al., NeuroImage, 2007. 37: p 90-101.

The Italian Ministry of Health Young Researcher Grant 2013 (GR-2013-02358177) is acknowledged for financial support

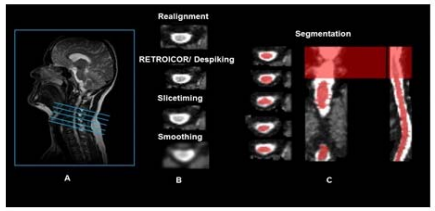

Figure 1: Preprocessing protocol_ Script Development for the data analysis *ad hoc* for the spinal cord and brainstem

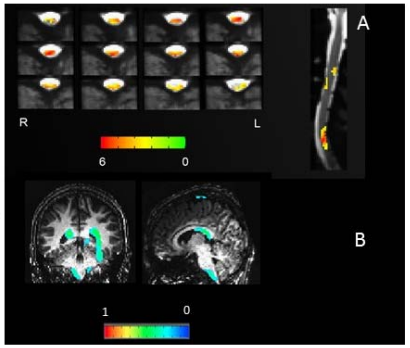

Figure 2: Activation maps of representative subjects (A) at lower cervical level and in the brainstem and in the cortex (B) during a graded isometric force

Assessment of cancellous bone quality through NMR diffusion measurement of water in trabecular bone microstructure and bone marrow fatty acids quantification

Silvia Capuani

CNR ISC Roma Sapienza, Physics Department Sapienza University of Rome, Rome, 00185, Italy

e-mail: silvia.capuani@roma1.infn.it

Keywords: NMR, water diffusion, bone, osteoporosis, bone marrow

Progress in understanding the pathogenesis of bone fragility and in performing a correct osteoporosis diagnosis is hampered by the poor accessibility of bone for microstructural investigation in vivo. Bone densitometry performed by means of dual-energy x-ray absorptiometry, is a noninvasive and low cost method for the quantification of bone mineral density (BMD), but it cannot provide information about trabecular bone rearrangement and organic components, that are details strictly linked to bone strength [1,2].

Even though BMD has been the accepted standard for osteoporosis diagnosis, it has a low predictive value on patients' risk for future fractures [2]. More specifically, bone strength is determined by the overall bone quality, a term that incorporates all the factors that determine how well the skeleton can resist fracturing, such as microarchitecture, accumulated microscopic damage, the quality of collagen and bone marrow, the size of mineral crystals, the physiologic activity of the skeletal cells and the rate of bone turnover [3].

Thus, new approaches for investigating subjects at risk for developing osteoporosis would be desirable.

In this regard, Magnetic Resonance (MR) diffusion weighted imaging (DWI) methodologies allow in vivo investigation of microstructural tissue features, by probing biological water motion on the micrometer length scale, which is orders of magnitude smaller than the macroscopic DWI image resolution.

Recently, a porous system model suitable for investigating the microstructural proprieties of cancellous bone by diffusion MR Imaging was described and corroborated by experiments [4-7]. The model is based on the schematic representation for which bone marrow water is more prevalent in the boundary zone while fat occupies primarily the central zone of each cancellous bone pore. Moreover, to better understand the mechanisms underlining osteoporosis development, bone marrow fatty acids are quantified [8].

In this work, Magnetic Resonance diffusion measurements were performed at 3T magnetic field in 60 woman (aged 22-75 y) characterized by different BMD (classified as healthy, osteopenic and osteoporotic subjects) and correlation between diffusion parameters, marrow fatty acids content (Mfc), BMD, and subjects' age were investigated. Monte Carlo simulations of water diffusion in different synthetic trabecular bone structures were conducted to elucidate the influence of magnetic susceptibility and Mfc on diffusion measurement in bone and corroborate clinical results. This investigation, which aims at finding an effective method for early osteoporosis diagnosis, is carried out in collaboration with orthopedic, physiologists and radiologists of Tor Vergata University, IRCCS Santa Lucia of Rome and Pennsylvania University (USA).

[1] Kanis JA. Diagnosis of osteoporosis and assessment of fracture risk. Lancet 2002;359:1929-1936.
[2] Stone K, et al. BMD at multiple sites and risk of fracture of multiple types: long-term results from the study of osteoporotic fractures. J Bone Miner Res 2003;18:1947–54.
[3] Ego Seeman, and Pierre D. Delmas. Bone Quality. N Engl J Med 2006; 354:2250-2261
[4] Capuani S. Diffusion in cancellous bone. Micropor Mesopor Mater 2013;178:34.
[5] Manenti G, Capuani S, et al. Diffusion tensor imaging and magnetic resonance spectroscopy assessment of cancellous bone quality in femoral neck of healthy, osteopenic and osteoporotic subjects at 3T: Preliminary experience Bone 2013;55:7.
[6] Rebuzzi M, Vinicola V, Taggi F, Sabatini U, Wehrli FW, Capuani S. Potential diagnostic role of the MRI-derived internal magnetic field gradient in calcaneus cancellous bone for evaluating postmenopausal osteoporosis at 3T. Bone 2013;57:155.
[7] Capuani S et al. Focus on Diffusion MR Investigations of Musculoskeletal Tissue to Improve Osteoporosis Diagnosis: A Brief Practical Review. BioMed Research International 2015; Article ID 948610.
[8] G. Di Pietro, S. Capuani et al. Bone Marrow Lipid Profiles from Peripheral Skeleton as Potential Biomarkers for Osteoporosis: A 1H-MR Spectroscopy Study. Acad Radiol. 2016; 23:273–283.

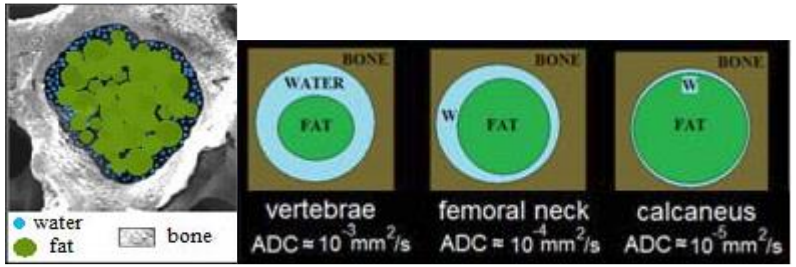

Figure 1 - The porous model suitable for obtaining microstructural information in cancellous bone by using diffusion. ADC is the apparent diffusion coefficient quantified by diffusion weighted MR tecniques

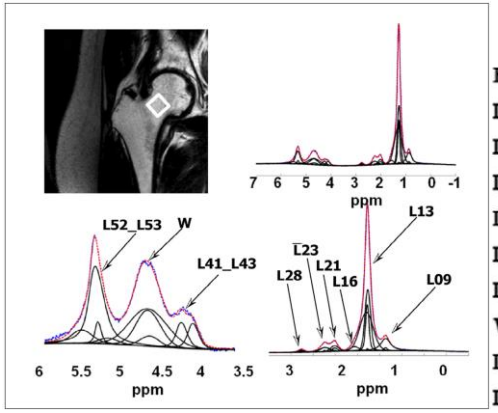

Resonance acronym	and name
L09	methyl protons
L13	methylene protons
L16	methylene protons β to COO
L21	methylene protons α to C=C
L23	methylene protons α to COO
L28	diallylic methylene protons
W	Water
L41 and L43	Glycerol
L52 and L53	Olefinic double bond protons

Figure 2 - Example of 1H-MRS spectra obtained in femoral neck of healthy subject and lipid quantification The T2-weighted image of femur shows the position of voxel (white square) used to collect spectra

Table 1
MR data in calcaneus and femoral neck of healthy, osteopenic and osteoporotic group

Parameter	Skeletal site	1 (H)	2 (OPE)	3 (OPO)	*P* Value (1 vs 2)	*P* Value (2 vs 3)	*P* Value (1 vs 3)
Mfc (%)	Calcaneus	86.44±4.70	88.01±3.32	87.50±2.00	ns	ns	ns
ADC ($*10^{-10}$ m^2/s)	Calcaneus	0.40±0.08	0.52±0.15	0.68±0.16	**	*	***
Mfc(%)	Femoral neck	73.42±5.34	80.14±7.78	83.86±4.94	*	ns	***
ADC ($*10^{-10}$ m^2/s)	Femoral neck	4.12±0.56	2.12±1.14	2.15±0.41	***	ns	***

Data are mean ±SD. n=number of subjects. ns ($P \geq 0.05$); *($P < 0.05$); **($P < 0.01$); ***($P < 0.001$).

Reduced gliotransmitter release from astrocytes mediates tau-induced synaptic dysfunction in cultured hippocampal neurons

Roberto Piacentini[1], Domenica Donatella Li Puma[1], Marco Mainardi[1], Giacomo Lazzarino[2],

Barbara Tavazzi[2], Ottavio Arancio[3], Claudio Grassi[1]

[1] Institute of Human Physiology, Università Cattolica, 00168, Rome, Italy
[2] Institute of Biochemistry and Clinical Biochemistry, Università Cattolica, 00168, Rome, Italy
[3] Department of Pathology and Cell Biology and Taub Institute for Research on Alzheimer's Disease and the Aging Brain, Columbia University, New York, 10032 USA
e-mail: roberto,piacentini@unicatt.it

Keywords: (Tau, astrocytes, ATP, synaptic transmission, synaptic proteins, Alzheimer's Disease)

Tau is a microtubule-associated protein exerting several physiological functions in neurons, however increasing evidence demonstrate the pivotal role of tau in Alzheimer's disease (AD) pathogenesis [1]. Hyperphosphorylated and misfolded tau accumulates intraneuronally and acts destroying axons, thus contributing to neuronal loss in AD. Tau protein has been also found in extracellular medium. We and other groups demonstrated that extracellular oligomeric tau (ex-oTau) exerts a strong synaptotoxic action [1,2]. Indeed, it may cross neuronal membranes and impair synaptic plasticity at the CA3-CA1 synapse in mouse hippocampal brain slices, as well as hippocampal-dependent memory in mice [2], thus suggesting that ex-oTau synaptotoxicity may depend on internalization and intracellular accumulation in neurons. However, tau has also been found accumulated in cells others than neurons, such as astrocytes and microglia [3]. Astrocytes have the ability of orchestrate synaptic plasticity and synaptic transmission. As part of the "tripartite synapse" they respond to synaptic activity and regulate synaptic transmission by buffering excess of glutamate and releasing gliotransmitters such as glutamate, ATP and D-serine in a Ca^{2+}-dependent fashion.

Here we report novel evidence that ex-oTau is abundantly and rapidly accumulated in astrocytes where they disrupt intracellular Ca^{2+} signaling and Ca^{2+}-dependent release of gliotransmitters, especially ATP. Consequently, synaptic vesicle release, the expression of pre- and post-synaptic proteins, and miniature Excitatory Post Synaptic Current (mEPSC) frequency and amplitude were reduced in neighbouring neurons. Notably, tau uploading from astrocytes required the amyloid precursor protein, APP.

Indeed, we found that: **i)** oTau accumulates more rapidly and abundantly in astrocytes than in neurons while it exerts its toxicity at synaptic level (Fig. 1 and 3). In fact, after 1-h ex-oTau application synaptic vesicular release (studied by FM1-43 imaging) and basal synaptic transmission (studied by patch-clamp recordings) were significantly depressed, and the expression of the synaptic proteins synaptophysin, synapsin and GluR1(studied by Western Blot) was reduced; **ii)** 1-h ex-oTau application reduces ATP-induced intracellular Ca^{2+} waves (studied by Ca^{2+} imaging) and Ca^{2+}-dependent gliotransmitter release, with ATP being the most affected one (Fig. 2). In fact, ATP levels (quantified by HPLC) were reduced by 73±7% respect to vehicle-treated cultures (from 93±27 to 28±13 nM; $P<0.01$). Conversely, ADP levels increased significantly following tau treatment (+28±13%; $P<0.05$); **iii)** synaptotoxic effects induced by oTau are reverted by exogenous ATP (Fig. 3); **iv)** when oTau is applied to wild-type neurons grown on astrocytes unable to upload tau (APP-KO) it does not exert any synaptotoxic effects (Fig. 4).

Collectively, our findings suggests that astrocytes play a critical role in the synaptotoxic effects of tau via reduced gliotransmitter availability, and that astrocytes are major determinants of tau pathology in AD.

References: [1] Guerrero-Muñoz MJ et al. 2015. Front Cell Neurosci. 9:464; [2] Fá M et al. 2016. Sci Rep. 6:19393; [3] Kahlson&Colodner 2015. J Exp Neurosci. 9: 43–50;

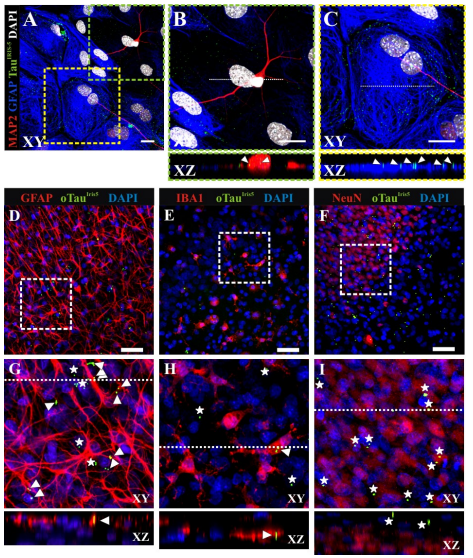

Figure 1. *Tau protein enters more efficiently astrocytes than neurons*

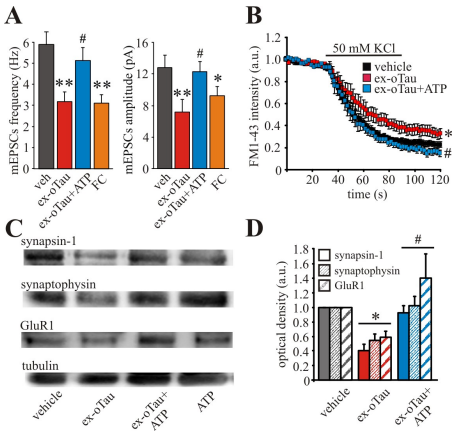

Figure 3. *Tau treatment affects basal synaptic transmission and its action is reverted by ATP*

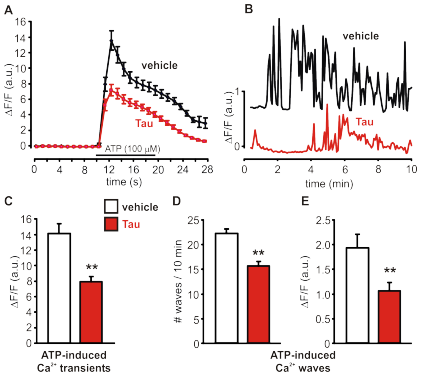

Figure 2. *Tau treatment affects ATP-induced intracellular Ca^{2+} transients and Ca^{2+} waves.*

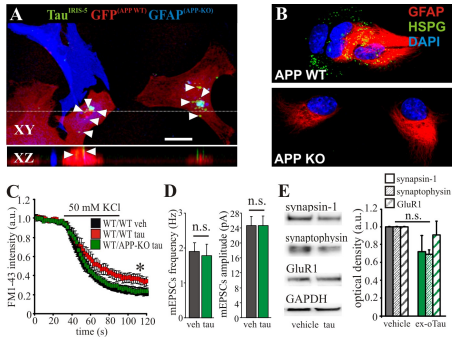

Figure 4. *Ex-oTau synaptotoxicity depends on its ability to be uploaded from astrocytes.*

Airway mucus microenvironment modelling to be applied on cystic fibrosis drug discovery

Petrini P[a], Pacheco DP[a], Pontremoli C. 3[b], Caron G.[c], Visentin S.[c]

[a] Dipartimento di Chimica, Materiali e Ingegneria Chimica, Politecnico di MilanoMilano, 20133, Italy
[b] Dipartimento di Scienza Applicata e Tecnologia (DISAT), Politecnico di Torino, Torino, 10129, Italy
[c] Department of Molecular Biotechnology and Health Science, Torino, 10125, Italy
e-mail: sonja.visentin@unito.it

Keywords: (mucus , drugs , cystic fibrosis, mucin)

Introduction

Cystic fibrosis (CF) is the most common life-threatening autosomal recessive genetic disease in pediatric age. CF is caused by mutations in the transmembrane conductance regulator (CFTR) gene encoding for an ion channel located on the apical membrane of lung epithelial cells.

Most of the health problems experienced by CF patients arise from the overproduction of the thick mucus (mucus is composed of water, ions, lipids, and approximately 2% of proteins: the protein mainly expressed is mucin, a high molecular O-glycosylated protein). These thick, sticky secretions plug up the ducts (small tubes) that should carry the secretions either outside of the body or into a hollow organ such as the lungs or the intestines. This can affect vital body functions such as breathing or digestion. There is no cure for CF, but pharmaceutical developments envisioned to tackle mucus accumulation/obstruction and CFTR-targeted therapies have improved average life expectancy of CF patients. Over the past decade, advanced technologies have enabled high throughput screening (HTS) approaches to drug discovery that yielded orally bioavailable small molecule compounds capable of targeting the underlying defect. CFTR modulators are designed to treat the underlying cause of cystic fibrosis by targeting the CFTR protein defect. Small molecule pharmacologic agents that target defects in CFTR gating, processing, and synthesis have undergone rigorous preclinical and clinical evaluation over the past decade and include CFTR potentiators (e.g. VX-770 also known as ivacaftor), correctors (e.g.VX-809 also known as lumacaftor), and translational read-through agents (aminoglycoside antibiotics e.g. gentamicin, tobramycin).

Although the encouraging results of pharmaceutical companies, mucus overproduction remains the major factor determining drug efficacy in CF patients. In fact, orally taken systemic drugs must pass through the gastrointestinal mucus barrier, whereas inhaled drugs must pass through airway mucus and their pulmonary deposition to reach their targets.

The need to characterize drug behavior in a rapid, simple and reproducible manner has urged the development of airway mucus models. In this work, an airway mucus model composed by alginate and mucin is herein proposed aiming to model both composition and rheological properties of the pathologic CF-mucus.

Material and Methods

Alginate (alginic acid sodium salt, from brown algae)/mucin (from porcine stomach, type III) hydrogels were developed taking advantage of the internal crosslinking mechanism of alginate, in the presence of NaCl (final concentration 7 mM). Rheological measurements were carried out to access the viscoelastic and shear thinning behavior of the developed gels and further compared to the pathological CF-mucus. Stability analysis was also conducted to acquire using both water and PBS, at 25 ºC, to analyze changes on weight percentage and volumetric increase. Finally, both drug diffusion and interaction through alginate and alginate/mucin gels were carried out using aspirin, cephalexin and epirubicin, as well as gold nanoparticles (GNP) as model drugs.

Results and Discussion

Hydrogels composed by alginate and mucin were developed. As observed for CF mucus (1-3), the viscosity of the mucus model decreases with the increasing of shear stress, with no differences observed between both mucus model and CF mucus at both breathing and ciliary beating frequencies. Additionally, no differences on the dissipative modulus were detected between the CF and model mucus, although small differences were detected over storage modulus (1-3). Stability analysis in both water and PBS, at 25°C, revealed an increased weight and size mainly in the early hours. Diffusion studies of drugs and gold nanoparticles through the gels exhibited compositional and structural dependency, thus effecting the interaction with mucin (4,5). The diffusion of drugs was also related to both alginate-drug interactions or steric barrier effect of the gel. Likewise, the diffusion of GNP was hindered by alginate-mucin gels compared to alginate gel, probably related to mesh size of the model.

Conclusion

A mucus model was proposed to study drug permeability in presence of mucus secretion. This platform will serve as the basis to implement the complexity of the model in terms of components, also including the effect of bacteria.

References

1. M. Robinson et al. J. Aerosol Med Pulm Drug Deliv. (2016), 337-345.
2. Y. Shaopeng et al. Sci Transl Med. (2015),1–19.
3. S.K. Lai et al. J.Adv Drug Deliv Rev. (2009), 86-100.
4. G. Caron et al. Int J Pharm. (2015), 67-69.
5. C. Pontremoli et al. Bioorg Med Chem. (2015),6581-6586.

.

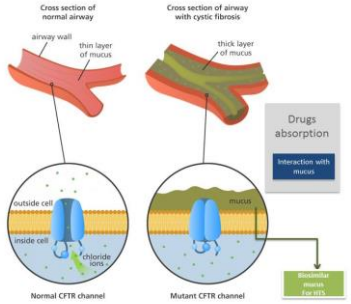

Figure 1 The overproduction of thick, sticky mucus is responsible for the efficacy of drugs used in the treatment of patients affected by CF

Non-Gaussian Diffusion NMR discriminates between low- and high-risk prostate cancer.

Di Trani M.G.[a, b], Caporale A.[a ,c], Nezzo M.[d], Miano R.[e], Mauriello A.[e], Bove P.[e], Manenti G.[d], Capuani S[a].

[a] Physics Dept., CNR ISC UOS, Sapienza University, Rome, 00185, Italy.
[b] SAIMLAL Dept., Morphogenesis and Tissue Engineering, Sapienza University, Rome, 00185, Italy.
[c] SAIMLAL Dept., Morpho-functional Sciences, Sapienza University, Rome, 00185, Italy.
[d] Diagnostic and Interventional Radiology Dept., Tor Vergata University, Rome, 00173, Italy.
[e] Urology Unit, Experimental Medicine and Surgery Dept., Tor Vergata University, Rome, 00173, Italy.
mail: mariagiovanna.ditrani@uniroma1.it

Keywords: (Diffusion NMR, non-Gaussian diffusion, prostate cancer, kurtosis, tissue microstructure, DTI)

Prostate cancer (Pca) is the second most common malignancy and the fifth leading cause of death in men worldwide. Current diagnostic methods, based on PSA measurement and biopsy, are limited by low specificity (36%) and invasive procedures; moreover, 30% of tumor-grade were under-estimated[1]. High-grade PCa is treated with more aggressive therapy, including surgery or radiations, than low-grade PCa; discriminating correctly different tumor grade is mandatory to plan patient treatment. Prostate tissue has a glandular structure, composed by several compartments: acini, formed by secretory cells and connected to ducts; the glandular structure is supported by the connective tissue of stroma.
PCa development is characterized by microstructural modifications, due to the growth of undifferentiated cells and alteration of cell membranes, that change each compartment volume fraction[2].
The Diffusion-weighted NMR (DW-NMR) imaging is sensible to the tumor modifications, since this technique exploits the diffusion of biological water molecules as an endogenous contrast agent.
Diffusion is the stochastic thermally-induced displacement of molecules, that colliding with the structures and barriers they encounter during motion, probe the tissue and reveal its histoarchitecture at microscopic scale, non-invasively. By using a couple of pulsed magnetic-field gradients, the NMR acquired signal, named DW signal, is proportional to the Fourier Transform of molecules motion propagator; if the displacements probability distribution (dpd) is Gaussian-shaped, as it happens in homogeneous media, the signal mono-exponentially decays. Nevertheless, prostate, as any biological systems, is a complex and inhomogeneous media, which exhibits a non-Gaussian diffusion. In order to obtain additional information on tissue microstructures, inaccessible to Gaussian-diffusion NMR technique, we estimate the Kurtosis, i.e. the fourth-order term of the cumulant expansion, that quantifies the deviation of dpd from a Gaussian distribution, providing a measure of tissue heterogeneity[3].
In this work, we compare two NMR technique, Diffusion Tensor Imaging (DTI) and Kurtosis Imaging (DKI), based respectively on Gaussian and non-Gaussian diffusion, to test their diagnostic potential in PCa identification and stadiation.
31 patients with different tumor grades (TG) PCa were enrolled to be examined by a 3T scanner, after two months from the first biopsy. Diffusion-weighted images were acquired with 5 different diffusion weights, i.e. b-values up to 2500s/mm^2. Parametric maps of Mean Diffusivity (MD) and apparent Kurtosis (K) were obtained by using an in-house algorithm developed in Matlab.
One-way ANOVA was performed to test statistical significance of differences in MD and K values calculated in benign prostate and in PCa among different TG. The linear correlation between diffusion parameters and the tumor grade was estimated by the Pearson's test.

Malignant tissue shows a significantly higher K and lower MD values compared to the healthy tissue ($p<10^{-4}$).
K-values of PCa were positively correlated with TG ($r=0.37;p<0.004$), while MD-values were negatively correlated with TG ($r=-0.31;p=0.02$). Both K and MD can significantly discriminate between low- and high-grade PCa; however K showed the highest significance ($p_K=0.005;p_{MD}=0.015$).
These results may be explained considering that, in healthy prostate, water diffusion is almost free in acini and ducts, restricted in stroma and highly restricted in secretory cell layer. The histopathological evidences show that tumor progression causes prostate glands to change in size and shape and malignant cells to infiltrate compartments. The overall effect of these modification lead to a decrease of diffusivity and an increase of heterogeneity.
Our results demonstrate that non-Gaussian diffusion parameter K is more sensitive to tumor-induced microstructural changes, suggesting that DKI could provide a reliable, non-damaging and less expensive diagnostic exam. Since DKI is a non-invasive technique, it also could be employed to follow-up patients, evaluating therapy response.

[1] Ferlay, J. et al., *Int. J. Cancer*, (2015): E359–E386.
[2] Nezzo, M. et al., *European Journal of Radiology*, (2016); 85:1794-1801.
[3] Jensen JH, Helpern JA. *NMR Biomed*, (2010);23:698-710.

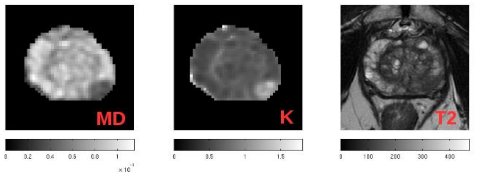

Figure 1. Diffusion parametric maps of Mean Diffusivity (MD, left) and Kurtosis (K, center). In addition, a high-resolution T2-weighted image (T2, right) is showed as anatomical reference.

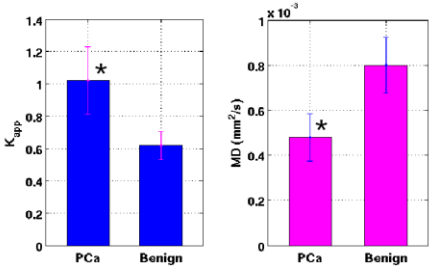

Figure 2. Bar-graphs represent mean value and standard deviation measured in PCa and benign tissue of Kurtosis (left image) and Mean Diffusivity (right image) Statistical significance ($*p<10^{-4}$).

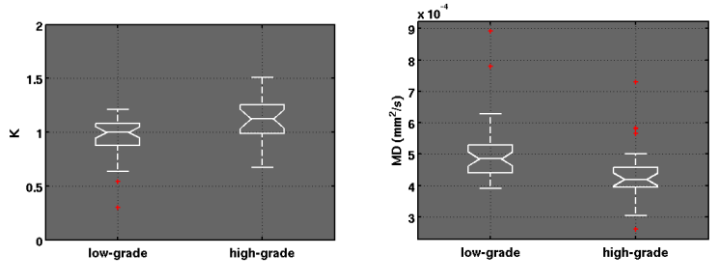

Figure 3. Box-plots represent mean values measured in low- and high-grade PCa of Kurtosis (left image) and Mean Diffusivity (right image).

The anomalous diffusion of biological water provides microstructural and physiological information of brain tissue

Alessandra Caporale[a,b], Marco Palombo[c], Emiliano Macaluso[d], Michele Guerreri[a,e], Marco Bozzali[f], and Silvia Capuani[a]

[a] CNR ISC UOS Roma Sapienza, Sapienza University of Rome, Rome, 00185, Italy
[b] SAIMLAL Dept., Morpho-functional Sciences, Sapienza University of Rome, Rome, Italy
[c] MIRCen, Commissariat à l'Energie Atomique, Fountain Aux Roses, France
[d] ImpAct Team, Lyon Neuroscience Research Center, Lyon, France
[e] SAIMLAL Dept., Morphogenesis & Tissue Engineering, Sapienza University of Rome, Rome, Italy
[f] NeuroImaging Laboratory, Santa Lucia Foundation, Rome, Italy

e-mail: alessandra.stella.caporale@gmail.com

Keywords: anomalous diffusion, magnetic susceptibility, MRI, relaxometry, brain

The purpose of this study is to investigate the capability of Anomalous Diffusion(AD)-MRI technique to provide additional information with respect to the conventional Gaussian diffusion techniques, regarding the microstructure and the physiology of brain tissue.
The spatial arrangement of myelinated fibers in white matter (WM) and the physiological concentrations of iron and iron storage proteins in the cortical and sub-cortical structures in gray matter (GM) cause local differences in magnetic properties among brain regions[1,2], such as magnetic susceptibility differences ($\Delta\chi$). The $\Delta\chi$ distribution may reflect the health state of the brain, practically a combination of myelin integrity and iron balance. Among the MRI parameters the rate of relaxation ($R2^*=1/T2^*$) is pretty sensitive to magnetic field inhomogeneity, and thus to $\Delta\chi$[3,4].
Regarding water diffusion, the conventional diffusion techniques, such as Diffusion Tensor Imaging (DTI) can highlight the anisotropy of myelinated fibers, presenting however a limited sensitivity with respect to tissue microstructure. Indeed, the multiplicity of scale lengths and compartments characterizing brain tissue cause a deviation of water behavior from the prediction of Gaussian diffusion techniques. The AD-MRI refers instead to the Continuous Time Random Walk[5] model, which describes the statistics of water diffusion in complex environments, and it consists in performing a stretched-exponential fitting of Diffusion-Weighted (DW) data, collected at increasing diffusion gradient strengths. We recently highlighted that AD stretched exponent γ quantifies super-diffusion processes[6,7], due to the internal gradients (G_{int}) originated by $\Delta\chi$ at the interfaces between diffusion compartments.
In our study we compared parameters derived from AD-γ maps with R2* in 8 healthy volunteers (4 males/4 females, mean age±SD=25±1years). MRI was performed at 3.0 T at Siemens Allegra Magnetom Scanner (Siemens Medical Solutions, Erlangen, Germany), equipped with a circularly polarized transmit-receive coil. T2*-weighted images (T2*WIs) were collected at TE = (10,20,35,55) ms with Echo Planar Imaging (EPI); DW-images (DWIs) were collected using 20 diffusion directions and b-values (0,100,200,300,400,500,700,800,1000,1500,2000,2500,3000,4000,5000) s/mm^2, with a DW-Double-Spin-Echo-EPI (TR/TE=6400ms/107ms; Δ/δ=72ms/35ms). 32 axial slices 3mm-thick, parallel to the anterior-posterior commissure were acquired in anterior-posterior direction (matrix size=128x128, in-plane resolution=1.8x1.8 mm^2). Signal-to-Noise Ratio of DWIs was approximately 55 for gray matter (GM), 25 for white matter (WM), and it was above 4 for the highest b-value, ensuring the reliability of DW-data[8].
We calculated rotationally invariant γ-metrics (mean-γ, Mγ; axial-γ, γ//; radial-$\gamma\perp$; γ-anisotropy, Aγ), similarly to the DTI approach[9]. We extracted Regions of Interest (ROIs) in WM and GM using atlases in subject's native space (Fig. 1), computing the relative mean values±SD. $\Delta\chi$ values[1] and iron concentrations ([Fe]) of GM ROIs[10] were taken from literature. Pearson's correlation tests were performed, with P-values<0.05 considered as statistically significant.

We found a significant linear correlation between R_2* and the fibers orientation angle Φ in WM (r=-0.381,P<0.0001), and a strong linear correlation (r=-0.950,P=0.05) between R_2* and [Fe] in GM, in agreement with literature[6,7] (Fig. 2), proving that R2* reflected $\Delta\chi$ inhomogeneity in WM and GM, and justifying the study of the dependence of on $\Delta\chi$ through the investigation of its dependence on R_2*.
In both WM ROIs and GM ROIs strong negative correlations between AD-metrics and R2* were found (respectively, in WM Mγ: r=-0.786, P=0.022; γ//: r=-0.822, P=0.012; in GM Mγ: r=-0.997, P=0.003; $\gamma\perp$: r=-0.989, P=0.011), while DTI-metrics did not correlate with R2* (Fig. 3).
Furthermore, we found a negative linear trend between R2*and $\Delta\chi$ in WM ROIs, a positive linear trend in GM ROIs, and an opposite trend of AD-parameters *vs* $\Delta\chi$ compared to R_2* (Fig. 4).
In conclusion this work, confirming results obtained in vitro[3,4], suggested that AD-metrics, differently from DTI, reflects $\Delta\chi$ due to differences in myelin orientation and iron content within selected regions in WM and GM at 3.0 T. This may have a clinical impact in the field of neuroimaging aimed at monitoring both myelin integrity and alterations due to abnormal iron accumulation, which is associated to oxidative stress and neurodegenerative processes in human brain[11].

[1] W. Li et al., Neuroimage 59(3) (2012) 2088-97.
[2] W. Li et al., Neuroimage 55(4) (2014) 1645-1656.
[3] D.A. Rudko et al., PNAS 111(1) (2014) E159-E167.
[4] N.J Gelman et al., Radiology 210(3) (1999) 759-767.
[5] R. Metzler, J. Klafter, Phys. Rep. 339 (2000) 1–77.
[6] M. Palombo et al., JMRI 216 (2012) 28-36.
[7] G. Di Pietro et al. ,App Magn Res 45(8) (2014) 771-784.
[8] D.K. Jones et al., Neuroimage 73 (2013) 239-254.
[9] S. De Santis et al., MRM 64(4) (2011) 1043-1052.
[10] B. Hallgren and P. Sourander J of Neurochem 3(1) (1958) 41-51.
[11] L. Zecca et al., Nature Rev Neurosci 5(11) (2004) 863-873.

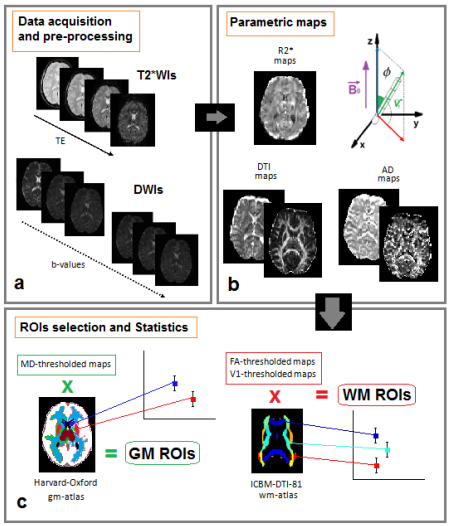

Figure 1 - Flow-chart illustrating the methods. a) Pre-processing of the acquired images, and extraction of parametric maps. b) The orientation of WM fibers Φ with respect to the magnetic field was estimated using

trigonometric relations. c) A composition of thresholds on parametric maps and the use of standard atlases was adopted for WM and GM ROIs selection.

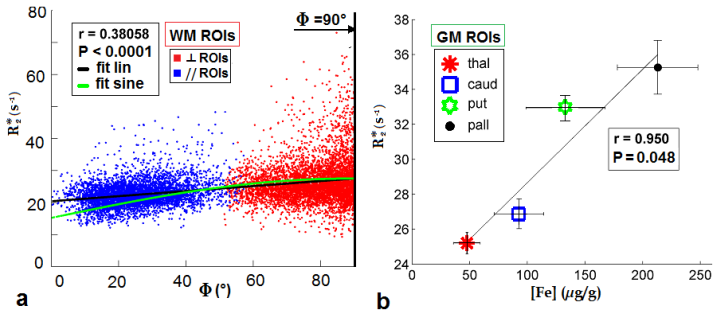

Figure 2 - R2* dependence on magnetic inhomogeneity in WM and GM. a) R2* of WM ROIs with parallel fibers (blue dots) and orthogonal fibers (red dots), plotted against their orientation. The data are linearly fitted (black line), and fitted with a sine function (green curve). b) R2* of thalamus (thal), caudate nuclei (caud), putamen (put) and globus pallidus (pall), estimated from the parametric R2* maps and plotted vs non-heme iron contents. Pearson's correlation coefficient r is reported in the box, together with the level of significance, P.

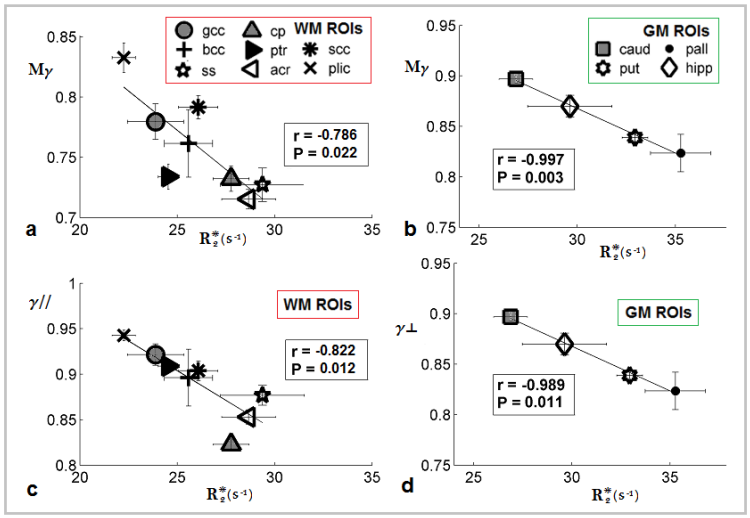

Figure 3 - AD-metrics plotted vs R2*. Mean values of mean-γ (Mγ), axial-γ (γ//) in WM-ROIs (a,c) and of Mγ and radial-γ ($\gamma^{\perp}$), as a function of R2* in GM-ROIs (b,d). Error bars indicate inter-subjects SD; the linear fit, Pearson's correlation coefficient and the significance level are indicated (gcc=genu of corpus callosum, cc; bcc=body of cc; scc=splenium of cc; plic=posterior limb of internal capsule; cp=cerebral peduncle; ptr=posterior thalamic radiations; acr=anterior corona radiata; ss=sagittal stratum; caud=caudate; put=putamen; pall=pallidum; hipp=hippocampus).

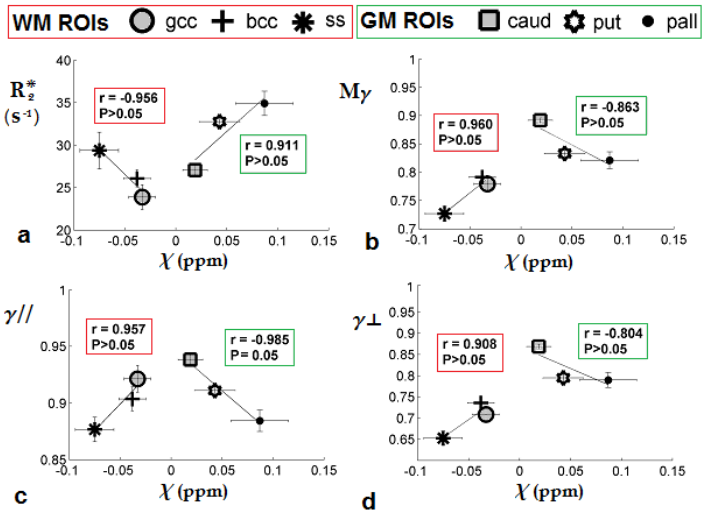

Figure 4 - R2* and AD-derived parameters plotted against χ in WM and GM ROIs. The trends are indicated by linear fits, that are treated separately for WM and GM ROIs. Pearson's correlation coefficients, r, are reported in the boxes, together with the level of significance, P (red boxes for WM ROIs, green boxes for GM ROIs; gcc=genu of corpus callosum, cc; bcc=body of cc; ss=sagittal stratum; caud=caudate; put=putamen; pall=pallidum).

Synopsis

This study aimed at investigating the capability of Anomalous Diffusion(AD)-MRI technique to provide complementary information with respect to the conventional diffusion techniques, regarding the microstructure of brain tissue. Here we confirmed *in vivo* the results previously obtained *in vitro*, suggesting that AD-MRI, differently from DTI, reflects magnetic susceptibility differences due to differences in myelin orientation and iron content within selected regions in brain parenchyma.

The plant vacuole as a biological model system to study the functional properties of intracellular channels and transporters.

A. Carpaneto

Institute of Biophysics (IBF), CNR, Via De Marini 6, 16149-Genova, Italy

e-mail: armando.carpaneto@ge.ibf.cnr.it

Keywords: CLCs, TPCs, TRPML1, endo-lysosome, plant vacuole, patch-clamp

Plant cells have something that animal cells have not: a large intracellular compartment, the vacuole, which has been investigated for long time. The central vacuole can occupy up to 90% of the cell volume and is easy to isolate, differently from intracellular organelles from animal cells as lysosomes or endosomes. Because of its large dimension (up to 40 μm diameter) it can be successfully studied using the classical patch-clamp technique. We had the idea that the vacuolar membrane could be used as a convenient model to characterize the functional properties of animal intracellular transporters and channels [1]. We focused on the three main families of transporters and channels, namely CLCs, TPCs and TRPs, which have members localised in endo-lysosomes. They are emerging to be very important in cellular physiology, as underlined by they involvement in severe diseases. CLC7, a proton/chloride antiporter is involved in osteopetrosis; TPC2, a sodium channel, plays a role in neoangiogenesis processes linked to vascularization of solid tumors, in neurodegenerative Parkinson disease and in Ebola virus infections; TRPML1, a lysosomal cation channel, is responsible of mucolipidosis. We could successfully express all these proteins in Arabidopsis vacuoles lacking the endogenous counterpart and perform a biophysical study [2–4]. We could find interesting unknown modulations, which can help to shed lights on their physiological role in organellar homeostasis and signalling.

[1] M. Festa, L. Lagostena, A. Carpaneto, Using the plant vacuole as a biological system to investigate the functional properties of exogenous channels and transporters, Biochim. Biophys. Acta. (2015). doi:10.1016/j.bbamem.2015.09.022.

[2] A. Costa, P.V.K. Gutla, A. Boccaccio, J. Scholz-Starke, M. Festa, B. Basso, I. Zanardi, M. Pusch, F.L. Schiavo, F. Gambale, A. Carpaneto, The Arabidopsis central vacuole as an expression system for intracellular transporters: functional characterization of the Cl-/H+ exchanger CLC-7, J. Physiol. 590 (2012) 3421–3430. doi:10.1113/jphysiol.2012.230227.

[3] A. Boccaccio, J. Scholz-Starke, S. Hamamoto, N. Larisch, M. Festa, P.V.K. Gutla, A. Costa, P. Dietrich, N. Uozumi, A. Carpaneto, The phosphoinositide PI(3,5)P_2 mediates activation of mammalian but not plant TPC proteins: functional expression of endolysosomal channels in yeast and plant cells, Cell. Mol. Life Sci. 71 (2014) 4275–4283. doi:10.1007/s00018-014-1623-2.

[4] L. Lagostena, M. Festa, M. Pusch, A. Carpaneto, The human two-pore channel 1 is modulated by cytosolic and luminal calcium, Sci. Rep. 7 (2017) 43900. doi:10.1038/srep43900.

Characterization of the interaction between the Amphipathic Cell Penetrating Peptide p28 and the Wild Type and Mutated p53 by Raman and Atomic Force Spectroscopies combined with Surface Plasmon Resonance

Sara Signorelli[a], Simona Santini[a], Tohru Yamada[b], Anna Rita Bizzarri[a*], Craig W. Beattie[b], and Salvatore Cannistraro[a]

[a] Università della Tuscia, Viterbo, 01100, Italy
[b] University of Illinois College of Medicine, Chicago, IL 60612, USA.
E-mail address: bizzarri@unitus.it (A.R. Bizzarri).

Keywords: Raman Spectroscopy, Atomic Force Spectroscopy, Docking, p53, Mutations, Cell penetrating peptide

Tumor suppressor p53 belongs to the class of intrinsically disordered proteins characterized by large unstructured regions. These proteins can adopt an ensemble of diverse, dynamically interchanging, and thermodynamic stable, secondary structure conformations [1]. This highly dynamic nature allows p53 to recognize a wide number of biological targets, without sacrificing specificity, acting as a central hub in a plethora of signaling pathways and playing a key role in the prevention of carcinogenesis [2]. Notably, p53 is often mutated in human cancers, chiefly in the DNA-Binding Domain (DBD), with drastic effects on its functionality; this making p53 an attractive target for anticancer strategies developing drugs addressed to restore its functions. p28, an amphipathic, nontoxic, cell-penetrating peptide, derived from the bacterial copper protein Azurin, can bind the DBD of wild type (WT) as well as of some mutants p53 through hydrophobic interaction inducing an increase of their intracellular levels and functionality, without altering the overall conformation [3][4]. In this context, the investigation of the structural properties of WT [5] and mutants p53 [6] could be useful to explore whether and how DBD punctual mutations can alter p53 conformations and, importantly, if the DBD alterations, in term of conformation and surface hydrophobicity, can correlate with the p28 binding affinity and capability; this aiming to refine the p28 peptide structure and to improve its ability to restore mutant to wild type p53 performance. Accordingly, we have combined Molecular Modeling, Raman spectroscopy coupled with a solvent perturbation strategy, Atomic Force Spectroscopy (AFS) and Surface Plasmon Resonance (SPR) studies to comprehensively characterize site-directed (L114D, A119D, C124D, and C229D) and naturally occurring (K164E, R273H and P223L/V274F) mutant DBDs, also in connection with their interaction with p28. We showed that mutations altering hydrophobicity within non-mutable and mutable regions of the p53-DBD can affect DBD secondary structure potentially reducing p28 binding. The affinity of p28 was positively correlated with the β-sheet content in naturally occurring mutants of DBD, being reduced by an increase of unstructured or random coil regions that resulted from a loss in hydrophobicity and redistribution of surface charge. The combination of the aforementioned techniques allowed us to conclusively demonstrate that p28 does bind to the DBD of p53 and confirm predictions of those binding motifs, providing an alternative approach to define how local alterations in secondary structure affect the binding of p28 to the p53-DBD. These results can help to refine our knowledge of the conformational properties of wild type and mutants p53 and their involvement in p28 binding, therefore getting insight on how potential structural modification in p28 can raise its anticancer activity [6].

[1] M.M. Babu, R. van der Lee, N.S. de Groot, J. Gsponer, Curr. Opin. Struct. Biol. 21 (2011) 432–440.
[2] B. Vogelstein, K.W. Kinzler, Nat Med. 10 (2004) 789-99.
[3] T. Yamada, T.K. Das Gupta, C.W. Beattie, Mol. Pharm. 10 (2013) 3375–3383.
[4] T. Yamada, S. Signorelli, S. Cannistraro, C.W. Beattie, and A.R. Bizzarri, Mol Pharm. 12 (2014)140-149.
[5] S. Signorelli, S. Cannistraro, and A. R. Bizzarri, Appl. Spectrosc. (2017). in press
[6] S. Signorelli, S. Santini, T. Yamada, A.R. Bizzarri, C.W. Beattie, and S. Cannistraro, Biochim et Biophys Acta 1861 (2017) 910–921.

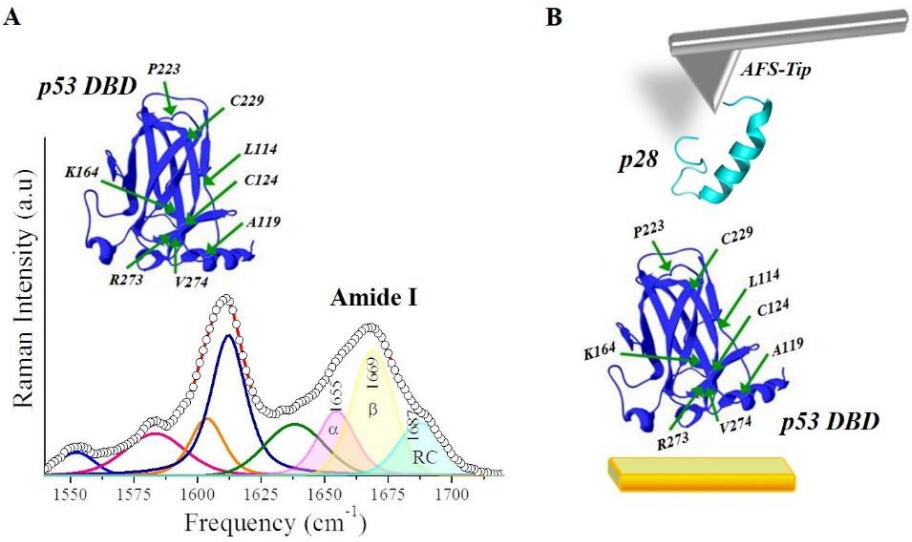

Figure 1. (A) Amide I Raman band (black circles) of wild type DBD fitted using three-component Voigt model (red line) to obtain the structural content of the main conformations present in the protein: α-helix (magenta band), β-sheet (yellow band) and random coil (blue band). The same fitting analysis was applied on both the site-directed and naturally occurring DBD mutants. (B) Schematic sketch of the AFS approach employed to study the interaction of p28 with both the site-directed and naturally occurring DBD mutants.

Ion induced fragmentation of 5BrU pure and hydrated clusters: role of the environment in radiosensitising mechanisms and resulting mutagenesis

M.C. Castrovilli*, P. Markush*, P. Bolognesi*, P. Rousseau†, S. Maclot†, A. Cartoni§,*
R. Delaunay†, A. Domaracka†, J. Kočišek &, B.A. Hubert† and L. Avaldi*

* CNR-ISM, Area della Ricerca di Roma 1, Monterotondo Scalo, Italy
† Normandie Université, CIMAP (UMR6252 CEA/CNRS/ENSICAEN/UNICAEN), Boulevard Henri Becquerel, BP5133, 14070 Caen Cedex 5, France
§ Dipartimento di Chimica, Sapienza Università di Roma, Roma, Italy
& J. Heyrovsk´y Institute of Physical Chemistry, The Czech Academy of Sciences, Prague, Czech Republic
e-mail: matteac@gmail.com

Keywords: 5BrU, pure clusters, hydrated clusters, mutagenesis, cancer, tautomerism, ion impact, hadron therapy.

Exposure of a living organism to ionizing radiation causes alterations that begin at the DNA level [1] and evolve in biological malfunctioning as well as mutation and cellular death. On the other hand, the same pathogenic effects of radiation damage are proficiently used in radiotherapy for cancer treatment. The major drawback in radiotherapy is that it produces an unselective damage in both tumour and healthy cells, with significant side effects for the patients. This issue led to the search for new strategies with targeted drugs, the radiosensitizers [2,3], that enhance the lethal effect of radiation specifically on tumor rather than on normal cells.

Among the different classes of radiosensitisers the halosubstituted pyrimidinic bases and their nucleosides analogues have reached the stage of clinical trials [4]. Among halopyrimidine nucleobases, 5-bromouracil (5BrU) [5,6] is the fundamental building block of bromo-deoxyuridine that, thanks to the similar steric hindrance of the Br atom and the methyl group, can replace thymine into the DNA of fast replicating tumor cells. In the present work we have investigated the $^{12}C^{4+}$ ion induced fragmentation of 5BrU embedded in clusters of molecules of the same species (pure clusters) or with the addition of water molecules (nano-hydrated clusters). Both situations mimic 'realistic' biological media, because of the planar bonding of nucleobases in the cluster, similar to base pairing configuration, as well as the presence of water, the main constituent of human bodies.

These studies indicate that the environment, on one hand, protects the system against the complete break-up in small fragments but on the other, triggers 'new' fragmentation pathways (OH loss). The most striking results are i) the observation in the nano-hydrated clusters, of series of hydrated fragments, which highlights a strong interaction between 5BrU and water molecules with a consequent blocking of specific fragmentation pathways active in the pure cluster (BrC_2H loss) and ii) the evidence that a sufficient number of water molecules can mediate the keto-enol tautomerisation responsible of mutagenesis. This sheds light on the radiosensitising and mutagenic effects of this DNA base analogue.

The present results prove for the first time the 5BrU potential to produce harmful effects on a biological system in terms of both mutagenicity, due to water-mediated tautomerisation, and enhanced fragility, due to ultrafast radiation damage mechanisms. The latter enhances the molecular fragmentation against a statistical redistribution of the absorbed energy, leading to the release of several types of 'hydrated fragments', never observed in other nitrogenous bases.

[1] M.A. Herve du Penhoat, et al., Int. J. Radiat. Biol. ,(2010), 86, 205–219.
[2] A. C. Begg et al., Nat. Rev. Cancer, (2011), 11, 239-253
[3] P. McLaughlin et al. Int. J. Radiat. Oncol., Biol., Phys., (1993), 26, 637.
[4] M. Matsutani et al., Radiat. Med., (1988), 6, 33−39
[5] S. Zamenhof, et al., Nature, (1958), 181, 827.
[6] W. McLaughlin et al., Int. J. Radiat. Oncol. Biol. Phys., (1993), 26, 637.

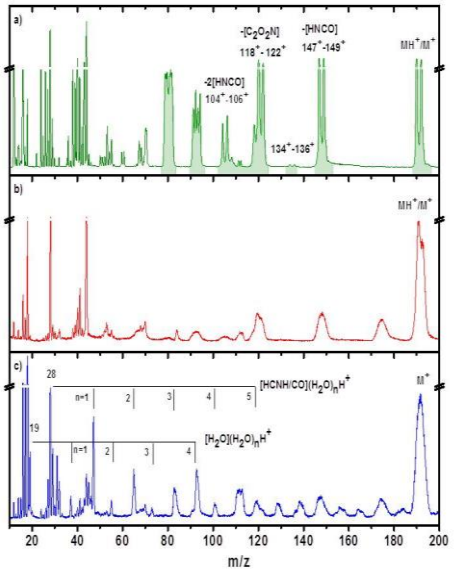

Figure 1. The 36 keV $^{12}C^{4+}$ ion induced mass spectra 5BrU molecules isolated (a) and embedded in pure (b) and nano-hydrated (c) clusters in the m/z region up to the monomer (M^+). Singly charged fragments containing the Br atom display the typical $^{79}Br(^{81}Br)$ isotopic structure and are highlighted as green areas in a). The peaks belonging to the protonated water clusters $(H_2O)_nH^+$ and hydrated $[HCNH/CO](H_2O)_nH^+$ series are indicated in (c).

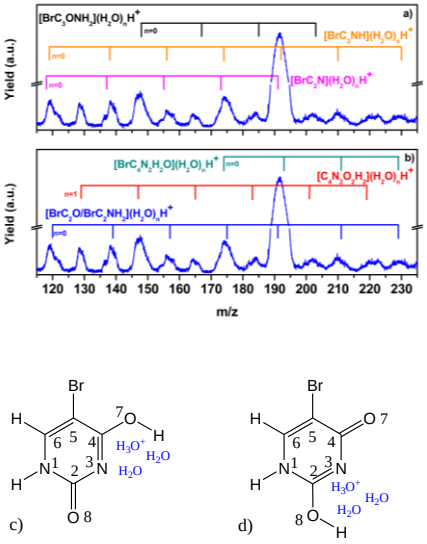

Figure 2. On the top: the 36 keV $^{12}C^{4+}$ ion induced mass spectrum of the nano-hydrated 5BrU clusters in the m/z region 115-235. The peaks belonging to hydrated series are shown. On the bottom: a schematic of the eno-tautomeric forms induced in the nano-hydrated cluster by at least three water molecules.

.

The interaction of H-NS with its target DNA

Bonvin A.[1], Dijk M.[2], Wienk H.[1], Boelens R.[1], Gualerzi C.[3], Spurio R.[3], Miano A.[3], Sette M[4]*.

[1]Bijvoet Center for Biomolecular Research, Faculty of Science-Chemistry, Utrecht University, Padualaan 8, 3584 CH, Utrecht, The Netherlands; [2]AIMMS Division of MolecularToxicology, Department of Chemistry and Pharmaceutical Sciences, VU University, Amsterdam, the Netherlands; [3]Laboratory of Genetics, University of Camerino, via Gentile III da Varano, Camerino 62032 (MC), Italy; [4]Department of Chemical Sciences and Technology, University of Rome "Tor Vergata", via Ricerca Scientifica, 00113, Rome, Italy.

email: sette@uniroma2.it

Keywords: H-NS, DNA repression, NMR, Molecular Biology

H-NS is a DNA-binding protein, known to condensate DNA and to act as a transcriptional repressor on bacterial Gram-negative genes. The protein presents an N-terminal oligomerization and a C-terminal DNA-binding domain linked by a flexible region. The proposed mechanism of repression is thought to occur via binding of the protein at multiple binding sites. Through a combined approach employing molecular biology and spectroscopic techniques, we have shown some of the peculiar features of H-NS binding to its target DNA. The molecular details of this interaction will be illustrated.

Design of allosteric stimulators of the HSP90 ATPase as novel anticancer leads

Ilda D'Annessa [a], Sara Sattin[b], Jiahui Tao[c], Marzia Pennati[d], Carlos Sànchez-Martìn[e], Elisabetta Moroni[f], Andrea Rasola[e], Nadia Zaffaroni[d], David A. Agard[c], Anna Bernardi[b] and Giorgio Colombo*[a]

[a] Istituto di Chimica del Riconoscimento Molecolare, CNR, Milan, Italy
[b] Dipartimento di Chimica, Università degli Studi di Milano, Italy
[c] Howard Hughes Med Inst and Dept. of Biochem & Biophys, Univ of California San Francisco, USA
[d] Dept. Experimental Oncology & Molecular Medicine, Molecular Pharmacology Unit Fondazione IRCCS Istituto Nazionale dei Tumori, Milan, Italy
[e] Dipartimento di Scienze Biomediche – DSB Università di Padova, Italy
[f] IRCCS Multimedica, Milano, Italy

e-mail: giorgio.colombo@icrm.cnr.it

Keywords: Drug Design, Hsp90, Molecular chaperone, Allosteric ligands

Heat Shock Protein 90 (Hsp90) is a ATP-dependent chaperone that controls the folding of more than 200 client proteins and constitutes a central node in many signaling pathways[1]. Overexpression and dysregulation of Hsp90 have been linked with cancer and neurodegeneration. It is thus not surprising that this chaperone has become an important drug-target: in principle its inhibition can result in the simultaneous degradation of multiple clients associated with different pathological hallmarks[2]. A viable way to interfering with Hsp90 is represented by allosteric ligands, which perturb the chaperone by targeting sites alternative to the ATP-site.

In this context, we have developed a method for the identification of allosteric pockets via the analysis of residue-pair distance fluctuations in the structural ensemble around the active state of the chaperone. The protien works as a homodimer and the site we identified is located at the interface between the C-terminus of the two protomers (Figure 1). Based on this, we designed modulators characterized by a *O*-aryl rhamnoside benzofuran scaffold, showing promising anticancer activities and a novel molecular mechanism of perturbation of Hsp90 functions: the ligands in fact were experimentally proved to be *activators* of closure kinetics and ATPase of the chaperone *in vitro*, induce cancer cell death, and interfere with client maturation[2]. We developed a first Quantitative-Structure-Dynamics-Activity-Relationship (QSDAR) model correlating the structures of an initial set of modulators to observed activation effects[3].

Based on this initial model, we report the rational design of new allosteric ligands, reaching low micromolar to nanomolar anticancer activities, which support their potential in the development of anticancer therapeutics (Figure 2). On the computational side, we further develop a model to evaluate the potency of allosteric modulators by taking into account the dynamic cross-talk that exists between the protein and the ligand. We calculated Dynamic Ligand Efficiency (DLE). i.e. the Ligand Efficiency in a multiconformational protein ensemble[3], to correlate predicted docking scores to ATPase stimulation and cellular effects. The model provides a good correlation between DLEs and measured ATPase stimulations (R = -0.66 considering all compounds discussed here and in [3]; R = -0.71 when considering only co-generic amino-derivatives). This finding supports the validity of our model for the design of allosteric activators of Hsp90. Next, we assessed the capacity of our new DLE descriptor to evaluate the potency of the designed compounds in antiproliferative assays. Importantly, the calculated DLE shows a significant correlation with measured cytotoxicities against the cancer STO cell line, with correlation value of 0.62 when considering the whole series, which raises to 0.67 when considering only amines indicating the ability of this very simple model to quantitatively capture the main determinants of cytotoxic activities.

To the best of our knowledge, these results are the first that show the actual feasibility of pushing integrated knowledge of dynamic protein-ligand cross-talk into the design of new Hsp90 allosteric compounds, with novel functional impacts as well as improved antiproliferative activities. We have shown before [2] that these compounds stimulate Hsp90 ATPase activity by accelerating the protein conformational cycle and favoring the catalytically active state: we hypothesize that this reverberates in a modification of the population of the chaperone structural ensembles and of the timing with which Hsp90 conformational families are presented to interaction with co-chaperones and clients. Consistent with recent findings based on mutational studies [3, 4], this novel way of perturbing chaperone populations and kinetics can expectedly be detrimental to cell viability.

[1] K. A. Krukenberg, T. O. Street, L. A. Lavery and D. A. Agard, *Q. Rev. Biophys.* **2011**, *44*, 229-255.
[2] S. Sattin, J. H. Tao, G. Vettoretti, E. Moroni, M. Pennati, A. Lopergolo, L. Morelli, A. Bugatti, A. Zuehlke, M. Moses, T. Prince, T. Kijima, K. Beebe, M. Rusnati, L. Neckers, N. Zaffaroni, D. A. Agard, A. Bernardi and G. Colombo, *Chem. Eur.J.* **2015**, *21*, 13598-13608.
[3] G. Vettoretti, E. Moroni, S. Sattin, J. Tao, D. Agard, A. Bernardi and G. Colombo, *Sci. Rep.* **2016**, *6*, 23830.
[4] B. K. Zierer, M. Rubbelke, F. Tippel, T. Madl, F. H. Schopf, D. A. Rutz, K. Richter, M. Sattler and J. Buchner, *Nat Struct Mol Biol* **2016**, *23*, 1020-1028; b) A. Rehn, E. Moroni, B. K. Zierer, F. Tippel, G. Morra, C. John, K. Richter, G. Colombo and J. Buchner, *J. Mol. Biol.* **2016**, *428*, 4559-4571.M.F. Krummel MF, Nat Immunol. 11(2010) 554-7.

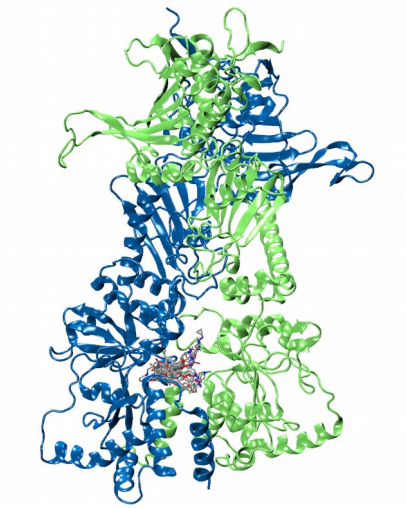

Figure 1.Overall view and detailed superposition of the best pose for each compound in the allosteric site. Color code: Protomers A and B, light blue and green respectively; compounds: C=grey, O=red, N=blue, Cl=green, F=dark yellow.

Table 1. Structures, stimulatory potencies, and cytotoxic activities of designed compounds.[a]

Compound	Normalized ATPase rate	Toxicity in STO (IC_{50} [μM])
1	1.1[b]	57.0±2.1[b]
18	4.8[b]	8.9±1.1[b]
19	6[b]	9.9±1.1[b]
20	1.5	16±1
21	2.2	8.2±2.7
22	1.9	11.7±2.4
23	2.4	3.9±1.8
24	4.1	8.6±2.1
25	4.5	22.1±1.1
26	4.2	4.1±0.4
27	1.4	not soluble
28	1.3	36±6
29	1.17	>75
30	0.98	>100
31	–	0.57±0.04

Figure 2. Structures, stimulatory potencies and cytotoxic activities of designed compounds.

Tuning the molecular mechanism of Hsp70 via a new allosteric network

S. Rinaldi [a], V. Assimon [b], Z. Young [c], G. Morra [a], J. Gestwicki [b], G. Colombo [a]

[a] Istituto di Chimica del Riconoscimento Molecolare, CNR Via Mario Bianco, 9 20131 Milano, Italy

[b] Department of Pharmaceutical Chemistry, University of California at San Francisco, CA 94158

[c] Department of Medicinal Chemistry, Biology, University of Michigan, Ann Arbor, MI 48109

Email: silvia.rinaldi24@gmail.com

Keywords: Molecular Dynamics, Allosteric regulation, Molecular chaperons, Modulation of functional motions.

The study of the correlations among protein structure, dynamics and function can be efficiently addressed by means of novel Molecular Dynamics (MD) based methods. In this scenario, the study of the impact of ligand-dependent conformational perturbations on functionally relevant protein motions provides new opportunities to regulate their biological activity. Herein, we address this question by advancing the mechanistic understanding on heat shock protein 70 (Hsp70) regulation at the atomic level and identifying molecules capable of selectively interfering with key structural and functional sub-states. Hsp70 system is a model for the next generation of difficult drug targets: it is composed of multiple protein components that show nucleotide-dependent allosteric regulation, it intersects many different biochemical and cellular activities and its dysregulation is implicated in several diseases, including neurodegenerative disorders and several types of cancer lines.[1,2,3] In this framework, the rational understanding of the best ways turning this system “on” or “off” with small molecules is particularly challenging, but highly promising. This idea has already proved its efficacy: the anticancer compound MKT-077 and its analogs have been shown to derive their activity by differentially interacting with Hsp70 allosteric states and impact multiple disease phenotypes.[4] Based on these findings, we combined the computational analysis of the main traits of internal dynamics differentially induced by MKT-077 on various Hsp70 nucleotide sub-states with *in vitro* mutagenesis experiments to identify the substructures that are most relevant in modulating the functional motions of the Hsp70. With this approach, we show that it is possible to rationally identify mutations that mimic the impact of MKT-077 on Hsp70 functions: in particular, we show that both the allosteric ligand and the mutations trap the chaperone in an ADP-like conformation where it can no longer carry out its physiological activity. The combination of our structural and biochemical studies provides new insights into possible ways to tune Hsp70’s functions to treat disease. While motivated by the challenges of Hsp70 as a drug target, the approach used is general and can be broadly extended to other difficult protein targets.

[1] Mayer, M. P., and B. Bukau. "Hsp70 chaperones: cellular functions and molecular mechanism." Cellular and molecular life sciences 62.6 (2005): 670-684.
[2] Swain, Joanna F., et al. "Hsp70 chaperone ligands control domain association via an allosteric mechanism mediated by the interdomain linker." Molecular cell 26.1 (2007): 27-39
[3] Murphy, Maureen E. "The HSP70 family and cancer." Carcinogenesis 34.6 (2013): 1181-1188
[4] Rousaki, Aikaterini, et al. "Allosteric drugs: the interaction of antitumor compound MKT-077 with human Hsp70 chaperones." Journal of molecular biology 411.3 (2011): 614-632

YAP regulates cell mechanics by controlling cell-matrix interaction strength

Jorge Oliver De La Cruz[a], Giorgia Nardone[a], ,Jan Vrbsky [a], Ana Rubina Perestrelo [a], Vladimir Vinarsky [a], Fabiana Martino[a] Stefania Pagliari[a], Giancarlo Forte [a,b].

[a]Center for Translational Medicine (CTM), International Clinical Research Center (ICRC), St Anne's University Hospital, Pekarska 53, Brno, CZ-65691, Czech Republic
[a] Department of Biomaterials Science, Institute of Dentistry, University of Turku, Turku FI-20014, Finland.

e-mail: giancarlo.forte@fnusa.cz

Keywords: (mechanobiology, Hippo pathway, cell-matrix interaction, focal adhesions)

The extracellular matrix (ECM) is the non-cellular constituent of the tissues that, far from being an inert structural scaffold, provides biochemical and biomechanical cues that impact on cell behavior. Several reports have focused on the molecular systems by which the ECM interaction impacts on the Hippo signaling pathway to regulate YAP nuclear shuttling and its consequent co-transcriptional activity[1,2].

In the present work, we describe the mechanism by which the mechanotransducer YAP directly controls through its transcriptional activity both the deposition of extracellular matrix components and the assembly of the intracellular apparatus of cell-ECM interaction, the focal adhesions (FAs). In fact, by exploiting ChIP-seq technology and YAP mutants obtained by CRISPR/Cas9 targeted approach, we unveil a number of targets of YAP-DNA binding activity that lead to the formation of membrane complexes devoted to the interaction with ECM including various integrin subunits like ITGA1, ITGA4, ITGAV and ITGB1, talin2, cadherins and catenins. At the same time, YAP binds DNA elements connected to the activation of genes encoding for ECM structural proteins like versican, collagens, laminins, fibronectin and osteonectin or involved in the processing of ECM components, like hyaluronan synthase 3, connective tissue growth factor (CTGF) and metallopeptidases. As expected, YAP mutant clones underwent a substantial switch in the expression of genes involved in structural ECM composition and remodeling, thus leading to the complete absence of FAs. As a consequence, cells failed to spread, invade and migrate through the surrounding matrix, when challenged in 2D and 3D assays and lose the ability to spread and acquire the given shape, develop tension through the cytoskeleton and exert force against the surrounding ECM.

Consistent with the model of YAP acting as a master of cell-ECM interaction, cell biophysical parameters were partially recovered by the re-expression of transcriptionally active YAP or ITGAV integrin subunit in conjunction with ITGB3 subunit, two of the proteins being more affected in YAP-defective cells[3].

In conclusion, YAP functions as the principal regulator of cell-matrix interface, being able to control the expression of crucial genes involved in the composition and arrangement of the extracellular environment, together with key components of cell mechanosome.

References:

[1] D. Mosqueira, S. Pagliari, K. Uto et al. (2014), ACS Nano. 8(3):2033-47

[2] NG. Kim and BM. Gumbiner (2015), J Cell Biol. 210(3): 503–515

[3] G. Nardone, J. Oliver De La Cruz et al. (2017), Nat Comm. DOI: 10.1038/ncomms15321

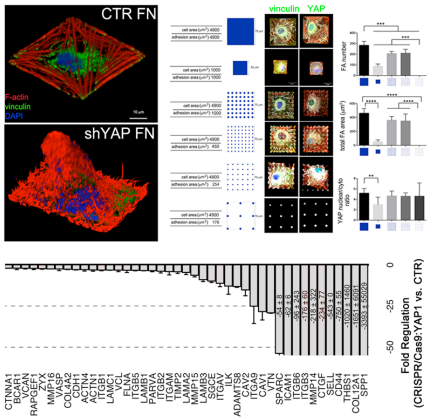

Figure 1. YAP depletion causes cell-ECM disruption. YAP activity is controlled by cell area independently of FA formation. YAP depletion results in decreased ECM and FA gene expression.

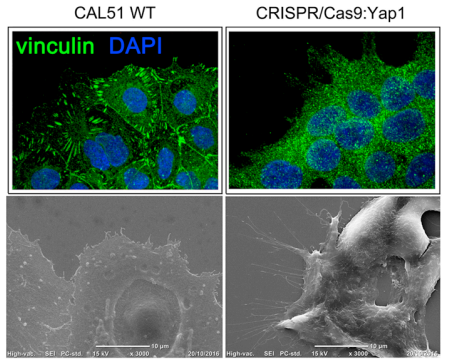

Figure 2. YAP-depleted cells lose the grip on ECM and fail to spread

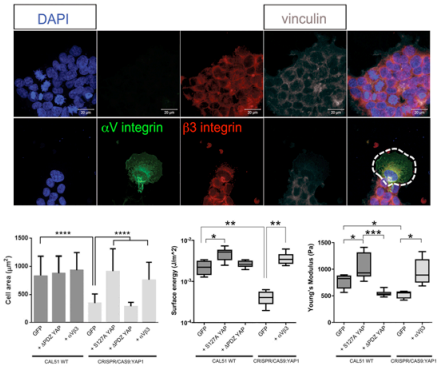

Figure 3. Re-expression of components of the Integrin-FA system partially restores the spreading and biomechanics of YAP-depleted cells.

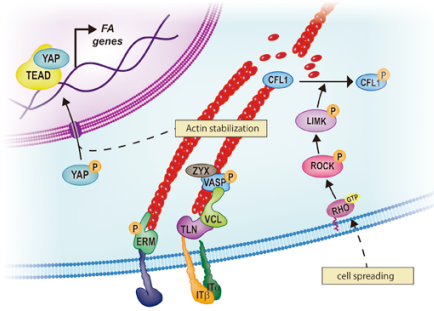

Figure 4. Cell spreading triggers RhoA/ROCK activation and YAP shuttling to the nucleus where it directly activates FA and ECM genes.

Ultrastructural study of biomineralization process in human bone marrow mesenchymal stem cells during the osteoblastic differentiation

E. Malucelli[a], A. Procopio[a], A. Pacureanu[b], A. Sargenti[a], S. Castiglioni[c], C. Cappadone[a], G. Farruggia[a], J. Maier[c], P. Cloetens[b], S. Iotti[a]

[a] Dip.to di Farmacia e Biotecnologie, Università di Bologna, Bologna
[b] European Synchrotron Radiation Facility, 38043 Grenoble Cedex 9, France
[c] Dipartimento di Scienze Biomediche e Cliniche "L. Sacco", Università di Milano, Milano
e-mail: emil.malucelli@unibo.it

Keywords: (Mesenchymal stem cell, synchrotron-based x-ray techniques, Osteoblastic differentiation)

Biomineralization (BM) is the process by which organisms form organized mineral crystals during tissue regeneration. During the BM process ions in solution are converted to biominerals thanks to chemical-physical transformations performed by the cellular activity. The process creates complex composite materials, made of organic and inorganic compounds. On the nanometric scale the highly specialized organic matrix of collagen microfibrils seems to direct the formation of nanosized platelet-hydroxyapatite (HA) oriented parallel to the collagen fibril axis [1-2]. Alongside these organic components, a mineral precursor amorphous, calcium phosphate is believed to play a fundamental role in the growth of HA nanocrystals. At the cellular level, the formation, maintenance, and repair of bone is based on the complex crosstalk between osteoclasts, osteoblasts and osteocytes[3]. Osteoblasts differentiate from bone mesenchymal stem cells (bMSC) and promote bone deposition [4].
Calcium is a crucial mineral for the bone and is present in the extracellular mineralized matrix as an integral component of hydroxyapatite crystals. Very little is known about the intracellular Ca concentration, distribution and homeostasis in bMSC, and even less about the progression of the extracellular Ca-phosphates and polyphosphates deposition during osteoblast differentiation. Several ionic substitutions in the HA structure are important also in BM; among these Zinc has drawn considerable attention due to its inhibitory activity to osteoclastic bone resorption [5].
Thanks to the advent of synchrotron radiation sources, which provide high intense coherent X-ray beams, it is now possible to study at nanoscale the cellular content and the extracellular deposition of the elements involved in the HA formation.
The goal of this study is to measure the intracellular Ca concentration and the extracellular Ca, P and Zn deposition in bMSC induced to osteoblast differentiation. Human bMSC have been isolated from the bone marrow of healthy individuals. bMSC have been exposed to a differentiating cocktail containing β-Glycero-phosphate, 50 µg/ml ascorbic acid, and vitamin D. Samples have been taken at day 0 (as control) and at 4, 10 days of differentiation towards osteoblast. Cryogenic sample preservation was used, and frozen hydrated cells have been studied at the beamline ID16A-NI at the ESRF synchrotron. In particular, we combined X-ray Fluorescence Microscopy (XRFM) measurements with x-ray phase contrast nano-tomography, to obtain 2D Ca, P and Zn concentration maps at high spatial resolution (down to 15nm). Moreover, to overcome the misleading interpretation coming from 2D elemental maps, we acquired x-ray fluorescence tomography to better localize in the space the deposition of Ca, P and Zn.
The preliminary results (Figure 1) of the 2D fluorescence shown an early spot deposition of Ca already at 4 days. It is worthy to note that in correspondence of Ca deposition a P and Zn accumulation is present as well, Moreover, the extracellular deposition of Ca at 10 days is massive since the bMSC osteoblast differentiation is almost complete and the co-localization of Ca with P and Zn is still evident.
These results strongly suggest the presence of some phosphate or polyphosphate compound of Ca precursors of the HA formation. Further analysis for the visualization of the 3D results are still ongoing.

REFERENCES:
[1] Nudelman F. et al., Nat Mater 9, 1004 (2010).
[2] Scaglione S. et al., Scientific Reports 2, 1-6 (2012).
[3] Kular J. et al., ClinicalBiochemistry, 45, 12 (2012).
[4] Abdallah BM. et al., Gene Therapy, 15 (2008)
[5] Bhattacharjee P. et al., Journal of Asian Ceramic Societies 2, 44-51 (2014).

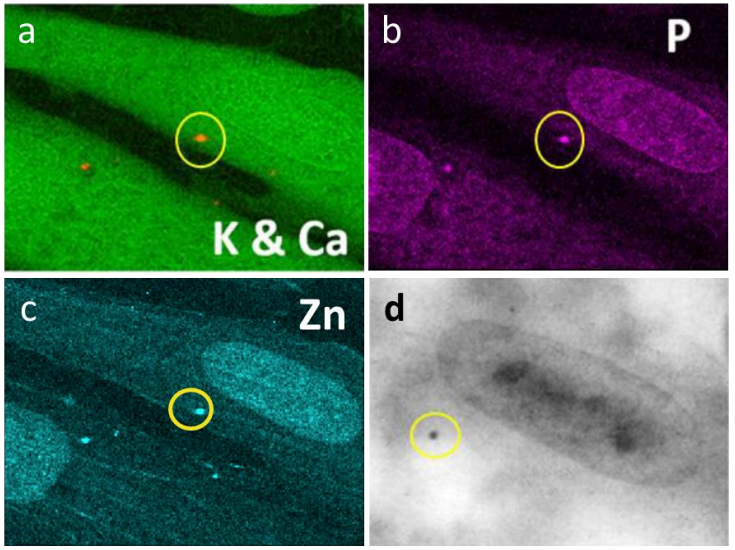

Figure 1. shows the deposition of Ca, P and Zn after 4 days of differentiation in bMSC (Panel a, b and c). Panel d, particular of phase contrast reconstruction of the same bMSC

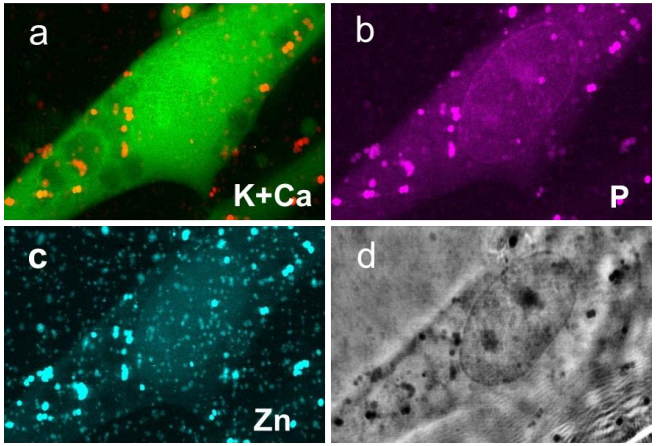

Figure 2. shows the deposition of Ca, P and Zn after 10 days of differentiation in bMSC (Panel a, b and c). Panel d, phase contrast reconstruction of the same bMSC

Engineering functional skeletal muscle networks by microfluidic bioprinting

Marco Costantini [a], Stefano Testa [b], Pamela Mozetic [a], Marcella Trombetta [a], Stefano Cannata [b], Cesare Gargioli [b] and Alberto Rainer [a]

[a] Tissue Engineering Lab, Università Campus Bio-Medico di Roma, 00128, Italy
[b] Department of Biology, University of Rome Tor Vergata, 00173, Italy

e-mail: a.rainer@unicampus.it

Keywords: 3D bioprinting, microfluidics, artificial muscle, myotubes

In mammalians, myogenesis is a complex phenomenon starting from the very first weeks of embryonic development. This process involves mononucleated cells named myoblasts that progressively fuse forming plurinucleated syncytia named myotubes. As development proceeds, myotubes undergo a maturation process, they grow in size, and eventually the actin-myosin based contractile apparatus is assembled, together with the neuromuscular and myotendinous junctions. Skeletal muscles can self-repair relatively small damages resulting from tears, small lacerations, strains, or toxins via a three-stage process that involves demolition, repair, and remodeling of myotubes. However, skeletal muscle cannot restore significant tissue loss that can arise after severe trauma, invasive surgeries, or degenerative diseases.

3D bioprinting has the potential to fabricate highly customizable and highly organized structures that, in principle, could be used for the assembly of an entire muscle [1]. This emerging biofabrication technology relies on the simultaneous deposition of cells and biomaterials in a layer-by-layer fashion, to form 3D well-organized heterogeneous structures that can mirror relevant complex biological architectures both physiologically and morphologically. Thanks to these attractive features, 3D bioprinting is rapidly becoming a first-choice technique for a broad set of tissue engineering (TE) scenarios, including skeletal muscle tissue reconstruction [2]. Inspired by the native structural morphology of skeletal muscles, we speculated that the spatial confinement of muscle precursor cells (C2C12) into highly aligned and compact 3D bioprinted hydrogel fiber structures could lead to a better orientation of the arising myotubes, thus mimicking the natural muscle morphology and organization more closely [3,4]. Building on such a premise, we developed a 3D bioprinting strategy based on a custom microfluidic printing head coupled to a co-axial extruder (Figure 1). This system enables the high resolution deposition of multi-material and multi-cellular structures by simultaneously extruding different bioinks or by rapidly switching from one bioink to another. Within few days of in vitro culture following 3D bioprinting, C2C12 started to elongate and fuse, forming highly aligned myotubes. The obtained myo-structures were thoroughly analyzed in terms of myotube length and orientation, fluorescence immunocytochemistry, and gene expression of relevant myogenic differentiation markers (MHC, MYOD, MYOG), revealing a significant differentiation and maturation of myotubes (Figure 2). Moreover, we demonstrated in vivo that the 3D bioprinted constructs outperformed control bulk-hydrogels in terms of myotube structural organization, supporting the hypothesis that the simple geometrical confinement exerted by 3D bioprinted hydrogel fibers promotes the architectural organization of muscle precursors cells.

These studies have the potential to unveil the mechanisms by which muscle precursors sense substrate stiffness and confinement, therefore representing a key starting point for the development of novel skeletal muscle regeneration strategies.

[1] Melchels FPW, Domingos MN, Klein TJ, Malda J, Bartolo PJ, Hutmacher DW, Additive manufacturing of tissues and organs, Prog. Polym. Sci. 37 (2012) 1079-1104,
[2] Murphy S V and Atala A, 3D bioprinting of tissues and organs Nat. Biotechnol. (2014) 32 773–85
[3] Costantini M, Testa S, Mozetic P, Barbetta A, Fuoco C, Fornetti E, Tamiro F, Bernardini S, Jaroszewicz J, Święszkowski W, Trombetta M, Castagnoli L, Seliktar D, Garstecki P, Cesareni G, Cannata S, Rainer A and Gargioli C, Microfluidic-enhanced 3D bioprinting of aligned myoblast-laden hydrogels leads to functionally organized myofibers in vitro and in vivo Biomaterials (2017) 131 98–110.
[4] Costantini M, Testa S, Fornetti E, Barbetta A, Trombetta M, Cannata SM, Gargioli C and Rainer A, Engineering Muscle Networks in 3D Gelatin Methacryloyl Hydrogels: Influence of Mechanical Stiffness and Geometrical Confinement, Front. Bioeng. Biotechnol. (2017) 5:22.

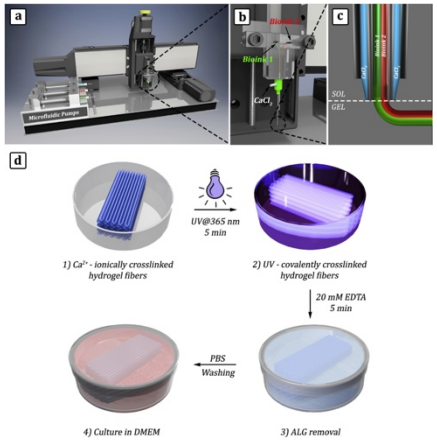

Figure 1. (Top) 3D bioprinting set-up composed of syringe pumps and a microfluidic printing head coupled to a coaxial extruder. (Bottom) Scheme of the cross-linking procedure.

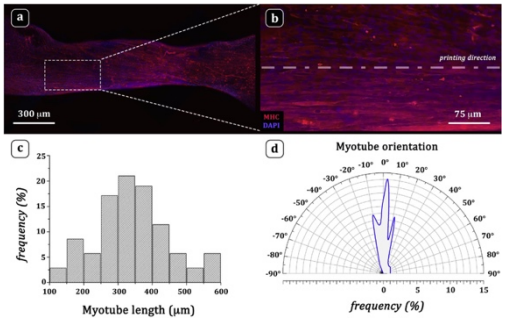

Figure 2. Quantification of myotube alignment and length for 3D bioprinted constructs after 15 days in vitro.

Simple 3D direct laser writing for tissue engineering

Mochi F. [a], De Matteis F. [a], Prosposito P. [a], Francini R. [a], Casalboni M. [a]

[a] Dept. Industrial Engineering and INSTM, University of Rome Tor Vergata, Via del Politecnico 1 Rome, 00133, Italy
and
Center for Regenerative Medicine, University of Rome Tor Vergata, Via Montpellier 1, Rome, 00133, Italy.
e-mail: federico.mochi@gmail.com

Keywords: (Scaffold, 3D printing, Tissue Engineering, PEGDa)

One of the main goals in tissue engineering research is to reproduce in vitro structures, mimicking the extracellular matrix (ECM), able to favorite the stem cell differentiation and the tissue growth. A 3D porous structure suitable to the scope is called scaffold.[1,2] In this contribution, we propose a simple process for scaffold fabrication based on photolithography using one photon polymerization. We used polyethyleneglycol-diacrylate (PEGDa) as photopolymerizable material for the scaffold. The PEGDa solution was prepared using PEGDa (MW 575) at 75% in ethanol. Irgacure 819 was dissolved in the alcoholic part of the solution to promote the polymerization process at a 7 mM concentration.

The main concerns in 3D photolithographic applications is to restrict the polymerization to a well-defined volume in order to achieve the desired resolution. The vertical resolution is often achieved exploiting two photon absorption (2PA) due to the dependency from the square of the light beam intensity. That requires the use of ultrafast-pulsed lasers which are able to concentrate enough energy in a well confined spatio-temporal volume. We present a simple alternative to such 2PA set-up that allows to directly write a photopolymerized pattern using a blue diode laser.

Figure 1 shows the optical setup. We used a diode laser (60 mW) at 448nm wavelength coupled with a multimode optical fiber (600µm core diameter) (OF). The outlet of the OF was set above a microscope objective. The distance between the OF and the objective was 22 cm. The objective was mounted on an x–y movement in order to control the position of the focusing point. The optical power focused on the sample was 60 µW.

The excitation wavelength falls on the tail of the absorption of the photopolymerizable PEGDA solution. As a consequence, the efficiency of the photopolymerization activation is strongly reduced. The efficiency of photopolymerization, as measured by the width of the polymerized linear structures, is represented as a function of the Irgacure concentration in Figure 2. A threshold value for the Irgacure concentration is set at the value of 6 mM below which no polymerization is produced. Figure 3 shows the intensity profile of the excitation light as a function of the depth in the solution for three different focusing optics. The intensity of the light reduces by a factor 5 within a penetration depth equal to the depth of focus (DOF) of the optical system. That sets the limit for the active volume to the minimal waist of the focused beam. The threshold for polymerization is not reached outside that volume where the intensity is not enough to trigger the process.

Figure 4 shows an optical image of a 3D scaffold (alternate woodpile structure) realized with this technique. We achieved a resolution of about 5-7µm for samples of about 1x1x1 mm^3. Evidence of cell differentiation using human Lin- Sca-1+ cardiac progenitor cells has been shown in absence of any concurring biochemical stimulus using woodpile scaffolds fabricated by this technique.[3]

[1] F. Mochi, et al (2016) IET Conference Proceedings, 84 (4.)
[2] P. Prosposito et al. (2017) Materials Science Forum, 879:1519-1523
[3] M.Ciocci et al, (2017) Stem Cell Dev. submitted.

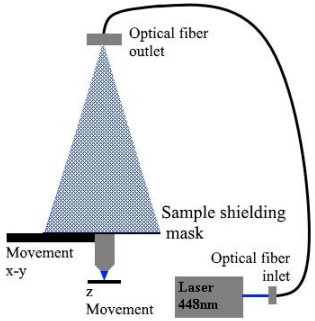

Figure 1. Scheme of the optical setup.

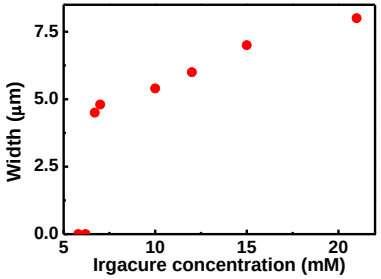

Figure 2. Width of the polymerized linear structures as a function of Irgacure 819 concentration

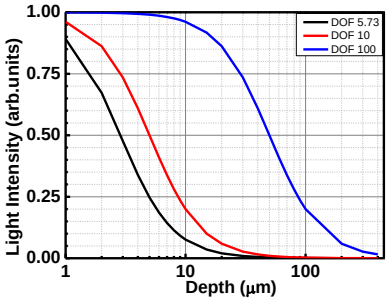

Figure 3. Intensity profile of the excitation light as a function of the depth in the solution for three different focusing optics.

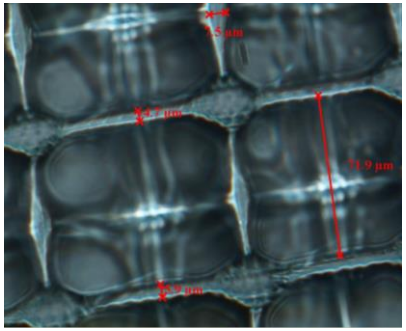

Figure 4. 50x optical micrograph of 1PP-PEGda (MW 575) woodpile structure.

Molecular details of the first steps in photosynthesis

Leonardo Guidoni[a b]

[a] Università degli Studi de L'Aquila, Dipartimento di Scienze Fisiche e Chimiche, Italy.
[b] Sapienza – Università di Roma, Dipartimento di Fisica, Italy
e-mail: leonardo.guidoni@univaq.it

Keywords: photosystem II, water splitting, molecular dynamics, electronic structure calculations, Quantum Mechanics / Molecular Mechanics

Although photosynthesis in plants and bacteria is sustaining all the life on earth since about two and a half billions of years, the details of its mechanisms of working are still elusive. The overall mechanism of energy conversion in photosynthesis include the capture of light by antenna systems, the primary charge separation that convert the photon energy into chemical energy, and the subsequent cascade of biochemical processes leading to the formation of stable high-energy organic products that can be stored in the living organisms (ATP and sugar). One fundamental step of such mechanisms is the conversion of the electronic excitations into chemical energy used to perform the light-driven transformation of water molecules into molecular oxygen and hydrogen equivalents, i.e. water splitting. This water oxidation in photosynthetic organisms occurs through a series of intermediate steps S0-S4 of the so-called Kok-Joliot's cyle in the Oxygen Evolving Center of Photosystem II (PSII). The four electrons necessary for the water splitting reaction are subsequently removed by a radical tyrosine (Tyr_Z) from the Mn_4CaO_5 core, where they are accumulated to perform the more difficult catalytic step: the formation of molecular oxygen. The Photosystem II protein complex has been in the last 5 years the target of several cutting-edge experiments of X-ray crystallography also using the Free Electron Laser. [1-3] The molecular details of the single steps occurring in water oxidation catalysis are starting to be revealed also thanks to the supporting use of electronic structure calculations.
Beyond their interests in biophysics, the comprehension of photosynthetic water splitting mechanisms is also important to inspire artificial catalysts and possible biomimetic catalysts for water oxidation [4-6].
Using QM/MM dynamics and gas phase models we have built a comprehensive pathways of intermediate steps which involves interconversions between open and closed cubane isomers and the binding of a water molecule to Mn4, upon its oxidation. [7-9] Along this pathway, we have also calculated vibrational properties through dipole-dipole autocorrelation function and vibrational density of states from QM/MM dynamics. Our results allowed us to assign specific vibrational bands to molecular motions in different regions of the catalytic pocket and in different parts of the vibrational spectra. [10] In particular to help the interpretation of the computational and experimental data in the low frequency region (400-700 cm-1), we propose a decomposition of the Mn4CaO5 moiety into five separate parts, composed by "diamond" motifs, each one involving four atoms. The spectral signatures arising by this analysis can be easier interpreted to assign experimentally known bands to specific molecular motions. A similar analysis is also extended to all the Mn-ligands in the S1, S2 and S3 state. Starting from the S3 state we have also investigated several possible pathways and spin surfaces that may lead to the formation of the O-O bond.

[1] Y. Umena, K. Kawakami, J.-R. Shen, N. Kamiya, *Nature* 473, 55 – 60 (2011).
[2] Suga, M. et al. *Nature* 1–17 (2014).
[3] Suga, M. et al. *Nature* 543, 131–135 (2017).
[4] D. Nocera, *Acc.Chem.Res.* 45, 767- 776 (2012).
[5] G. Mattioli, P. Giannozzi, A. Amore Bonapasta, L. Guidoni, *JACS* 35, 15353–15363 (2013).
[6] Zhang, C. et al.. *Science* 348, 690–693 (2015).
[4] D. Bovi, D. Narzi, L. Guidoni, *Angewandte Chemie* 52, 11744–11749 (2013).
[5] D. Bovi, D. Narzi, L. Guidoni, *New Journal of Physics*, 16, 015020 (2014).
[6] D. Narzi, D. Bovi, L. Guidoni, *Proc.Nat.Acad.Sci.,* 111*, 8723–8728* (2014).
[7] D. Bovi, M. Capone, D. Narzi, L Guidoni, *BBA Biomembranes* 1857, *1669-1677* (2016).

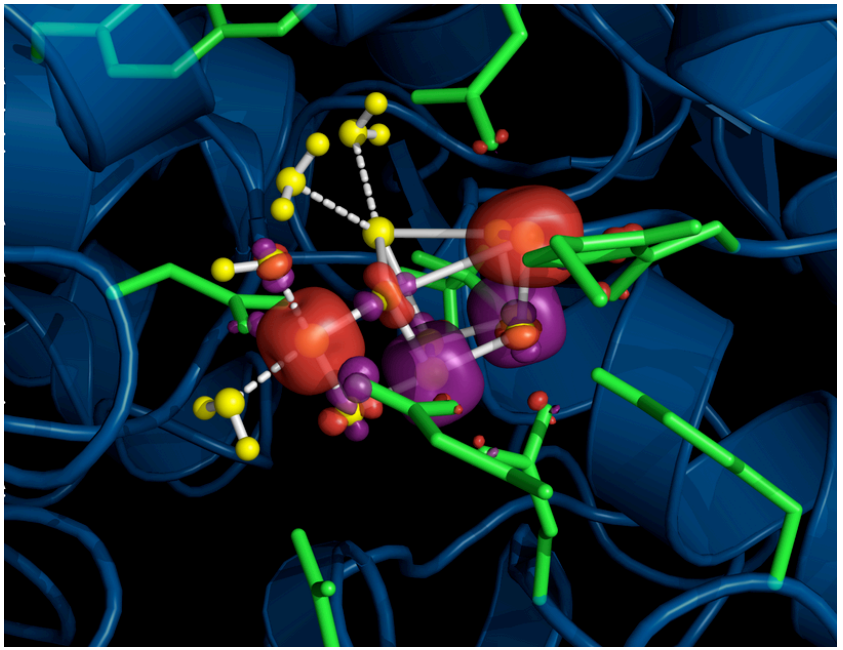

Figure
Quantum Mechanics / Molecular Dynamics simulation of catalytic site of the Photosystem II complex. The up and down spin density is highlighted in red and violet.

A Comprehensive Description of the Homo and Heterodimerization Mechanism of the Chemokine Receptors CCR5 and CXCR4

Daniele Di Marino,[a] Vittorio Limongelli,[a]

[a] *Department of Informatics, Institute of Computational Science, Università della Svizzera Italiana (USI)*

Signal transduction across cellular membranes is controlled by G protein-coupled receptors (GPCRs). In this family of transmembrane proteins the binding of extracellular physiological ligands stabilize the active conformation of receptors, leading to cellular response. It is widely accepted that members of the largest GPCR family self-assemble as dimers or higher-order but the functional consequences of the dimerization was described only for few receptors. The chemokines receptors are GPCRs manly implicated in the functioning and maintenance of the immune system. These receptors represent prime targets for therapeutic intervention in a wide spectrum of inflammatory and autoimmune diseases, heart diseases, and HIV. The CXCR4 and CCR5 receptors are two of the manly studied playing crucial roles in different pathologies. It was recently shown that inhibition of the CCR5-CXCR4 heterodimer formation reduces atherosclerosis in a hyperlipidemic mouse model. Furthermore the entry of HIV type 1 virus into host cells requires CXCR4 and CCR5. In this scenario the use of computational techniques able to describe complex biological processes such as protein dimerization acquires a great importance. Combining coarsegrained (CG) molecular dynamics and well-tempered metadynamics (MetaD) we are able to describe the mechanism of dimer formation, capturing multiple association and dissociation events allowing to compute a detailed free energy landscape of the process. CG-MetaD is an enhanced sampling method particularly suitable to describe processes with very slow rates of interconversion among the possible states of the system. This approach provides an accurate and comprehensive description of the dimerization free energy landscape, thereby revealing critical motions and important structural-dynamical features involved in the homo- and heterodimer formation of the CCR5 and CXCR4 receptors.

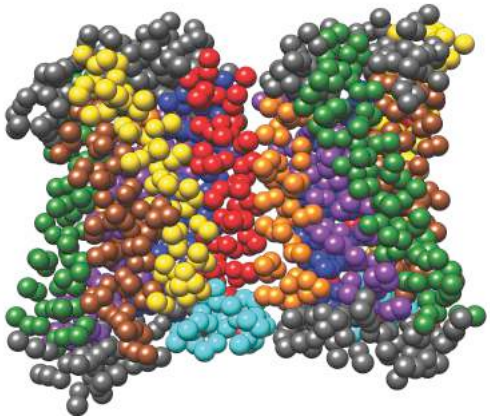

Figure 1: representative snapshot of the coarse-grained simulation

References

1. Structure-function of the G protein-coupled receptor superfamily.Katritch V, Cherezov V, Stevens RC. Annu Rev Pharmacol Toxicol. 2013;53:531-56.
2. Chemokine receptor oligomerization and allostery. Stephens B, Handel TM. Prog Mol Biol Transl Sci. 2013;115:375-420.
3. Structure-function of the G protein-coupled receptor superfamily.Katritch V, Cherezov V, Stevens RC. Annu Rev Pharmacol Toxicol. 2013;53:531-56.
4. G Protein-Coupled Receptor Multimers: A Question Still Open Despite the Use of Novel Approaches. Vischer HF, Castro M, Pin JP. Mol Pharmacol. 2015 Sep;88(3):561-71.
5. Chemokine and chemokine receptor structure and interactions: implications for therapeutic strategies. Kufareva I, Salanga CL, Handel TM. Immunol Cell Biol. 2015 Apr;93(4):372-83.
6. The MARTINI force field: coarse grained model for biomolecular simulations. Marrink SJ, Risselada HJ, Yefimov S, Tieleman DP, de Vries AH. J Phys Chem B. 2007 Jul 12;111(27):7812-24.

7. Escaping free-energy minima. Laio A, Parrinello M. Proc Natl Acad Sci U S A. 2002 Oct 1;99(20):12562-6. Well-tempered metadynamics: a smoothly converging and tunable free-energy method. Barducci A, Bussi G,
8. Parrinello M. Phys Rev Lett. 2008 Jan 18;100(2):020603. PLUMED 2: New feathers for an old bird. Tribello GA, Bonomi M, Branduardi D, Camilloni C, Bussi G. Comput Phys Commun. 2014;185:604–13.
9. GROMACS 4.5: a high-throughput and highly parallel open source molecular simulation toolkit. Pronk S, Páll S, Schulz R, Larsson P, et al.Bioinformatics. 2013 Apr 1;29(7):845-54.

Differential modulation of αvβ3 dynamics upon RGD-ligands

Antonella Paladino[a], Monica Civera[b], Laura Belvisi[b], Giorgio Colombo[a].
[a] Institute of Chemistry of Molecular Recognition – CNR, via Mario Bianco 9, 20131 Milano
[b] Department of Organic and Industrial Chemistry, University of Milan
e-mail: antonella.paladino@icrm.cnr.it

Keywords: (integrins, molecular simulations, ligand binding, peptidomimetics, allostery)

Integrins are heterodimeric cell adhesion receptors composed of two non covalently bound α and β glycoproteins. On the cell surface these proteins exist in an inactive state. The tripeptide RGD has been identified as the common motif used by several endogenous binders to recognize and bind integrins, initiating biological and pathological processes and promoting allosteric changes in the ectodomain required for signal transduction.[1-3]

The study of conformational responses of protein receptors upon the binding of endogenous ligands may be a source of inspiration for the design of small molecule modulators that permit to control such biological processes.

Here we present molecular dynamics simulations of the multidomain receptor αvβ3 integrin bound to two different sequences of the endogenous ligand fibronectin: the wild type one, wtFN10, which acts as an agonist activating the receptor, and a high affinity mutant, hFN10, which acts as a true antagonist inhibiting the receptor.[4] Through the comparative analysis of several dynamic descriptors at different levels of resolution, from the residue to domain level, we shed light on the salient conformational dynamics differences determined by fibronectin sequence mutations: we show that it is possible to identify interaction hotspots in the integrin binding site that specifically respond to the fibronectin sequence variations, and allosterically drive conformational changes towards integrin activation (in the case of wtFN10 binding) or inhibition (hFN10 binding).[5]

Moreover, in recent years a wealth of linear or cyclic peptidic and peptidomimetic integrin ligands has been developed and few potent compounds are in different stages of clinical trials as anticancer drugs (e.g. Cilengitide) or in clinical use for antithrombotic therapy. By means of MD studies, we investigate a new class of cyclic peptidomimetic RGD-based integrin ligands containing bifunctional diketopiperazine scaffolds (cyclo[DKP-RGD] ligands) which showed low nanomolar IC50 values in competitive binding assays to the purified αvβ3 receptor.[6-8]

Different dynamic ensembles of the protein upon ligand-binding unveil the links between the fine atomic-scale protein-ligand interactions and the large-scale protein motions, enabling an allosteric model of integrin regulation that can be used in the design of small molecule integrin inhibitors or modulators.

[1] J. Xiong, et al., Science. 296 (2002) 151–155.
[2] R.O. Hynes, Cell. 110 (2002) 673–687.
[3] J. Takagi, et al., Cell. 110 (2002) 599–611.
[4] J.F. Van Aghtoven, et al., Nat Struct Mol Biol. 4(2014) 383-8.
[5] A. Paladino, et al., PLoS Comput Biol. 13(2017) e1005334.
[6] A.S.M. da Ressurreiçao, et al., Chemistry. 15(2009) 12184-8.
[7] M. Marchini, et al., Chemistry. 18(2012) 6195–07.
[8] S. Panzeri, et al., Chemistry. 21(2015) 6265–71.

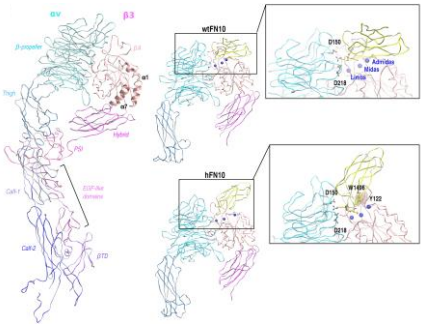

Figure 1. 3D-structure of integrin αvβ3 and αvβ3-FN10 complexes.

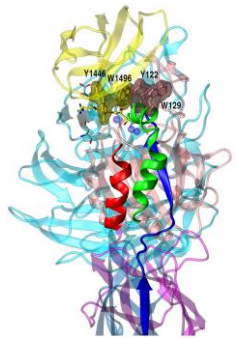

Figure 2. Close-up view of hFN10 complex.

Time-correlated networks of motions in proteins: a basis for spectroscopy-related models of internal dynamics

Paolo Calligari[a,b], Marco Gerolin[a], Daniel Abergel[c], Antonino Polimeno[a]

[a] University of Padua, Padova, Italy
[b] University of Roma "Tor Vergata", Roma, Italy
[c] Ecole Normale Supérieure, Paris, France
e-mail: paolo.calligari@unipd.it

Keywords: protein domain-decomposition, protein dynamics

Amplitudes and time scales of internal motions in proteins can be obtained from spectroscopic observables. However, their interpretation is not straightforward and requires a plausible model of the internal dynamics, which can be based on molecular dynamics (MD) simulations, theoretical models or a combination of the two. In particular, MD simulations can be used to infer useful information on cooperative motions, which can be used afterward to model the dynamics behavior of the protein.
In the proposed method, the clustering of effective correlation times allows to decompose protein structures in terms of time-scale dependent networks of dynamically correlated local domains. This segmentation of the protein on the basis of motion time scales should provide an adaptive strategy for coarse-graining internal motions, depending on the problem (or technique) at hand, and could be used in the derivation of stochastic models for flexible macromolecules. In this context, it may serve as a basis for the development of a unified framework for the derivation of dynamic models that allow to extend the range of time scales accessed by MD simulations.
This approach is of particular interest for the interpretation of spectroscopic data when dynamical processes at different time scales are probed with complementary experimental techniques.
Preliminary results obtained for several prototypal proteins will illustrate this approach.

[1] P. Calligari *et al*, *J Chem Theor and Comp*, 2017, 13 (1), pp 309-319.

First principle calculation of X-ray absorption spectra

Stellato F [a], De Santis [a], La Penna G [b], Minicozzi V [a], Rossi G.C. [a,c], Morante S [a]
[a] Department of Physics University of Rome 'Tor Vergata' and INFN, Roma, 00133, Italy
[b] CNR - Institute for Chemistry of Organometallic Compounds , Sesto Fiorentino, 50019, Italy
[c] Centro Fermi - Museo Storico della Fisica e Centro Studi e Ricerche "Enrico Fermi", Roma, 00184, Italy
e-mail: stellato@roma2.infn.it

Keywords: metal ions, X-ray absorption spectroscopy, density functional theory

The unprecedented progress of high performance computing we are witnessing today offers the possibility of accurate electron density calculations of atomic systems in realistic physico-chemical conditions. Detailed information of this kind is instrumental not only for *ab initio* molecular dynamics simulations, but also for a model-independent interpretation of experimental data.
We present here a strategy aimed at performing a first-principle calculation of the very informative low energy part of the X-ray Absorption Spectroscopy spectrum based on the density functional theory determination of the electronic potential [1].
To test the effectiveness of the approach we have applied the method to the computation of the characteristic features of the X-ray Absorption Near Edge Structure (XANES) part of the XAS spectrum in the paradigmatic case of metal cations, namely Cu(II) and Zn(II), in water solution. In order to keep into account the effect of the metal site structure thermodynamic fluctuations in determining the experimental signal, the theoretical spectrum is evaluated as the average over the computed spectra of a statistically significant number of equilibrated metal site configurations. The agreement of the theoretical spectrum obtained with experimental XAS data is quite good [2].
The remarkable success of this approach in the interpretation of XAS data makes us optimistic about the possibility of extending the computational strategy we have outlined to the more interesting case of molecules of biological relevance bound to transition metal ions. This will be particularly relevant in the study of the metal coordination modes in cases where the metal-protein complex cannot be crystallized, as it happens for the amylogenic proteins involved in the pathogenesis of Alzheimer's disease and transmissible spongiform encephalopathies [3}[4].

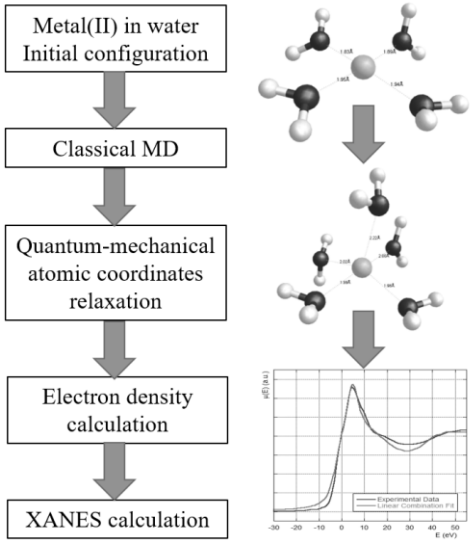

Figure 1. Left panel: the low-chart illustrating the XANES calculation procedure. Right panel: the case of Cu(II) ions in water (right side).

[1] C. Gougoussis, M. Calandra, A.P., Seitsonen, and F. Mauri, F. Phys. Rev. B 80 (2009) 075102.
[2] G. La Penna, V. Minicozzi, S. Morante, G.C. Rossi and F. Stellato J. Chem. Phys. 143 (2015) 124508.
[3] F. Stellato, V. Minicozzi, G.L. Millhauser, M. Pascucci, O. Proux, G.C. Rossi and S. Morante, Eur. Biophys. J. 43 (2014), 631-642.
[4] E. De Santis, V. Minicozzi, O. Proux, G.C. Rossi, K.I. Silva, K., M.J. Lawless.and S. Morante, J. Phys. Chem. B 119 (2015) 15813.

Cavitation enhanced permeability in a bio-inspired micro device

G. Silvani[1,2], R. De Luca[1], C. Scognamiglio[1,3], G. Sinibaldi[1], D. Caprini[1], G. Peruzzi[2], M. Chinappi[4], L. Marino[1], G. Durando[5], M. F. Kiani[6], C.M. Casciola[1,2]

[1] *Sapienza University of Rome, Department of Mechanical and Aerospace Engineering, Rome, Italy*
[2] *CLNS@Sapienza Istituto Italiano di Tecnologia, Rome, Italy*
[3] *Laboratoire de Physique de la Matière Condensée, Université Sophia Antipolis, Nice, France*
[4] *Tor Vergata University of Rome, Department of Industrial Engineering, Rome, Italy*
[5] *INRiM National Institute of metrological research, Turin, Italy*
[6] *Temple University, Department of Mechanical Engineering, Philadelphia, United States*
e-mail : giulia.silvani@iit.it

Keywords: cavitation, ultrasounds, blood-vessel-on-a-chip, drug delivery, permeability

Methods combining focused ultrasounds and microbubbles offer the unique capability of non-invasively, locally e transiently open the endothelial barrier. In general, cavitation is already exploited to locally and transiently open biological barriers in *In vivo* animal models with the advantage to allow studies of therapeutics effects in natural environments [1][2]. Nevertheless, these studies are expensive, time-consuming and difficult to perform. In this context, the need to develop a physiological *in-vitro* model takes place as a necessary and effective clinical trials.

Here, we present a bio-inspired micro-device, specially designed, that enables to investigate the effects of ultrasound-driven microbubbles cavitation. The expected effect is a temporary increase of the barrier permeability due to the increase of inter cellular spaces of the endothelium, allowing drugs to extravasate into tissues of interest.

The bio-inspired micro device consists of a PDMS microfluidic network, see Fig. 1a, with a central circular tissue compartment (1575 µm width, 100 µm height) enclosed by two independent vascular channels (200µm width, 100µm height), mimicking the three-dimensional morphology, size and flow characteristics of micro-vessels *in vivo* [3]. An interface with a series of 3 µm pores, spaced every 50 µm, separates the vascular channels from the tissue chamber. The unique features of the device are the three-dimensional geometry of the vascular channels with realistic size, the correct perfusion rate, the correct physiological shear stress intensity and the ability to reproduce biochemical interactions between different kind of tissues. Moreover, the optically clear microfluidic chip allows for visualization and real time measurements of the dynamic interactions occurring in vascular channels and tissue compartment [3].

It has been developed a reliable and reproducible experimental procedure to culture endothelial cells (HUVECs) within the artificial vessels in physiological conditions (fig.1b). A continuum flow of cellular growth medium, kept at typical blood flow rate and body temperature, is injected to force the cell to take the typical elongated shape in the stream-wise direction, see Fig.1c.

The endothelial membrane permeability is evaluated through a dedicated experimental procedure. Measurements of fluorescent dye diffusion through the pores membrane will be carried out with a 2-hours of time-lapse acquisition, under a confocal microscope operated in epi-fluorescence mode. An image analysis on the intensity change due to fluorescent accumulation in the tissue compartment is performed to obtain to quantify of permeability, see Fig.2a,b.

The same experimental procedure will be adopted to quantify the effect of ultrasound-induced cavitation on permeability. The acoustic setup will consist of an ultrasound transducer driven by a function generator through a power amplifier. Commercial microbubbles (SonoVue®), typically used as contrast agent, will be used. The change of permeability will be obtained in different steps of the experiment, i.e. the free-cell device, the HUVECs cultured device and HUVECs cultured device with microbubbles cavitation.

[1] Konofagou, E. E. et al. Ultrasound-induced blood-brain barrier opening. Curr. Pharm. Biotechnol. (2012).
[2] Kovacs, Z. I. et al . Disrupting the blood–brain barrier by focused ultrasound induces sterile inflammation, PNAS (2016)
[3] Deosarkar, S. P. *et al.* A Novel Dynamic Neonatal Blood-Brain Barrier on a Chip. *PLoS One* (2015)

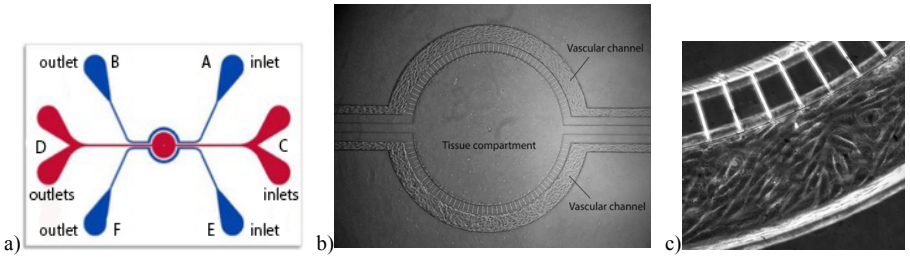

Figure 1 – (a) Sketch of the SynVivo blood-vessel-on-a-chip (b) Bright-field image of the bio-inspired chip cultured with HUVECs. (c) Reconstructed bright-field image: section of the vascular channel with HUVECs. The porous interface is also visible.

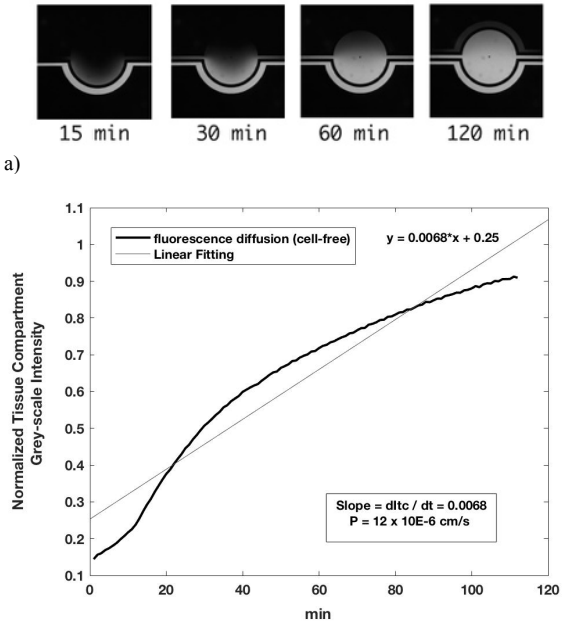

Figure 2 -(a) The time-lapse setting is 1 photo per minute, for a total of 120 photos captured at an exposure time of 90 ms. (b) Quantification of permeability using MATLAB.The slope of the line dI_t/dt is used to calculate the permeability (P).

Pressure Field Around Bubble Break-Up In a T-Junction microchannel From Experimental Velocity Field

Davide Caprini [a], Giorgia Sinibaldi [a], Mauro Chinappi [b], Luca Marino [a], Carlo Massimo Casciola [a,c]

[a] Department of Mechanical and Aerospace Engineering, Sapienza University of Rome , Rome, 00181, Italy
[b] Department of Industrial Engineering, Tor Vergata University of Rome, Rome, 00133, Italy
[c] Italian Institute of Technology, Center for Life Nano Science@Sapienza, Rome, 00161, Italy

e-mail: davide.caprini@uniroma1.it

Keywords: (Microfluidics ,T-junction, µPIV, Bubbles)

In the traditional microfluidics approach, reagents or products are distributed over the single phase flowing in the microchannel. A different approach is the bubble-based or droplet-based microfluidics, where chemical reaction are confined in small bubbles or droplets, allowing for strong reduction of reaction volume and time in biochemical processes [1]. In particular, the study of the gas-liquid two-phase flow, it is of fundamental importance in biological applications to calibrate the amount of gas, or size and speed of microbubbles in microdevice, used in the manufacture porous materials, or in the dissolved gas in biological control flows. Bubbles are generated by mixing a secondary gaseous stream with the main liquid flow, e.g. by using a T-junction configuration. Controlling size and frequency of the bubbles is essential to achieve well-defined and reproducible regimes [2]. The pressure field, which is crucial for bubble break-up, remains an elusive quantity, usually estimated from theoretical considerations or numerical simulations [3,4,5]. Here, the bubble break-up process is investigated using micro Particle Image Velocimetry (µPIV) together with high-speed imaging. The purpose is to evaluate the pressure field around the bubble during the break-up instant by post processing the experimentally measured velocity fields.

The experimental set-up (Fig.1) consists of an inverted microscope (Zeiss Observer Z1) combined with µPIV, based on a Nd:YAG double-pulse laser (Litron NanoPIV) at 532 nm. A dual frame camera (SX-4) captures pairs of images to be post processed using the LaVision Davis software. The continuous phase is seeded with polystyrene fluorescent particles of different diameters (D = 1.47-5.47 µm). Some tests on the influence of the particles on the capillary number have been performed, to recognize the correct bubble generation regime (Fig.2 and Fig3). Several commercial and laboratory-manufactured chips are tested and compared. The microfluidic network is supplied by a syringe pump (PHD Ultra-Harvard) for the liquid phase and a pressure pump (Dolomite Mitos P-Pump) for the gas phase. The set-up has been validated by comparing the threshold capillary number with reference results for stable bubble flow rate [3].

Two dimensional velocity fields around the developing bubble were acquired on different focal planes. For each acquisition the bubble interface was reconstructed by image analysis to enable phase locked averaging of the velocity fields (Fig.4). From this information, the symmetry plane is identified and the two principal curvatures of the bubble are estimated, to try to evaluate the pressure at the bubble interface. Interesting preliminary results have been obtained in small regions close to the interface and we are presently working to extend the analysis to the whole region around the bubble.

[1] Hao Gu, Michel H.G. Duits and Frieder Mugele, Droplets Formation and Merging in Two-Phase Flow Microfluidics,(2011) Int. J. Mol. Sci.
[2] Garstecki, P.; Fuerstman, M.J.; Stone, H.A.; Whitesides, G.M. Formation of droplets and bubbles in a microfluidic T-junction-scaling and mechanism of break-up.(2006) Lab Chip 2006.
[3] J K Nunes, S S H Tsai, J Wan, and H A Stone, Dripping and jetting in microfluidic multiphase flows applied to particle and fiber synthesis. (2013)J Phys D Appl Phys.
[4] By M. De Menech, P. Garstecki, F. Jousse and H. A. Stone, Transition from squeezing to dripping in a microfluidic T-shaped junction.(2008) Journal of Fluid Mechanics.
[4] Gim Yau Soh, Guan Heng Yeoh, Victoria Timchenko, Numerical investigation on the velocity fields during droplet formationin a microfluidic T-junction. (2016)Chemical Engineering Science.

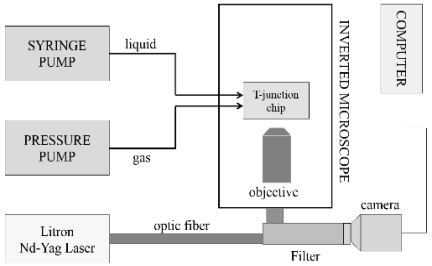

Figure 1. Scheme of experimental set-up.

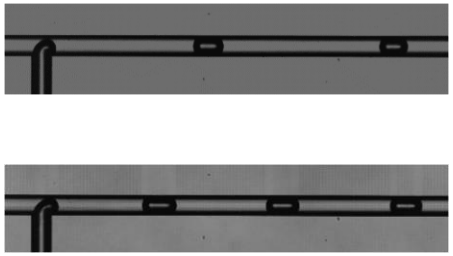

Figure 2. Example of squeezing regime to validate the set-up at different regimes (5x objective; 20000fps).

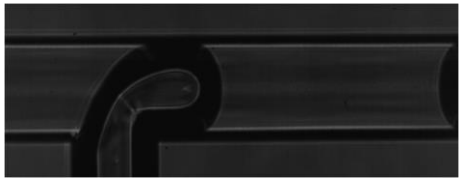

Figure 3.Snapshot of bubble break-up (channel width 110 µm; 20x objective; 40000 fps).

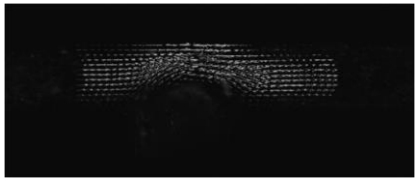

Figure 4. Example of average velocity field around bubble during break-up.

Bragg curve imaging of 6.75 MeV protons with lithium fluoride crystals and fluorescence microscopy

E. Nichelatti [a], M. Piccinini [b], A. Ampollini [b], L. Picardi [b], C. Ronsivalle [b], F. Bonfigli [b], M.A. Vincenti [b], R.M. Montereali [b]

[a] ENEA C.R. Casaccia, Fusion and Technologies for Nuclear Safety and Security, Via Anguillarese 301, S. Maria di Galeria, Roma, 00123, Italy
[b] ENEA C.R. Frascati, Fusion and Technologies for Nuclear Safety and Security, Via E. Fermi 45, Frascati (RM), 00044, Italy
e-mail: enrico.nichelatti@enea.it

Keywords: proton therapy, Bragg curve, lithium fluoride, colour centres, luminescence

Use of hadrons in oncological radiotherapy has seen a remarkable growth in recent years due to the excellent ballistic properties of heavy particles, which release most of their energy at the end of their path [1]. A linear accelerator for proton therapy is under development at ENEA C.R. Frascati in the framework of the TOP-IMPLART Project carried out by ENEA in collaboration with ISS and IRE-IFO [2]. Even though still below clinically relevant energies, the proton beam has been already characterised thanks to collaborations with scientific and industrial partners. In this context, lithium fluoride (LiF) crystals have been proposed and used as luminescent radiation detectors for Bragg curve imaging [3].

LiF is an alkali halide material with peculiar physical and optical properties, useful for applications in optoelectronics, integrated optics as well as in X-ray imaging and dosimetry [4], thanks to its tissue equivalency. It can host laser-active electronic defects, known as colour centres (CCs), characterised by wide tunability and good stability even at room temperature [5].

Irradiation of LiF by ionising radiation of various kinds induces the formation of CCs, mainly the primary F centre (an anionic vacancy occupied by an electron) and the aggregate F_2 and F_3^+ CCs (two electrons bound to two and three anion vacancies, respectively). The F_2 and F_3^+ CCs possess almost overlapping broad absorption bands, centred at a wavelength of ~450 nm, known as M band [5]. By optically pumping in the M band, the F_2 and F_3^+ CCs simultaneously emit broad photoluminescence (PL) bands peaked at 678 nm and 541 nm, respectively [6].

In this work, it is shown how Bragg curves of the TOP-IMPLART proton beam are recorded and stored as latent fluorescent images in LiF. A preliminary study was recently published by using LiF thin films as radiation detectors [7]; here, results regarding irradiation of LiF crystals with 6.75 MeV protons are reported for the first time.

In the experiment, 10×10 mm^2, 1 mm thick polished LiF crystals are longitudinally placed along the path of the proton beam to create a depth distribution of CCs in the material. The PL radiated by F_2 and F_3^+ CCs belonging to this distribution is detected by a Nikon Eclipse 80-i C1 fluorescence microscope under blue lamp illumination, and stored in a computer as an image acquired by a s-CMOS camera. An example of such an image is shown in Fig. 1 for an irradiation with 6.75 MeV protons. In it, the segment AB indicates a one-dimensional PL profile that is later used for comparison with theory. To this purpose, Monte Carlo simulations of linear energy transfer (LET) profiles are performed with SRIM software [8]. The calculated LET profiles – Fig. 2 shows one of them corresponding to 6.75 MeV protons passing through a 50 μm thin Kapton window, 5 mm in air, and then entering LiF bulk – are not directly comparable with the experimental PL depth profiles, although the Bragg peak position is the same. Therefore, the SRIM output is elaborated within a Matlab code to take into account (a) the proton beam energy spread, and (b) the PL vs. dose relationship, including saturation effects due to high CC concentration. Indeed, the detected PL signal cannot be considered as linearly dependent on the absorbed dose above a certain threshold, see Fig. 3. Figure 4 shows the resulting theoretical PL profile (again, for 6.75 MeV protons) compared with the corresponding experimental profile of segment AB in Fig. 1.

Research carried out within the TOP-IMPLART (Oncological Therapy with Protons—Intensity Modulated Proton Linear Accelerator for RadioTherapy) Project, funded by Lazio Innova, Italy.

[1] A. Tamborini et al., Nucl. Instrum. Methods A 815 (2016) 23.
[2] C. Ronsivalle et al., Eur. Phys. J. Plus 126 (2011) 68.
[3] M. Piccinini et al., J. Lumin. 156 (2014) 170.
[4] R.M. Montereali et al., J. Lumin. 170 (2016) 761.
[5] J. Nahum and D.A. Wiegand, Phys. Rev. 154 (1967) 817.
[6] G. Baldacchini et al., J. Phys. Chem. Solids 61 (2000) 21.
[7] R.M. Montereali et al., IOP Conf. Ser.: Material Science and Engineering 169 (2017) 012012.
[8] J.F. Ziegler et al., Nucl. Instrum. Methods B 268 (2010) 1818.

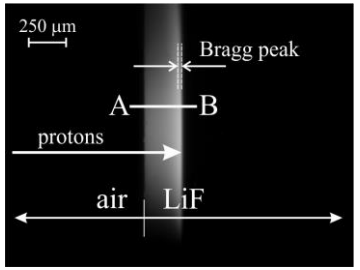

Figure 1. PL image, as detected by a fluorescence microscope with a s-CMOS camera, due to F_2 and F_3^+ CCs formed in a LiF crystal irradiated with 6.75 MeV protons.

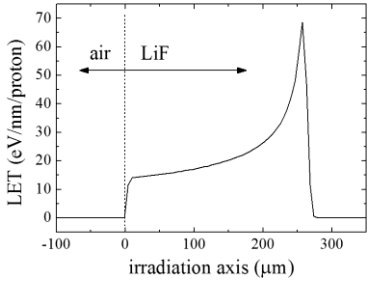

Figure 2. Monte Carlo simulated depth profile of the energy released by 6.75 MeV protons into the LiF bulk material.

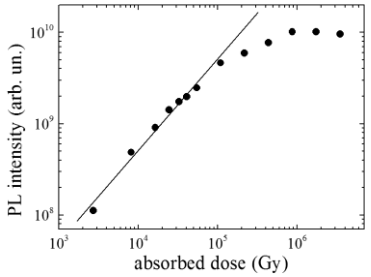

Figure 3. Experimental spectrally integrated PL intensity of CCs formed at various doses in a LiF crystal by irradiation with 6.75 MeV protons. Saturation at doses above ~10^5 Gy can be clearly seen. The superimposed straight line evidences the linear part of the curve.

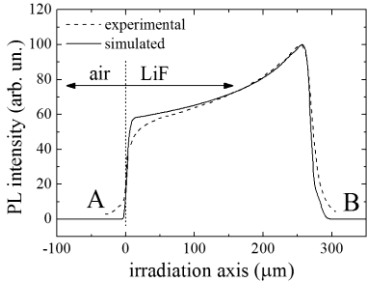

Figure 4. Comparison of the experimental PL profile corresponding to AB in Fig. 1 with its simulated counterpart, obtained by elaborating in Matlab a number of LET profiles resulting from SRIM calculations, and also by taking into account the saturation shown in Fig. 3.

A novel coplanar layout enabling accurate microfluidic impedance cytometry

A. De Ninno [a], V. Errico [a], F.R: Bertani [b], L. Businaro [b], P. Bisegna [a], F. Caselli [a]

[a] Dept. of Civil Engineering and Computer Science, University of Rome Tor Vergata, Rome, 00133, Italy
[b] Institute for Photonics and Nanotechnologies, Italian National Research Council, Rome, 00156, Italy
e-mail: caselli@ing.uniroma2.it

Keywords: microfluidic impedance spectroscopy, single-cell analysis, coplanar electrode layout

Single-cell impedance cytometry is a non-invasive method for characterizing individual cells and particles [1, 2]. A microfluidic impedance chip typically consists of a microchannel equipped with microelectrodes and filled with a conductive buffer. An AC voltage is applied to a pair of electrodes, which causes a current to flow between them. The current change upon passage of a cell between the electrodes is measured and then analysed to determine cell properties. Coplanar chip layouts are especially attractive, because coplanar electrodes can be easily patterned yielding miniaturized, reproducible, and ultimately low-cost devices. However, their accuracy is challenged by the dependence of the measured signal on particle trajectory, which manifests itself as an error in the estimated particle size, unless any kind of focusing system is used.

The aim of this work is to present a new, easy-to-realize microfluidic impedance chip able to provide high-accuracy size estimation without the need for focusing [3, 4]. The device uses a chip with coplanar electrodes, and its operation mode is conceived such that a peculiar electric field distribution is generated within the sensing region. Consequently, the signal trace recorded upon the passage of a particle exhibits a characteristic shape, from which a new metric can be extracted correlating with particle trajectory height (Figures 1 and 2).

As proved by numerical and experimental campaigns, the new metric can be used to compensate for the spurious spread in the measured electrical size, thus achieving high accuracy (Figures 3 and 4).

The easiness of fabrication of coplanar electrodes coupled with the increased accuracy achieved by the proposed methodology make the resulting device a simple and effective tool for label-free particle analysis, with potential applications in medicine, life science and quality control.

[1] K.C. Cheung, Cytometry Part A 77 (2010) 648-666, doi: 10.1002/cyto.a.20910.
[2] T. Sun and H. Morgan, Microfluid. Nanofluid. 8 (2010) 423-443, doi: 10.1007/s10404-010-0580-9.
[3] A. De Ninno et al., Lab Chip 17 (2017) 1158-1166, doi: 10.1039/c6lc01516f.
[4] V. Errico et al., Sens. Actuators B: Chem, 247 (2017) 580-586, doi: 10.1016/j.snb.2017.03.035.

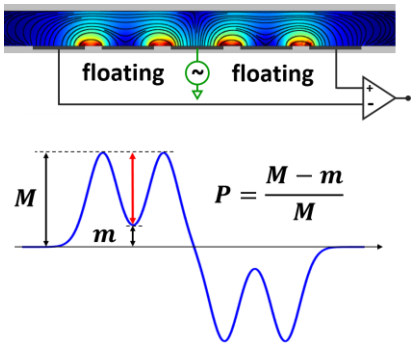

Figure 1. AC excitation signals are applied to the central electrode, and the difference in current flowing through the lateral electrodes is measured, with intermediate electrodes floating. Weak-field regions are generated in front of the floating electrodes, yielding a bipolar double-Gaussian profile of the measured current. The definition of relative prominence P is shown.

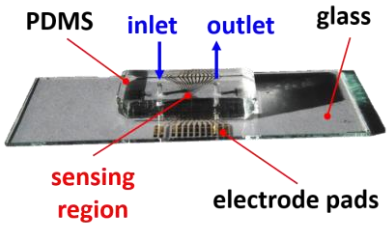

Figure 2. Microfluidic impedance chip, consisting of a PDMS fluidic top layer and patterned coplanar microelectrodes on glass. In the sensing region, the microchannel cross-sectional area is 40 µm (w) × 21 µm (h). The sensing electrode width is 30 µm, and the spacing between them is 10 µm.

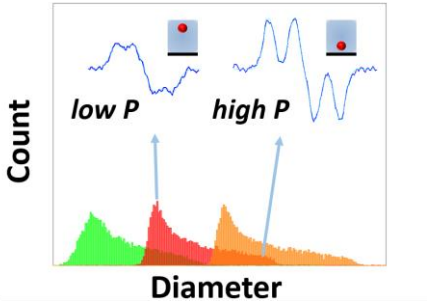

Figure 3. The histogram of the electrical diameters of 5 (green), 6 (red), and 7 (orange) um beads exhibit spread and asymmetry. Particles traveling near the electrodes (having high prominence P) provide larger diameters than particles traveling far from the electrodes (exhibiting low prominence P).

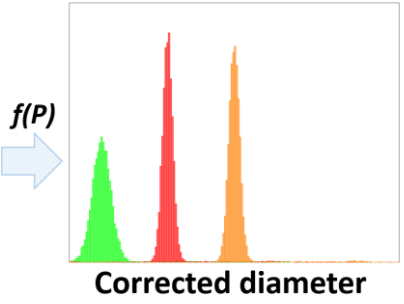

Figure 4. After applying a compensation procedure based on the relative prominence P, 5 (green), 6 (red), and 7 (orange) um beads exhibit low CV Gaussian electrical diameter distributions, and therefore can be properly discriminated by size.

Nanotomography and X-Ray Fluorescence Microscopy for quantitative Iron concentration map in inflamed cells

Chiara Gramaccioni [a,d], Alessandra Procopio [b], Andrea Notargiacomo [c], Michela Fratini [d,e], Alexandra Pacureanu[f], Yang Yang[f], Emil Malucelli[b], Stefano Iotti[b], Peter Cloetens[f], Sylvain Bohic[f], Piera Valenti[g], Luigi Rosa[g], Francesca Berlutti[g] and Stefano Lagomarsino[d].

[a] Dept. of Physics Univ. of Cosenza, Arcavata di Rende (Cosenza), 87036, Italy
[b] Dept. of Pharmacy and biotechnology Univ. Bologna, Bologna, 40126, Italy
[c] Institute for Photonics and Nanotechnologies - CNR, Roma, 00185 Italy
[d] CNR-Nanotec c/o Dept. of Physics Univ. Sapienza, Roma, 00185, Italy
[e] Fondazione Santa Lucia, Roma, 00179, Italy
[f] ESRF, Grenoble, 38043, France
[g] Dept. of Public Health and Infectious Diseases Univ. Sapienza, Roma, 00185 Italy
e-mail: chiara.gramaccioni@gmail.com

Keywords: (Nanotomography, X-ray Fluorescence Microscopy, Intracellular Fe, Human THP-1 macrophages cells, Phase Contrast Imaging, Atomic Force Microscopy)

Iron is a primary component of fundamental processes in the cell. However, iron can become toxic when present in excess because of its capacity to don electrons to oxygen, thus causing the generation of reactive oxygen species, such as superoxide anions and hydroxyl radicals. In human fluids, free iron is maintained at 10^{-18}M concentration thanks to several proteins as lactoferrin (LF) in secretions and transferrin in blood. The altered iron balance favors bacterial infection and the related inflammatory response as occurs in cystic fibrosis [1,2]. Therefore, it is of great importance to provide quantitative mapping of iron concentration at high spatial resolution. Here we studied human phagocytic cells unstimulated or stimulated with bacterial lipopolysaccharide (LPS) or/and Lf to map the intracellular density and iron concentration. For this aim, X-ray fluorescence microscopy (XRFM), atomic force microscopy (AFM), X-ray phase contrast imaging and Phase Contrast Nanotomography were combined. In a recent paper [3, 4], we have demonstrated that it is possible to merge compositional and morphological information to quantitatively derive the element concentration combining XRFM with Atomic Force Microscopy (AFM). Here we aim to demonstrate that it is possible to quantitatively derive the elemental concentration combining XRFM with phase contrast nanotomography. The nanotomography is of paramount importance to reach the volumetric information in frozen-hydrated cells because AFM cannot be used since frozen hydrated cells are stored in liquid nitrogen. Combination of these techniques makes possible accurate description of compositional and structural cell features. The XRFM and phase contrast measurements 2D/3D have been carried out at the beamline ID16A-NI at ESRF, with the spatial resolutions of 100 nm and 50 nm, respectively; the volume of freeze-dried cells has been obtained by AFM with lateral resolution of 100 nm. To determine the concentration map we normalized the fluorescence intensity with the volume of the illuminated region (Fig.1). Moreover, we determined the weight fraction distribution map, normalizing the fluorescence intensity with the projected density obtained by phase contrast imaging (Fig.2) [5]. Indeed, we obtained the density distribution of the cells (Fig.3) by normalizing phase reconstruction maps with AFM data. Similar evaluations were carried out for LF- and LPS plus LF-treated cells. We also carried out nanotomography measurements, to obtain the iron three-dimensional density distribution (Fig.4). We succeeded for the first time in deriving quantitative concentration maps from combined use of XRFM and Phase Contrast nanotomography at nanometer scale spatial resolution (Fig.5). To obtain the thickness map from nanotomography we have not used the reconstructed tomographic image in terms of representation of the local electron density; instead, we have used it to obtain a morphological segmentation of the cell [6], and then we projected along the thinnest direction of this 3D mask. We obtained the thickness map from nanotomography by summing along the short axis and converting the pixel size into micrometres. It is worth to note that in the case of freeze dried cells the ratio between thickness and lateral dimension is very small, and this makes the quantitative derivation of cell thickness more difficult. In this work, we have demonstrated that it is possible to obtain the distribution map of the major cell components (as Iron, Phosphorus and Potassium), using XRFM, and the volume information obtained by phase contrast nanotomography or AFM. This work opens the way to quantitative biological analysis at nanometre spatial resolution using synchrotron radiation Imaging techniques. This makes possible to study of frozen hydrated cells as well, in case AFM cannot be used (Fig6).

The research was granted by Sapienza University of Rome to PV and FB and by a STSM of the Cost 1207.

[1] R. Paesano et al. Pathogens and Global Health 2012, 106, 200.
[2] P. Valenti et al., Lactoferrin and cystic fibrosis airway infection. In: Diet and Exercise in Cystic Fibrosis. 2015, 30, 259
[3] S. Lagomarsino et al., Spectrochim. Acta B 2011 66, pp767-866
[4] E. Malucelli et al., Anal. Chem., 2014, 86 , pp 5108–5115
[5] E. Kosior et al.,. J. Struct. Biol. 2012 177(2):239-47
[6] Gramaccioni et al. Combined use of x-ray fluorescence microscopy, phase contrast imaging for high resolution quantitative iron mapping in inflamed cells, accepted for publication n Journal of Physics: Conference Series (JPCS), for the XRM2016 conference proceedings.

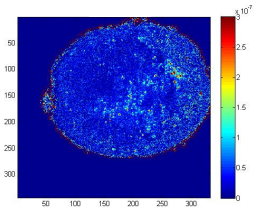

Figure 1. Iron concentration map [nM] of cell treated with LPS.

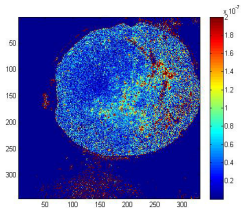

Figure 2. Iron Weight fraction distribution map of cell treated with LPS.

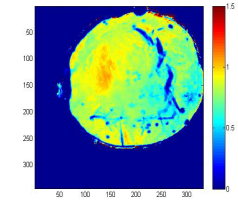

Figure 3. Density distribution map [g/cm^3] of cell treated with LPS.

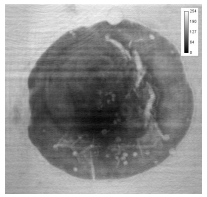

Figure 4. Density Map 3D from Nanotomography [g/cm^3] of cell treated with LPS.

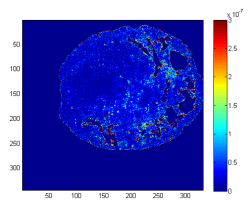

Figure 5. Iron Concentrations maps from Nanotomography [nM] of cell treated with LPS.

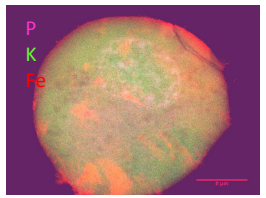

Figure 6. Fluorescence intensity Composite Map of frozen hydrated control cell.

Nano-mechanical characterization of human brain tumor

Minelli E. [a], *Ciasca G.* [a], *Sassun T.E.* [b], *Antonelli M.* [c], *Papi M.* [a], *Santoro A.* [b], *Giangaspero F.* [c,d], *Delfini R.* [b°], *De Spirito M.* [a°]

[a] Istituto di Fisica, Universita Cattolica del Sacro Cuore, Largo F. Vito 1, 00168 Rome, Italy
[b] Department of Neurology and Psychiatry, Neurosurgery, Sapienza University, 00181 Rome, Italy
[c] Department of Radiological, Oncological and Anatomo Pathological sciences, Sapienza University, Rome, Italy
[d] IRCSS Neuromed, Pozzilli (IS), Italy.
° These authors share equal credit for seniorship
e-mail: minelli.eleonora@gmail.com

Keywords: cancer microenvironment, biomechanics, AFM

It is already becoming apparent that the mechanical properties of cells and their microenvironment may profoundly affect tissue homeostasis. In physiological conditions, cells are susceptible to physical and mechanical forces, mediated by the extracellular matrix (ECM), which play a fundamental role in the development and maintenance of organs and tissues. The perturbation of this biophysical interplay between cells and ECM has therefore emerged as a key signaling pathway regulating diseases growth and progression. Tumour onset and advancement indeed influenced, and are influenced by, modifications in the mechanical properties of cells and their surrounding ECM [1].

Atomic Force Microscopy (AFM), have allowed scientists to probe the mechanical properties of cells and tissues, demonstrating that cancer cells in vitro are softer than their healthy counterparts, while cancer tissues appear to be significantly stiffer than healthy ones. The cellular modified deformability is associated to alterations in the cytoskeletal architecture and it is strictly related to their malignant behavior, instead, the tumor tissue rigidity is due to the accumulation of ECM fibrous protein, such as collagen, laminin, and fibronectin[2-3].

This is particularly true in the case of glioblastoma multiforme (GBM), a highly invasive brain tumor with a unique infiltrative pattern, strictly related the typical composition of the brain ECM[4]. In this work, we provide the first study of the nano-mechanical properties of human GBM tissue, obtained after surgical resection. In order to achieve a more in-depth understanding of the role of the mechanical landscape, we investigated Young's modulus (E), to obtain information about the tissue elasticity, and the Hysteresis (H), the energy dissipated during the indentation cycle, to quantitatively evaluated the role of the viscous forces. We compared the GBM results with that of human meningothelial meningioma (MM) tissue, a benign brain lesion which does not infiltrate the normal parenchyma.

Normal brain ECM is composed of glycosaminoglycan, hyaluronan, and proteoglycans, and it is very soft with an average Young's modulus of 1-2 kPa (fig 1a) and high H value, while both GBM and MM microenvironment are characterized by high rigidity 10 kPa and 15 kPa, respectively, and lower Hysteresis values (fig. 2).

The stiffness increase of GBM tissue is related to its spread mechanism; GBM cells motility is higher on stiff structures, so they actively modify their microenvironment. Moreover, being GBM a high-grade tumor, necrosis is always present and it is a hallmark for the diagnosis. We provide the mechanical characterization of necrosis, finding out an extremely low Young's modulus and high viscous behavior, E~300 Pa H ~ 0.7 (fig.1b)

These results confirm the important role played by the mechanical cues in the spreading and the progression of brain tumors, further stressing the need to elucidate the mechanical modifications occurring during the genesis and progression of the pathology. In this regard, it is important to evaluate the key role played by the extracellular microenvironment We report a comprehensive study on the nano-mechanical properties of human GBM and MM tumor tissues obtained after surgical resection and analysed by indentation-type atomic force microscopy (IT-AFM).

[1] Suresh, S. Acta Materialia 55, 3989-4014 (2007)
[2] Alibert, C., et.al Biology of the Cell (2017).
[3] Plodinec, M., et al. Nature nanotechnology 7.11 (2012): 757-765.
[4] Ciasca, G., et al. Nanoscale 8.47 (2016): 19629-19643.

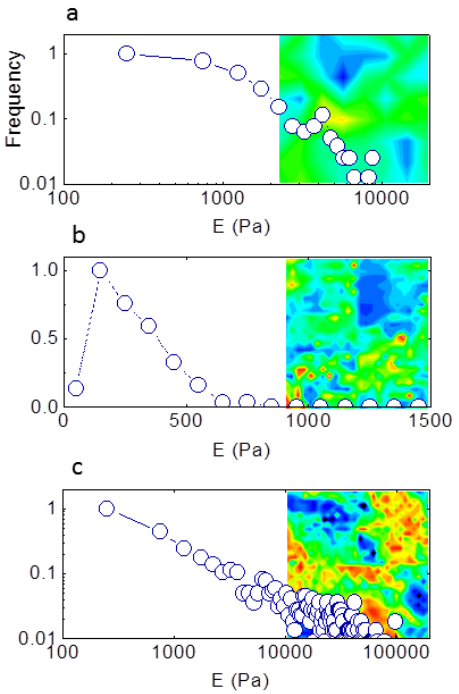

Figure 1. Normalized frequency histogram of the apparent Young's modulus and the relatives maps. a) healthy brain tissue, b) GBM necrosis, c) GBM tumor tissue.

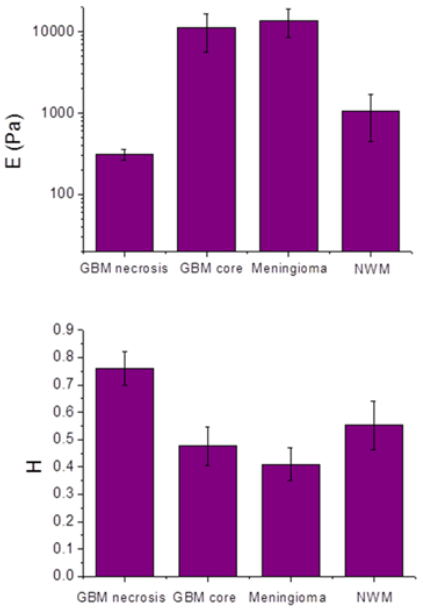

Figure 2. Average E and Hysteresis value for GBM necrosis, GBM tumor tissue, meningioma and normal white matter (NWM)

RECOMBINANT E6 ONCOPROTEINS OF DIFFERENT HUMAN PAPILLOMAVIRUSES: NOVEL TOOLS FOR HPV TUMOR DIAGNOSIS

Elena Illiano [a], Rosella Franconi [b], Antonio Rinaldi [a]

[a] NANOFABER s.r.l , Via G.A. Badoero 82, 00154, Rome, Italy
[b] ENEA, Casaccia Research Center, Department for Sustainability, Via Anguillarese 301, 00123, Rome, Italy
e-mail: elena.illiano@nanofaber.com

Keywords: (HPV, E6 oncoprotein, Biomarker, Diagnostic)

High-risk human papillomaviruses (HR-HPVs) types 16 and 18 are the main etiological agents of cervical cancer, with more than 550.000 new cases each year worldwide. HPV16 and HPV18 have also been shown to cause almost half the vaginal, vulvar, and penile cancers, while about 85% of anal cancers are also caused by HPV16 [1]. HPVs, and HPV16 in particular, are associated with some head and neck squamous-cell carcinomas, and they are an independent risk factor for oropharyngeal cancers [2].
The HR-HPV E6 and E7 oncoproteins are responsible for onset and maintenance of the cell transformation state, and they represent appropriate targets for the development of new diagnostics.
Moreover, in the last years, HPV16 E6 serology was identified as a promising pre-diagnostic marker for HPV-driven cancers, as HPV16 E6 seropositivity has been found more than 10 years before diagnosis of oropharyngeal cancers [3]. It is also important to note that seropositivity is relatively common before diagnosis of anal cancer, although it is rare for other HPV-related ano-genital tumors [4].
Recombinant E6 protein is extremely difficult to obtain in a soluble and active form. We set up a protocol for the production of soluble Histidine-tagged E6 protein (His_6-E6), from HPV-16, -18, -11, in native conditions from bacteria. [5].The structural properties of HPV16 His_6-E6 were determined using circular dichroism and fluorescence spectroscopy and suggest that the protein maintains correct folding. His_6-E6 oncoprotein immunogenicity was assessed in a mouse model showing a significant humoral immune response. The E6 proteins from HPV16, HPV18, and HPV11 were purified according to a new procedure and investigated for protein–protein interactions. Its functionality was determined using *in vitro* GST pull-down and protein degradation assays. HR-HPV His_6-E6 bound p53, the PDZ1 motif from MAGI-1 proteins, the human discs large tumor suppressor (hDLG) and the human ubiquitin ligase E6-associated protein (E6AP), thus suggesting that they are biologically active. The purified HR-HPV E6 proteins also targeted the MAGI-3 and p53 proteins for degradation. Moreover, we demonstrated that our HPV-16 E6 protein is stable at + 4 °C for at least 2 years [6].
This new procedure can be useful to prepare the E6 protein to promote its industrial production for diagnostic tests. With this aim, the maintenance of the native conformation of the E6 protein should improve the specificity, costs, precision, and reproducibility in the detection of anti-E6 antibodies in patient sera.
Our goal is the development of a simple,rapid,reliable,portable,low-cost diagnostic kit, based on direct/indirect detection of E6 biomarker, which is expressed at high levels in samples only when HPV-infected cells undergo precancerous and cancerous changes.
Ongoing experiments to immobilize HPV E6 proteins on chips based on elettrospun biopolymers, for the detection of serum antibodies in patients, will be reported.

[1] D.P. Zandberg *et al*., Cancer J Clin. (2013) 57–81
[2] M.J. Worsham *et al*., Mol Diagn Ther. (2012) 209–22
[3] A.R. Kreimer *et al*., J Clin Oncol. (2013) 2708–15
[4] A.R. Kreimer *et al*., J Clin Oncol. (2015) 877–84
[5] R. Franconi & E. Illiano (2007) Brevetto Italiano n. 1379103
[6] Illiano *et al*. J Transl Med (2016) 14:224

Protocol	Temperature (°C)	Dithiothreitol (μM)	pH	Imidazole (mM)			Detergent[a]
				Lysis buffer	Wash buffer	Elution buffer	
A	Room temperature	–	8	10	20	250	–
B	4	100	8	10	25	250	–
C	4	100	8	20	50	250	–
D	4	100	7.5	20	70	300	–
E	4	100	7.5	20	70	300	0.02 % lauryl-β-D-maltoside 0.02 % Tween-20 0.02 % glycine 0.02 % betaine 0.1 M arginine
F	4	100	7.5	20	70	300	0.02 % betaine

[a] The detergents listed were tested individually

Figure 1. Table of Chemical and physical parameters analyzed during the purification of the HPV16 His_6-E6 protein under native conditions

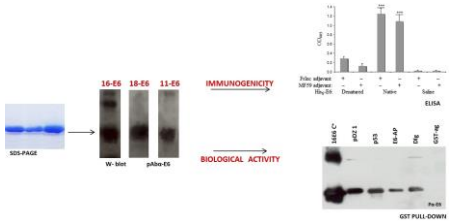

Figure 2. Purification of the His_6-E6 proteins from HPV16 18 and 11 under native conditions. Anti-E6 humoral responses in mice. Physical interactions between the purified HPV16 His_6-E6 protein and its cellular targets.

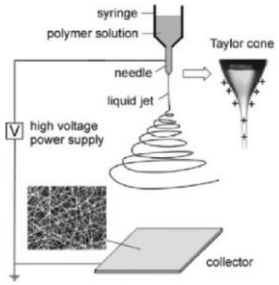

Figure 3. Schematics of electrospinning setup

Figure 4. Prototype chip for detection of serum antibodies in patiens

Biosensors for Endogenous Lipids

S. Grasso [a], G. Pennazza [a], T. Bisogno [a,b], M. Santonico [a], M. Maccarrone [a,c*]

[a] Campus Bio-Medico University of Rome, 00122 Rome, Italy
[b] Endocannabinoid Research Group, National Research Council, 80078 Pozzuoli, Italy
[c] Santa Lucia Foundation, Via del Fosso di Fiorano 64, 00143 Rome, Italy
[*] E-mail: m.maccarrone@unicampus.it

Keywords: endocannabinoids, biosensor, BIONOTE

The endocannabinoid system comprises endogenous lipid mediators (endocannabinoids, eCBs) like *N*-arachidonoylethanolamine (anandamide, AEA) and 2-arachidonoylglycerol (2-AG), along with their specific G protein-coupled type-1 (CB_1) and type-2 (CB_2) cannabinoid receptors, and the proteins responsible for eCB biosynthesis, inactivation, transport, and accumulation [1]. Growing evidence suggests that eCB levels might be modulated during pathological conditions affecting both central and peripheral nervous system [2]. The understanding of the biological significance of eCBs would not be possible without the development of methods for the accurate, precise, and sensible detection and quantification of these molecules in cells, tissues and biological fluids. Unfortunately, the currently available gold standard for eCB detection is liquid chromatography-mass spectrometry (LC-MS), a technique that, although highly sensitive, is expensive and rather sophisticated [3].

In the present study, a novel approach based on an innovative liquid biosensor has been used to analyse relevant eCBs: the BIONOTE device. The latter is composed of a probe and a dedicated electronic interface devoted to supply a variable input signal and to record the related output data [4]. The signal input consists of a triangular waveform between -1V and 1V and a frequency of 10 mHz while the output signal is the current response to a specific voltage input value. When the sensor probe is immersed in a solution, a current related to the oxy-reductive reactions occurring in the sample is recorded. Data is acquired with a sampling rate of 200 milliseconds, thus collecting 500 output values for each measuring cycle. The whole registered data array is treated as a global pattern with an enriched informative content representing the electrical signature of the analysed sample. The complex data set is finally analysed through multivariate data analysis techniques to provide a simplified representation of the multidimensional space acquired and to highlight the most informative features. Partial Least Square Discriminant Analysis (PLS-DA) coupled with the Leave-One-Out criterion as cross-validation method has been employed to obtain all the predictive models onto the calibration data. As a preliminary approach to eCB quantification, standards of the two most representative members of this lipid family have been analysed by the liquid sensor under controlled conditions. AEA and 2-AG were suspended in methanol at millimolar concentration and were measured through the BIONOTE, independently of each other. Despite the device was able to detect qualitatively both molecules, the micromolar error associated with the calibration curve was too large to allow detection of these eCBs at physiological levels. Due to the natural affinity to bind lipids circulating in blood, bovine serum albumin (BSA, fatty acid free) was selected as a candidate to attempt probe functionalization with the aim to improve the sensibility of the whole analytical system. A thin film of agarose gel containing 1 mg of BSA was then deposited by drop casting technique onto the surface of the probe, and then it was let to air dry. The modified probes were left to soak for 10 minutes in the target solution before starting the analysis. This process forced the dissolved lipids to move together with the solvent toward the dry BSA film where these got trapped by the binding with the serum protein. By means of this experimental setup we were able to increase the eCB concentration specifically at the probe interface. By challenging the BIONOTE with different amounts of eCBs to draw calibration curves in the 1 µM to 1 nM concentration range, and then applying a linear regression model to the experimental data, the system was able to predict both AEA and 2-AG concentrations with a Root Mean Square Error in Cross Validation (RMSECV) of 6.61 nM and 23.50 nM respectively. In addition, to test the discriminating performance of the analytical system against the eCBs, two molecules sharing part of the chemical structure of AEA and 2-AG were analysed: ethanolamine and glycerol. These substances were measured at the same concentrations as AEA and 2-AG, replicating the experimental setup. Also in this case, BIONOTE was able to predict the specific molecule concentration with an RMSECV of 4.47 nM and 20.73 nM, respectively. Finally, a comprehensive array containing the overall sensors' responses was built, and collected data were analysed through multivariate data analysis. The calculated PLS-DA models highlighted the ability of the system to distinguish the 4 standard molecules with an efficiency of 100% in the classification.

In conclusion, we report for the first time the development of an innovative lipid biosensor able to assess eCB content. Although our electronic device needs to be further validated by comparing its outcomes with those obtained by classical LC-MS analysis, the exploitation of sensors as suitable devices for high throughput screening of bioactive lipids has an apparent diagnostic potential for tomorrow's medicine.

[1] Maccarrone, M. *et al*. Nat Rev Neurosci 15 (2014) 786-801. [2] Di Marzo, V. Nat Rev Drug Discov. 7 (2008) 438-55. [3] Bisogno, T. *et al*. Eur J Lipid Sci Technol 111 (2009) 53–63. [4] Santonico, M. *et al.* Sensors 13 (2013) 16625-16640.

Acknowledgements. This investigation was supported by MIUR under competitive PRIN 2015 grant to M.M.

Figure 1. Probe functionalization procedure.

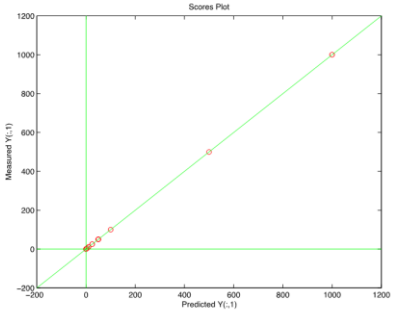

Figure 2. Predicted model obtained by a PLS-DA model. The device has been calibrated to AEA at concentration values ranging from 0 to 1 µM.

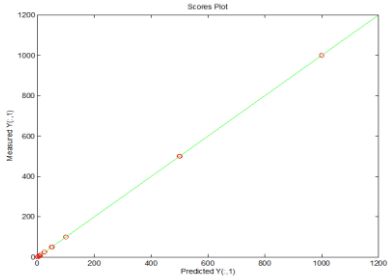

Figure 3. Predicted model obtained by a PLS-DA model. The device has been calibrated to 2-AG at concentration values ranging from 0 to 1 µM.

Principal Component Analysis of Raman spectra of red blood cells to study biochemical signature of ageing process

E. Lenzi[1], S. Dinarelli[2], G. Longo[2], M. Girasole[2], V. Mussi[3]

[1] Physics Department, University of Rome Tor Vergata, Rome
[2] Institute of Structure of Matter, National Research Council, Rome
[3]Institute of Complex Systems, National Research Council, Rome
e-mail: elisa.lenzi91@gmail.com

Keywords: erythrocyte, ageing, Raman spectroscopy, AFM

Red blood cell's (RBC) ageing is a physiological process, fundamental to ensure a proper blood homeostasis that, *in vivo*, balances the production of new cells and the removal of senescent erythrocytes. Thus, a detailed characterization at the cellular level of the progression of the ageing phenomenon can reveal biological, biophysical and biochemical fingerprints for diseases related to misbalances of the cell turnover and for blood pathologies.

Many different techniques [1] have been used to investigate the modifications in the cell's dimension and shape and in the composition and oxidation state of the plasma membrane during ageing. In this work, we combined AFM imaging and Raman spectroscopy to analyse human RBCs. While high-resolution imaging characterized the morphological and mechanical effects of ageing, Raman spectroscopy provided a survey of the vibrational levels, to obtain characteristic mean spectra of single cells at different ageing times. Furthermore, by performing a statistical elaboration of the spectroscopy data through Principal Components Analysis (PCA), we highlighted subtle spectral differences associated with conformational and biochemical alterations induced by the progression of the ageing.

The collected data show a clear separation of the cellular spectra measured at different ageing times, opening the way to the efficient use of this technique for rapid, automatic and label-free assessment of cell status and evolution.

[1] "Structural, morphological and nanomechanical characterization of intermediate states in the aging of erythrocytes" M. Girasole, S. Dinarelli, G. Boumis Journal of Molecular Recognition 25 (2012) 285-291.

Use of focused ion beam/scanning electron microscopy (FIB/SEM) to study senescent features of pluripotent stem cells

Fiorella Colasuonno[1], Maurizio Muzzi[1], Rossella Borghi[1,2], Alessia Niceforo[1,2], Claudia Compagnucci[2], Andrea Di Giulio[1] and Sandra Moreno[1]

[1]University Roma Tre, Department of Science, LIME, Rome 00146, Italy

[2]Children's Research Hospital Bambino Gesù, Department of Neuroscience, Unit of Neuromuscular and Neurodegenerative Diseases, Laboratory of Molecular Medicine IRCCS, Rome 00146, Italy

sandra.moreno@uniroma3.it

Keywords: FIB/SEM, induced pluripotent stem cells mitochondria, autophagy

Understanding structural and compositional details down to the nanoscale is paramount to any scientific purpose, ranging from materials science to biomedical research. Focused ion beam/scanning electron microscopy (FIB/SEM) is a recently developed technology used by research laboratories, nanotechnology centers, and companies worldwide. Dualbeam instrument combines one electron beam (SEM column) and one ion beam (FIB column), oriented at 52°, and focused on the same point of the sample, thus enabling the operator to selectively ablate in a nanometer scale a previously marked region of the sample by using a focused ion current from a gallium source. The milling process can be interrupted every few nanometers to take high-resolution images of cross sections by the SEM column. Despite the great potential and flexibility of this innovative approach, applications are so far mainly limited to particle analysis and material characterization, being only occasionally utilized to study biological samples.
Induced pluripotent stem cells (iPSCs) represent a most promising tool in biomedical research, in that they mimic embryonic stem cell features, while being obtained from adult tissues. Indeed, they display the ability to differentiate in virtually any cell type, while being capable to mitotically divide, self-renewing themselves. Owing to these pluripotency and self-renewal properties, human iPSCs constitute an unlimited source of patient-specific cell types that could be used for disease modeling, as well as for tailored cell-based therapies, particularly concerning regenerative medicine and drug screening [1]. Human iPSCs are promptly obtained from skin biopsies, by reprogramming fibroblasts, through a recently established *in vitro* procedure, involving non-integrating episomal technology. Though extensively characterized from a molecular/genetic point of view, ultrastructural studies dealing with iPSCs peculiar features are still few, encouraging further research addressing this issue. Even scarcer information is presently available on the possible ultrastructural changes occurring in iPSCs, as a function of culturing time. In fact, despite general assumption that iPSCs can be maintained and propagated indefinitely in culture, alterations involving mitochondrial biogenesis and function have recently been found in long-term cultured iPSCs [2].
To investigate the issue of senescence processes occurring in iPSCs, we comparatively analysed ultrastructural features of iPSCs maintained in culture for 1, 6 and 12 month, focusing on mitochondrial morphology and intracellular distribution.
Human iPSCs derived by healthy male adult fibroblasts were cultured on Matrigel (BD Biosciences) in mTeSR1 (Stemcell Technologies) and passaged for varying time. They were transferred to Chamber Slide™ (Lab-Tek®), fixed in 0.2% glutaraldehyde and 2% paraformaldehyde in 0.1M cacodylate buffer and embedded in epoxy resin, prior to being analysed by a FIB/SEM Helios Nanolab (FEI Company, Eindhoven, The Netherlands). Resin-embedded iPSCs were mounted on stubs by using a self-adhesive carbon disk and gold sputtered by an Emithech K550. Regions of interest were cross-sectioned by the focused gallium ion beam operated at 30 kV and 6.5 nA. Pictures of each cross-section were acquired at a working distance of 2 mm using backscattered electrons (BSE) and a through-the-lens (TDL) detector in immersion mode with an operating voltage of 2 kV and an applied current of 0.17 nA (Fig. 1).
FIB/SEM micrographs from 1-month-cultured iPSCs show few mitochondria displaying spherical, immature-like shape, poorly developed cristae and mostly perinuclear localization. At difference, 6- and 12-month-cultured iPSCs display structurally mature mitochondria, widely distributed in the cytoplasm (Fig.2). These organelles show an elongated tubular morphology, numerous distinct cristae, reminiscent of a differentiated phenotype. Moreover, in mid-to-long-term cultured iPSCs, double-membrane limited vacuoles containing mitochondria and other cytoplasmic material, referred to as, autophagosomes are readily recognized (Fig. 2). These structures representing an index of ongoing senescence processes further support the previously hypothesized concept that long-term maintenance of iPSCs in culture may alter mitochondrial status [2]. In view of the crucial role played by mitochondria in the maintenance of pluripotency, differentiation, and reprogramming of iPSCs we suggest that these important properties may be progressively lost during culturing time, with relevant impact on their potential use for cell therapy. Indeed, culturing time-dependent features of iPSCs suggest their use as a faithful model of cell senescence and possibly of age-dependent human diseases.

[1] JJ. Unternaehrer and GQ. Daley, Philos Trans R Soc Lond B Biol Sci 366 (2011) 2274-85.
[2] A. Masotti et al., Aging 6 (2014) 1094-108.

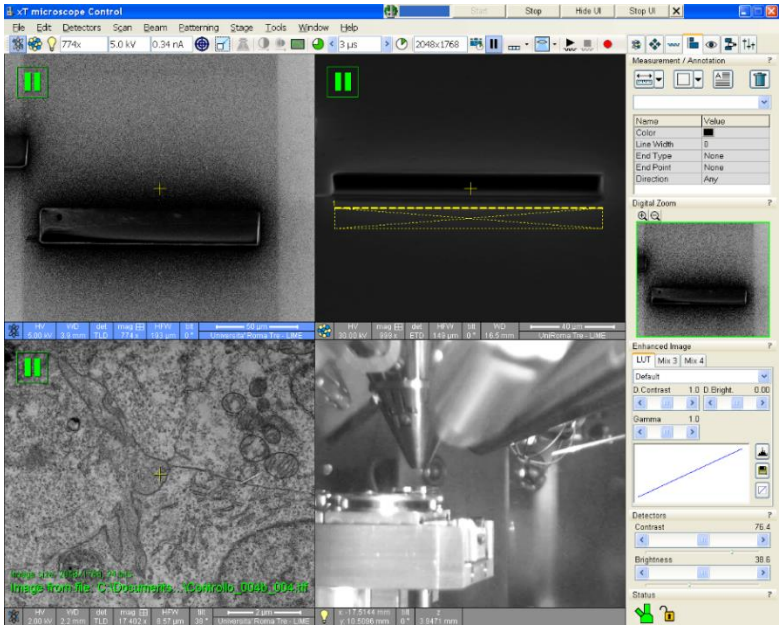

Figure 1. User interface showing SEM image with secondary electrons (top left quad); FIB image (top right quad); SEM image with backscattered electrons (bottom left quad); infrared CCD camera image (bottom right quad).

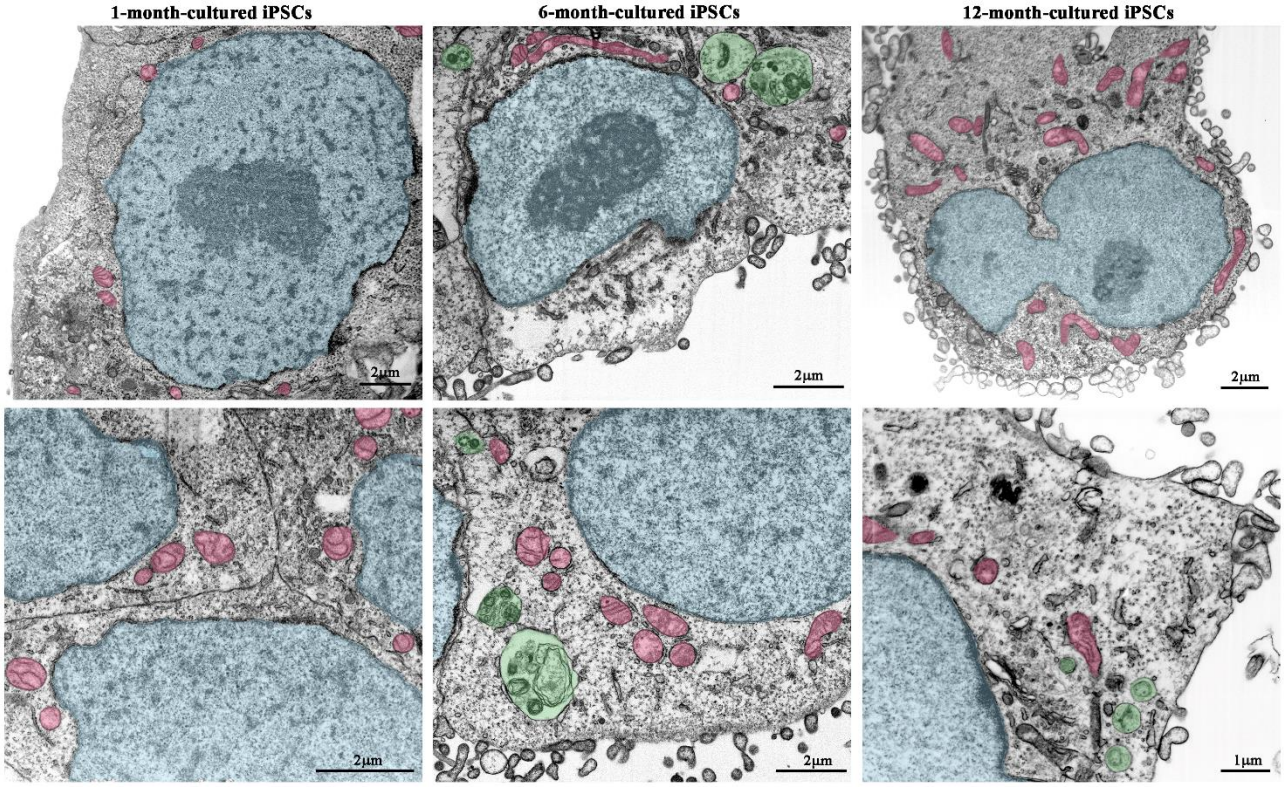

Figure 2. FIB/SEM micrographs from 1-, 6-, 12-month-cultured iPSCs. Light blue, nuclei; pink, mitochondria; green, autophagosomes.

Measurement results and improvements on an open EPR system

G. Sacco[3,4], C. De Angelis[1,4], G. De Angelis[1], S. Della Monaca[1,4], L. Di Trocchio[5], P. Fattibene[1], L. Ficcadenti[4], M. Lucentini[1,4], A. Mostacci[2,4], L. Piersanti[4], S. Pisa[3], E. Pittella[3], M. C. Quattrini[1,4], F. Santavenere[1,4]

1 Istituto Superiore di Sanità, Roma, 00161, Italy
2 Università "La Sapienza", Dip. Scienze di base e applicate per ingegneria, Roma, 00161, Italy
3 Università "La Sapienza", Dip. Ing. dell'inf., elettronica e telecomunicazioni, Roma, 00184, Italy
4 Istituto Nazionale di Fisica Nucleare, Sezione Roma 1, Roma, 00161, Italy
5 Univ. Bordeaux, IMS, CNRS UMR 5218, F-33405 Talence, France

e-mail: stefano.pisa@uniroma1.it

Keywords: (EPR, open resonator, modulation coil)

Electron paramagnetic resonance (EPR) is a spectroscopic method that allows measuring paramagnetic species, like stable radicals. EPR analysis has been proposed as a potential tool for non-invasive melanoma diagnosis [1]. Moreover, the EPR measurements can help to estimate the dose absorbed by people exposed during a nuclear disaster, detecting the number of radicals induced in their mobile phones due to the exposition. Using conventional closed microwave cavities, for the melanoma diagnosis the nevi must be extracted by biopsy in order to be examined and the phone display must be fragmented to be introduced inside the resonator. The aim of this work is to develop a system, compatible with the spectrometer Bruker Elexys E500, able to preserve sample integrity, i.e. allowing in principle to avoid the biopsy for a non-invasive melanoma diagnosis and the fragmentation of the display. The system uses an X-band resonant metallic cavity with a slit, realized on one side, for the leak of the excitation magnetic field and a Helmotz coil pair. The resonator allows measuring a sample lodged outside the cavity, while the coil produce a 100 kHz modulated field that encodes the output signal at a particular frequency and increases the SNR.

The design of the cavity has been performed using the software Microwave Studio (CST). Fig. 1 shows the final structure. The resonator was designed in order to reach a high-unloaded quality factor, Q_u, and to work with modes such that along the cavity sidewall, the magnetic and the electric fields have their maximum and minimum value, respectively [2].

The coils, instead, were designed to obtain a field enough uniform and strong in the sample volume. They are realized connecting in series on the same axis two solenoids, at a distance d = 7 cm, carrying the current in the same direction. Each coil has a radius R = 5.2 cm and consists of 100 turns of a copper wire with a radius of 250 μm (Fig. 2).

The efficacy of the system was tested by using, as sample material, a powder of stable free-radical molecules (DPPH), positioned on an adhesive support in contact with the slit. Fig. 3 shows the recorded signal. In order to increase the system performances, the matching of the coil has been improved. To this purpose, first, the coil impedance has been measured, with an LCR meter, as a function of the frequency. Then a circuital model that fits the impedance data around the central frequency of 100 kHz has been realized (Fig. 4). The resistance R is the static ones of the coils while the L inductance is that measured at 100 kHz. The R_1 resistance in the second branch takes into account the parasitic effects of the structure. Both measurements and the model evidence at 100 kHz an impedance modulus of about 2.5 kΩ that strongly reduces the coil flowing current and the generated magnetic field. A possible way for solving that problem is to put an adequate value capacitance, in series to the circuit of Fig. 4, in order to cancel the inductive term at the frequency of 100 kHz and consequently to reduce the impedance modulus. Simulations of the proposed structure, performed using the software AWR, allowed finding an optimal value of capacitance of about 630 pF. In this manner, the estimated current reaches about 110 mA at 100 kHz and is able to produce a magnetic field of about 1.5 G at the coil axis center.

[1] E. Cesareo et al., PLoS ONE 7(11)
[2] L. Di Trocchio, 18th Int. Conf. on Solid State Dosimetry, July 2016, Germany.

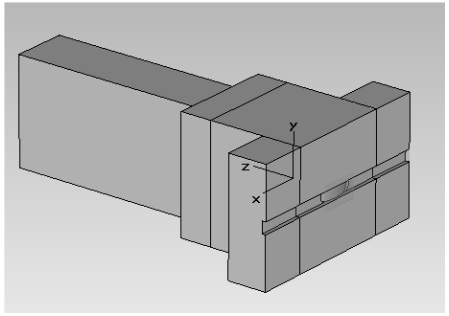

Figure 1. Sketch of the cavity designed with CST.

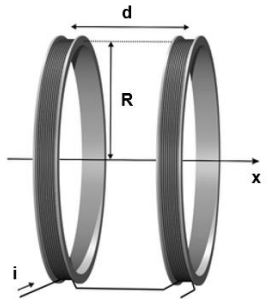

Figure 2. Coil system for the generation of the 100 kHz modulation field.

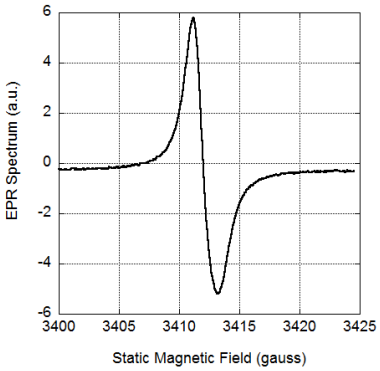

Figure 3. Output signal of the EPR for the DPPH sample placed in contact with the resonator slit.

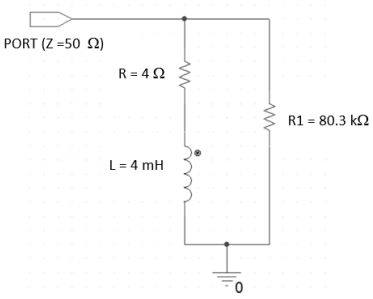

Figure 4. Circuital model of the coil system around the 100 kHz frequency.

Biocompatible flexible piezoceramic thin films for biomedical applications

N. D. Scarisoreanu [a], F. Craciun [b], V. Ion [a], R. Birjega [a], A. Bercea [a], V. Dinca [a], M. Dinescu [a], L. E. Sima [c], M. Icrivezi [c], A. Roseanu [c], L. Gruionu [d, e], G. Gruionu [d, f]

[a] National Institute for Laser, Plasma and Radiation Physics, Magurele, 077125, Romania
[b] CNR-ISC, Istituto dei Sistemi Complessi, Area della Ricerca di Roma-Tor Vergata, Roma, 00133, Italy
[c] Institute of Biochemistry of the Romanian Academy, Bucharest, 060031, Romania
[d] Medinsys Craiova, Craiova, 200409, Romania.
[e] Faculty of Mechanics, University of Craiova, Craiova, 200585, Romania
[f] Departament of Surgery, Harvard Medical School and Massachusetts General Hospital, MA 02114, USA
e-mail: floriana.craciun@isc.cnr.it

Keywords : biocompatible materials, piezoceramic thin films, laser processing, osteogenic differentiation, mesenchymal stem cells

In the last years there was an increased interest in developing piezoceramic materials for bone repair. Indeed several research studies evidenced that osteogenic regeneration and implant osseointegration could be actively improved by transforming electrical stimuli into mechanical loading necessary for cell signaling through mechanotransduction [1,2]. This process could help to overcome the so-called stress shielding, which occurs around implants and contribute to bone tissue loss and implant loosening [2]. In order to employ the piezoceramic materials in suitable devices for bone repair, it must first be tested if mesenchymal progenitors would be able to respond to these piezoceramics without being exposed to increased toxicity. In this study we report the synthesis of functional biocompatible piezoceramic $(Ba,Ca)(Zr,Ti)O_3$ (BCZT) thin films with enhanced piezoelectric properties. The high piezoelectric coefficients and dielectric constants, which make this material very appealing for a variety of applications in photonic, piezoelectric and electronic devices, are not the only advantages of BCZT system. Another significant perspective, given by the specific properties of BCZT as lead-free non-toxic material, regards its applicability in biology and medicine field, from fundamental biological studies to tissue engineering. We have first studied this $BaTiO_3$-based material suitably doped with Ca and Zr in order to optimize its composition in the phase diagram region where maximization of physical properties of interest can be obtained [3]. BCZT thin films have been grown from these targets and investigated by different techniques [4]. We have employed two pulsed laser-based techniques: classical pulsed laser deposition (PLD) and matrix-assisted pulsed laser evaporation (MAPLE). The MAPLE technique was specially developed for integration with polymeric/organic/biological materials and allows both the deposition of organic/polymer materials that would be damaged in a classical PLD process, as well as deposition on flexible polymer substrates, which is of high interest for integration of piezoactive thin films in flexible microdevices. PLD films have been grown on Pt/Si substrates while MAPLE films have been deposited on flexible polymer Kapton substrates coated with Pt. BCZT thin films grown by both techniques show similar structural properties and high piezoelectric coefficients [5]. The assessment of cell adhesion and osteogenic differentiation onto BCZT materials has been further investigated. It has been proved for the first time that BCZT films on Kapton polymer substrates provide optimal support for osteogenic differentiation of mesenchymal stem cells in the bone marrow. Laser-based approaches to obtain BCZT as biomaterials which support cellular adhesion, proliferation and differentiation can have an important impact to their exploitation in a variety of biomedical applications. Thus, by modulating the properties of BCZT thin films, the response of mammalian cells *in vitro* (adhesion, proliferation, migration, electrical stimulation and differentiation) can be adapted to the envisaged application. Therefore the results presented here can be of more general relevance for other biocompatible piezoactive materials and their applications in the biotechnology field.

[1] J. R. Fernandez et al, J. Theor. Biol. (2012) 292, 86-92.
[2] A. Olsson, Piezoelectric Coatings on Implants. Diploma work, Linköping 2005.
[3] F. Cordero et al., Appl. Phys. Lett. (2014) 105, 232904-232904-4.
[4] N. D. Scarisoreanu et al, ACS Appl. Mater. Interfaces (2015) 7, 23984-23992.
[5] N. D. Scarisoreanu et al, ACS Appl. Mater. Interfaces (2017) 9, 266-278.

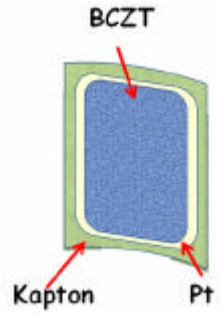

Figure 1. Sketch of a BCZT/Pt/Kapton structure.

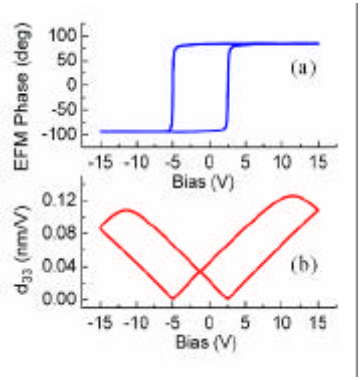

Figure 2. Piezoelectric response (phase and amplitude) of BCZT/Pt/Kapton.

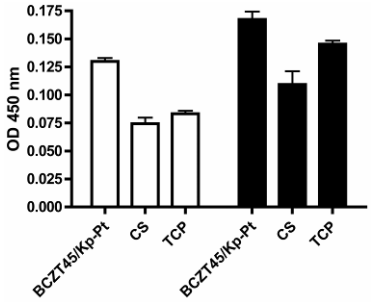

Figure 3. Proliferation rate by metabolic activity measurement of human epithelial embryonic kidney HEK 293 T (white) and human malignant melanoma A375 cells (black) grown for 48 h on BCZT/Pt/Kapton film, glass CS and TCP.

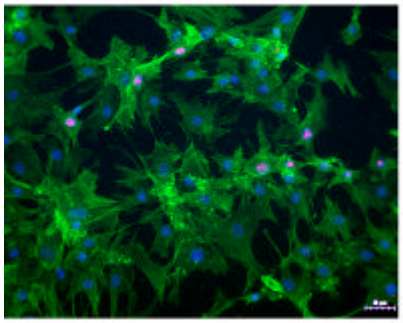

Figure 4. Spreading and proliferation of cells on BCZT/Pt/Kapton at 14 days postosteoinduction in osteogenic conditions.

Human Sperm Interactome network

Ordinelli A [a] Bernabò N [a] Orsini M.[b] Mattioli M [a,b] Barboni B [a]
[a] Faculty of Bioscience and Technology for Food, Agriculture and Environment, University of Teramo, Teramo, 64100, Italy
[b] Istituto Zooprofilattico Sperimenatle "G. Caporale", Teramo, 64100, Italy
e-mail: aordinelli@unite.it

Keywords: Human spermatozoa, biological network, male infertility, systems biology

From a biological point of view, it is known that mammalian spermatozoa after ejaculation are unable to fertilize the oocyte. They need, to acquire the ability of fertilizing, to reside from hours to days within the female genital tract. Here, they interact with different molecules before to recognize and bind the oocyte. It is possible to define the Sperm–Egg Recognition and Binding as a multistep multi-molecular event, which involves not only the gametes but, virtually, all the female genital tract[1]. This strengthens the importance of an integrated approach in the study of reproductive medicine, with major references to male infertility. Often, the most common diagnostic and therapeutic approaches are not effective in treating infertility. The personalized medicine could address these challenges, by characterizing individuals' phenotypes and genotypes. Integration of biological knowledge and the personalized medicine are the prerequisite to realize a model able to represent the molecular interaction that characterize sperm physiology. We realized the Human Sperm Interactome Network 3.0 (HSIN3.0) starting from the pathway active in male germ cells.
The HSIN3.0 Interactome was built by a multistep approach. As first, we collected data from papers indexed in PubMed referred to Human Sperm Proteome or proteomic studies of sperm biology. Then, staring from the list of identified proteins, we carried out a network enrichment and pathways reconstruction analysis through Reactome FI; Pathway Commons and String. Quality control and network creation was performed by some ad-hoc implemented Python scripts. Finally, with Cytoscape 3.4.0 was used to realize the network[2]. All the analysis have been carried out with the plug-in Network Analyzer (http://apps.cytoscape.org/apps/networkanalyzer).
The HSIN3.0 is constituted by 7891 nodes linked by 14712 links, and 25 connected components. In particular, we identified a Main Connected Component (HSNI3.0_MC) that accounts for 7758 nodes and 14534 links. The analysis of HSNI3.0_MC showed that it is characterized by a scale free topology that follows the Barabasi-Albert (BA) model but with a tendency to develop hierarchical pattern. The number of links per node (the node degree) follows a power law, with a negative exponent ($y = a\ x^{-1.764}$, $R2 = 0.771$), and the clustering coefficient (cc), which is a measure of the network tendency to form clusters, is low ($cc = 0.140$). In addition, HSNI3.0_MC is characterized by an ultra-small world topology: the averaged of. neighbours, which represents the mean number of connection of each node, is 3.746 and the characteristic path length, which gives the expected distance between two connected nodes, is 7.413.
These specific features, scale-free and ultra-small world architecture, describe a network resistant to random attacks and that is designed to respond quickly and specifically to external inputs. In addition, it has been possible to identify the most connected nodes (the hubs) and bottlenecks nodes. These results allowed us to explore the control mechanisms that drives sperm biochemical machinery and to verify different levels of control. Finally, we found that several key-nodes representing molecules specifically involved in function that are usually considered as not present or not active in sperm cells, such as control of cell cycle, proteins synthesis, nuclear trafficking, and immune response.
These approach could be helpful to identify new perspectives in the study of sperm biology and to identify potential diagnostic markers concurring in explaining male "idiopathic infertility", which are, at the present, one of the most important causes of fertilization failure.

1. Bernabò et al OMICS. 2014, 18(12):740-53
2. Bernabò et al., BMC Syst Biol. 2010, 4:87.

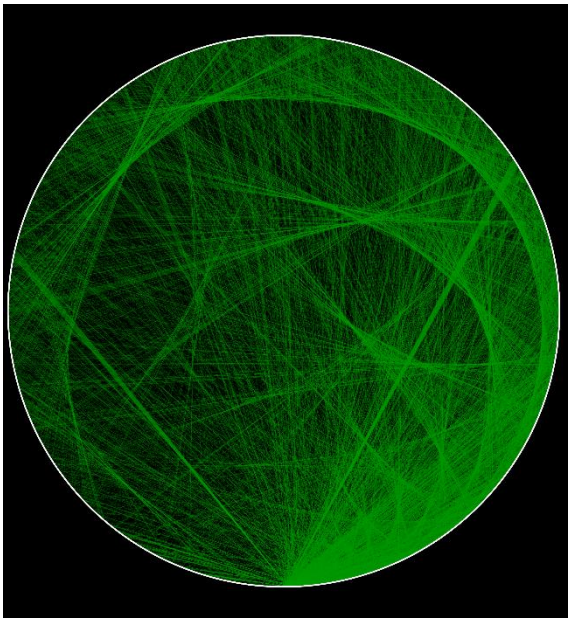

Figure 1. Network representing HSIN3.0 Interactome in spermatozoa

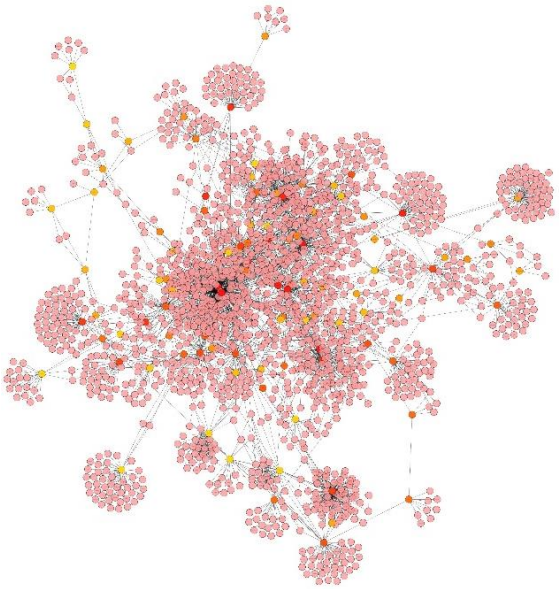

Figure 2. Network representing Bottleneck with the first-stage nodes

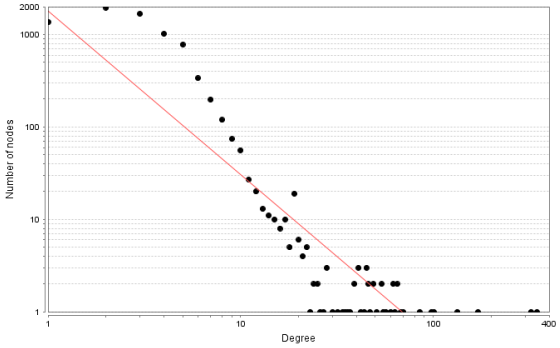

Figure 3. Node Degree Distribution

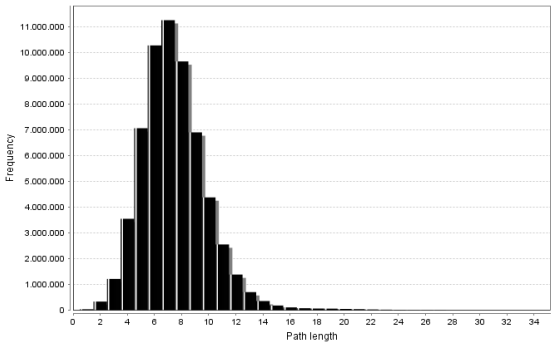

Figure 4. Shortest Path Length Distribution

Characterization of vibrational fingerprints along the Kok-Joliot's cycle by means QM/MM *ab-initio* molecular dynamics

Matteo Capone[1], Daniele Narzi[2], Leonardo Guidoni[1]

Institute 1, University of L'Aquila, Italy
Institute 2, Ècole Polytechnique Fèdèrale de Lausanne, Switzerland

e-mail: matteo.capone@graduate.univaq.it

Keywords: Photosystem II, Density functional theory, Kok-Joliot's cycle, QM/MM.

Unveiling the molecular details behind the water oxidation mechanism developed by the photosynthetic protein Photosystem II is a fundamental aim for theoretical and experimental studies.
The natural catalytic pathway consist in a five steps cycle named S0 to S4, for each step an electron and a proton is removed from the manganese based cluster present in the reaction center. On the step S4 the metal cluster reach the oxidizing potential capable of oxidize two water molecule to one of molecular oxygen.
Understanding the catalytic mechanism is crucial both for the characterization of the biological metabolisms and for the smart design of artificial biomimetic catalyst for the photo-activated water oxidation.
In the last years by mean of QM/MM, static and dynamic, simulations some important feature of the biological photo-oxidation was proposed. An oscillating mechanism for the crucial transition S2 to S3 has been proposed, the isomerization between and open and closed cubane fashion of the manganese cluster allows supplying of substrate water molecule and the advance in the catalytic pathway.
The vibrational infrared spectroscopy as well is a powerful and important tool to characterize the intermediate states of the Kok-Joliot's cycle, even though the complexity of the system led to notable problems in the interpretations of the spectra. The most studied spectral regions to understand the change of the reaction center along the key steps for the oxygen evolution are the manganese cluster regions at low frequencies (400-700 cm^{-1}) and it's ligands of first and second shell at mid frequencies (1100-1800 cm^{-1}), with a particular interest in the region associated with carboxylate ligands symmetrical stretching characterized by few superpositions (1200-1400 cm^{-1}).
Simulated infrared spectra from dynamical simulations provides useful insight to interpret the amount of experimental data present in literature that lack of a clear interpretation.
In our method the IR adsorption spectra is calculated as Fourier transform of the polarization time autocorrelation function, and applied on ~20ps long simulations of the S1, S2 and S3 states.
Furthermore the full spectra was divided in dipole components associated with the regions of major interest, in a similar framework of a previous work based on vibrational density of state.
Formalizing the dipole-dipole time autocorrelation in a correlation function, several interaction effect of the system was removed, leading to a clearer visualization of the single moiety contribute to the global infrared spectrum.
In the correlation framework the single component spectra is not anymore an IR spectrum but represent the algebraical decomposition of the total dipole spectrum. The approach provided assignations of all the symmetric stretching modes of the carboxylate groups, as well as for the anti-symmetrical modes, while for the manganese cluster only few modes has been assigned unequivocally, and further studies are required.

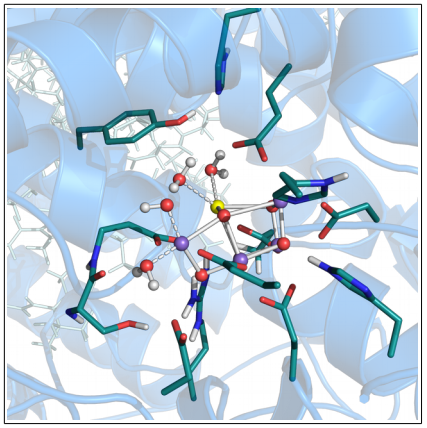

Fig.1: QMMM model of PSII, highlighted the atoms treated at DFT level.

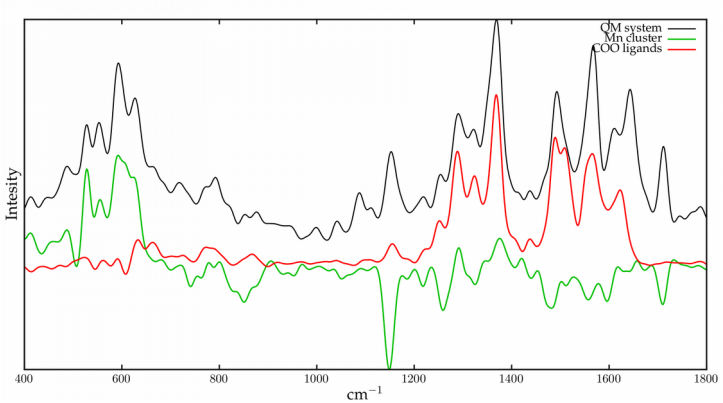

Fig.2: Total and decomposed infrared intensities of S2 state, in green and red the Mn cluster and carboxylate ligands decompositions.

Modeling Ru-based dendrimers: inorganic photosensitizers for artificial photosynthesis

Giovanna Rogati[1], Sebastiano Campagna[2], Leonardo Guidoni[1]

[1]University of L'Aquila, Dipartimento di Scienze Fisiche e Chimiche, L'Aquila 67100, Italy
[2] University of Messina, Dipartimento di Chimica, and Centro Interuniversitario per la Conversione Chimica dell'Energia Solare, Via Sperone 31, Messina 98166, Italy

e-mail: giovanna.rogati@roma1.infn.it

Keywords: Dendrimers, Photosensitizers, Artificial Photosynthesis, MD and DFT.

The natural photosynthesis, optimized through millennia of evolution, provides a highly efficient way to store and convert the solar radiation into chemical energy. Due to the increase in global energy demand, the search on artificial photosynthesis has been extremely appealing in the last decades. The solar-powered water oxidation can be exploited for hydrogen generation by direct photocatalytic water splitting.
To mimic the natural photosynthetic systems, a synthetic one, capable of performing artificial photosynthesis, should contain the following basic components: light-harvesting antennae, charge separation units and multielectron transfer catalysts.
Recently, it has been shown that decanuclear Ru(II) dendrimers, based on 2,3-bis(2′-pyridyl) pyrazine (dpp) bridging ligands (Fig. 1), can be ideal photosensitizers for photoinduced water oxidation. Indeed, they have three advantages: they absorb a good amount of visible light (their experimental absorption spectra show intense bands in the UV and in the visible region), they have a fast and efficient photoinduced electron transfer, and the oxidized sensitizer has a suitable potential [1].
The biggest challenge in the dendrimer modeling is that each monomer can exist as different geometrical isomers depending on the arrangement of the ligand around the metal ions and also on the spatial structure of the bridging ligand.
In the present work, we investigate the structure of decanuclear Ru-based dendrimer by quantum mechanics calculations and molecular dynamics simulations.
To identify the more stable isomeric structures of these complexes in the experimental conditions, we compared the relative stability of all stereoisomer mixtures. Molecular dynamics calculations reveal the details of the tridimensional structure of the dendrimer aggregates.

[1] F. Puntoniero, A. Sartore, M. Orlandi, G. La Ganga, S. Serronia, M. Bonchio, F. Scandola, and S. Campagna : Photoinduced water oxidation using dendrimeric Ru(II) complexes as photosensitizers, Coord. Chem. Rev, Vol 255, November 2011, doi:10.10167j.ccr.2011.01.026

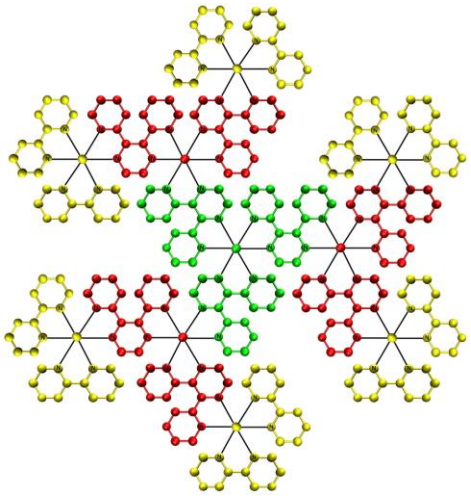

Figure 1: A decanuclear dendrimer (one central core, three intermediate cores, six peripheral cores, respectively the green one, the red ones and the yellow ones)

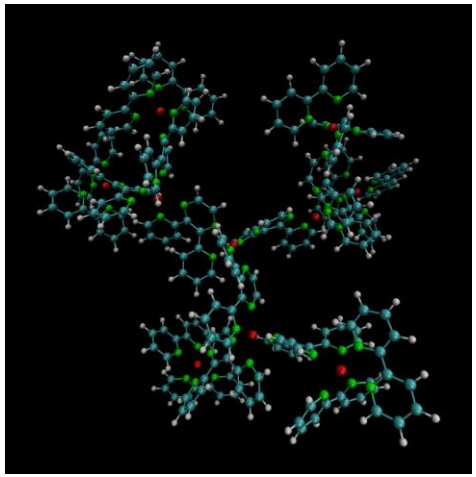

Figure 2: The optimized structure of decanuclear dendrimer containing only the most stable monomers

Characterization of the Sr 2+ - and Cd 2+ -Substituted Oxygen-Evolving Complex of Photosystem II by Quantum Mechanics/Molecular Mechanics Calculations

Fabio Pitari [a], Daniela Bovi [b], Daniele Narzi [c], Leonardo Guidoni [a]

[a] University of L'Aquila, L'Aquila, 67100, Italy
[b] Pangea Formazione S.r.l., Rome, 00145, Italy
[c] Ecole polytechnique fédérale del Lausanne, Lausanne, 1015, Switzerland
e-mail: leonardo.guidoni@univaq.it

Keywords: (photosynthesis, photosystem II, QM simulations, QM/MM simulations, Molecular Dynamics)

The Mn_4CaO_5 cluster in the oxygen-evolving complex is the catalytic core of the Photosystem II (PSII) enzyme, responsible for the water splitting reaction in oxygenic photosynthesis [1]. The role of the redox-inactive ion in the cluster has not yet been fully clarified, although several experimental data are available on Ca^{2+}-depleted and Ca^{2+}-substituted PSII complexes, indicating Sr^{2+}-substituted PSII as the only modification that preserves oxygen evolution [2]. Whereas the Sr^{2+} ion is experimentally known to restore the catalytic function of PSII in the calcium-depleted oxygen-evolving complex, albeit with a different turnover rate, Cd^{2+}-substituted PSII showed no activity, and in particular the catalytic cycle has been shown to stop between the S2 and S3 states [3]; this particular is very interesting since the existence of two distinct structural conformers of the Mn_4CaO_5 cluster representative of the S2 state of the Kok−Joliot cycle was proposed [4]. One of the two conformers is characterized by an open cubane (OC) structure (Figure 2) and an S=1/2 spin ground state, consistent with the EPR multiline signal. The other conformer has an S=5/2 ground state consistent with the EPR signal at g=4.1 and characterized by a closed cubane (CC) conformation (Figure 2). The two conformers were found to be interconvertible at physiological temperature, and the transition from the S2 state to the S3 state was suggested to proceed passing first by the OC state and afterward through the CC state [5]. On the basis of EPR measurements, Boussac et al. revealed that the g=4.1 signal, corresponding to the closed cubane configuration, is present also in Sr-substituted PSII. Conversely, in the Cd-substituted PSII complex, the typical double EPR signal associated with the S2 state was not found [6].

In this work, we investigated the structural and electronic properties of the PSII catalytic core with Ca^{2+} replaced with Sr^{2+} and Cd^{2+} in the S_2 state of the Kok−Joliot cycle by means of density functional theory and ab initio molecular dynamics based on a quantum mechanics/molecular mechanics approach. Our calculations do not reveal significant differences between the substituted and wild-type systems in terms of geometries, thermodynamics, and kinetics of two previously identified intermediate states along the S2 to S3 transition, namely, the open cubane and closed cubane conformers. Conversely, our calculations show different pKa values for the water molecule bound to the three investigated heterocations. Specifically, for Cd-substituted PSII, the pKa value is 5.3 units smaller than the respective value in wild type Ca-PSII. On the basis of our results, we conclude that, assuming all the cations sharing the same binding site, the induced difference in the acidity of the binding pocket might influence the hydrogen bonding network and the redox levels to prevent the further evolution of the cycle toward the S3 state.

[1] J. Barber, Chem. Soc. Rev. 38 (2009), 185−196.
[2] F. Koua et al.,Proc. Natl. Acad. Sci. U. S. A. 110 (2013), 3889−3894.
[3] C. Lee et al., Biochemistry 46 (2007), 3211−3223.
[4] D. Pantazis et al, Angew. Chem. Int. Ed. 51(2012), 9935−9940.
[5] D. Bovi, D. Narzi and L. Guidoni. Angew. Chem. Int. Ed. 52 (2013), 11744−11749.
[6] A. Boussac and A. W. Rutherford, Biochemistry 27 (1988), 3476−3483.

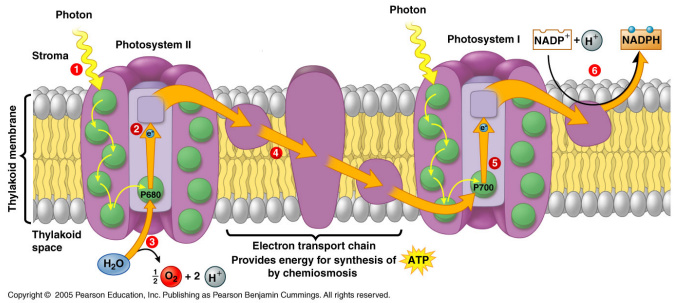

Figure 1. A sketch of the core systems involved in the photosynthesis. PSII is in charge to store photons from the sun using its chlorophylls; the associated energy allows the Oxygen Evolving Complex (OEC) to catalyze a water splitting reaction, then Photosystem I can store the energy using the remaining electron in the $NADP^+ + H^+ + 2e^- \rightarrow NADPH$ reaction.

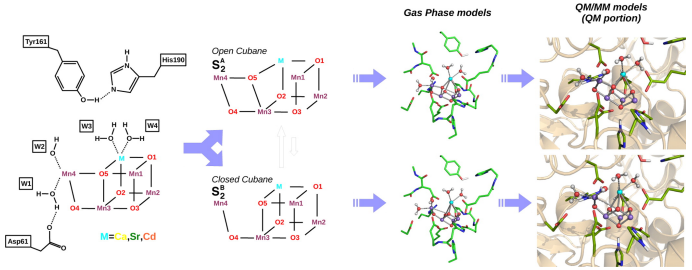

Figure 2. For every ion replacing Ca^{2+} in the OEC both the open and closed structure of the OEC in the S2 state of the Kok cycle have been simulated with DFT+U theory with both geometry optimizations and MD simulations. A preliminary study with a small QM model has been followed by QM/MM simulations.

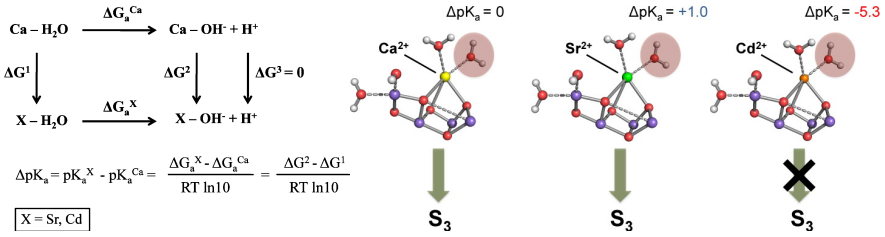

Figure 3: pKa differences for the system have been computed using a simple thermodynamic sycle in which every total energy has been computted by QM simulation of the relative system.

Current-voltage relation and electroosmotic flow in alpha-hemolysin nanopore via all-atom molecular dynamics simulations

Emma Letizia Bonome [a], Fabio Cecconi [b], Mauro Chinappi [c]

[a] Dipartimento di Ingegneria Meccanica e Aerospaziale Sapienza Università di Roma, Roma, 00185, Italy
[b] CNR-Istituto dei Sistemi Complessi UoS Sapienza, Roma, 00185, Italy
[c] Dipartimento di Ingegneria Industriale, Università di Roma Tor Vergata, Roma, 00133, Italy

e-mail: mauro.chinappi@gmail.com

Keywords: (nanopores, electroosmosis, molecular dynamics, electrohydrodynamics)

Nanopore analysis is a technique for biosensing at a single molecule level. In nanopore sensing a voltage is applied between the two sides of the membrane; in the presence of an electrolyte solution the ionic flow through the nanopore is inducted. When a molecule translocates across the nanopore a reduction of the current is measured. In the last decades several protocols on nanopores as sensors have been developed and many study are focused on the electroosmotic flow used as a tool to drive the ions in the pore [1,2], particle separation [3] and trapping [4].

In this work we present a computational study on the current-voltage relation and electroosmotic flow (EOF) in alpha-hemolysin (α-HL) nanopore at different ionic concentration of KCl, voltage and pH. The α-HL channel presents several residues exposed toward the interior of the pore that has a relevant effect on the ionic and electroosmotic flows. These residues are localized in three different region of the pore: in the cis and trans side and in the constriction, where a ring positive is presents. The change of these residues can be altered by varying the pH of the solution from 7.0 to 2.8 (fig 1B and 1C).

For this study we employed a computational protocol of non-equilibrium all atom molecular dynamics simulations with an external electric field applied normally to the membrane.

The fig. 1D shows the current-voltage characteristic at pH 7.0 (dashed line) and pH 2.8 (solid line). For low voltages the curve present a symmetry in agreement with the experimental results [5] but for high voltages the ionic current I at pH 7.0 is asymmetric respect to the voltage ΔV. The charges of these residues, in the three regions of the nanopore, a different pH and voltage, apply a repulsive and attractive action on the ions flow [3]. In particular at pH 7.0 the current intensity is larger at positive ΔV because the anions (Cl^-) and the cations (K^+) are both attracted in the pore. The results exhibit also that, for either the pH, the total current is dominated by the negative carries, in according with the anionic selectivity of the α-HL channel (fig. 1E).

The electroosmotic flow is very affected by the alteration of the pH. The flow is expressed in number of water molecules for unit of time (ns) and it is directed as the negative ions. The EOF flow is present at both pH values but it is favored at pH 2.8, as visible in fig. 1F, where the internal surface of the pore presents an excess of positive charges. The numerical results are compared with two continuum models for ideal electroosmotic flow. The first method estimates the ideal EOF flow for a cylinder of radius “a” and length L, with L » a. In the second model the EOF flow is achieved using a Poiseuille expression for a flow in a cylindrical channel. The result show that the value of the electroosmotic conductance is in according with the order of magnitude of the numerical results [6].

[1] Luo, Yun, and Benoît Roux. "Simulation of osmotic pressure in concentrated aqueous salt solutions." *The Journal of Physical Chemistry Letters* 1.1 (2009): 183-189.
[2] Bhattacharyya, S., and Subrata Bera. "Combined electroosmosis-pressure driven flow and mixing in a microchannel with surface heterogeneity." *Applied Mathematical Modelling* 39.15 (2015): 4337-4350.
[3] Malgaretti, Paolo, Ignacio Pagonabarraga, and J. Miguel Rubi. "Entropic Electrokinetics: Recirculation, Particle Separation, and Negative Mobility." *Physical review letters* 113.12 (2014): 128301.
[4] Asandei, Alina, et al. "Electroosmotic Trap Against the Electrophoretic Force Near a Protein Nanopore Reveals Peptide Dynamics During Capture and Translocation." *ACS applied materials & interfaces* 8.20 (2016): 13166-13179.
[5]Rodriguez-Larrea, David, and Hagan Bayley. "Multistep protein unfolding during nanopore translocation." *Nature nanotechnology* 8.4 (2013): 288-295.
[6]Emma Letizia Bonome, Fabio Cecconi, Mauro Chinappi "Electroosmotic flow through an Hemolysin nanopore" *Microfluidics and Nanofluidics* under review.

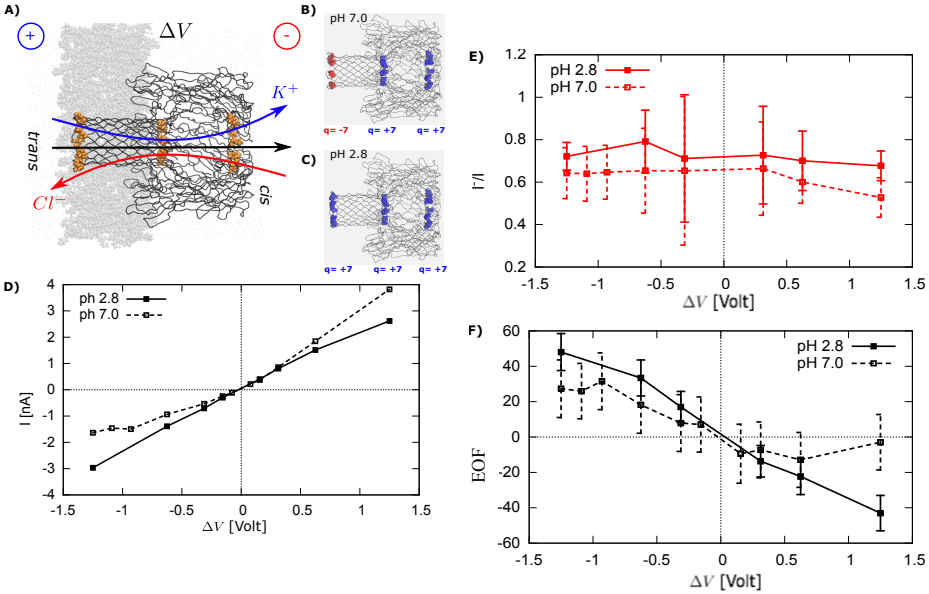

Fig. 1: A) System setup: schematic representation of nanopore of α-HL inserted in a lipid bilayer membrane. The arrows indicate the total current I and the cationic and anionic contributions. B, C) Total charge q for cis entrance, constriction and trans entrance at pH = 7 and pH = 2.8. Positive (negative) charged amino acids for these three regions are shown in blue (red). D) I-V curve for 2M KCl simulations at pH = 2.8 and pH = 7.0. E) Ion selectivity: anionic current fraction I-/I as a function of ΔV at pH = 2.8 and pH = 7.0 for 2M KCl. F) Electroosmotic flow (number of molecules for unit of time) as a function of ΔV.

.

Study of the hSAMHD1 self-assembly process by coarse grained molecular dynamics simulation approach

Francesca Cardamone*#, Mattia Falconi*, Siewert-Jan Marrink#, Alessandro Desideri*

*****Department of Biology, University of Rome "Tor Vergata", Italy*, francesca.cardamone@uniroma2.it

#*Molecular dynamics group, University of Groningen, Zernike campus, The Netherlands*

Keywords: Coarse grained molecular dynamics simulation (CG-MD), Self-assembly process, SAMHD1, MARTINI

Sterile alpha motif domain and histidine-aspartate domain-containing protein 1 (SAMHD1) plays a key role in the innate immunity blocking retrovirus infection, including HIV-1, in non-cycling cell types. The enzyme prevents the early steps of the reverse transcription, cleaving all four deoxynucleosides triphosphate (dNTPs) into their deoxynucleosides (dN) and inorganic triphosphate (PPP) [1]. In this way, the intracellular pool levels of dNTPs decrease under the threshold necessary to synthesize the cDNA by polymerase, arresting the viral replication [2]. Mutations in SAMHD1 are also associated with the rare disease Aicardi-Goutières syndrome (AGS), a severe neurological autoimmune condition which resembles a congenital viral infection [3].

SAMHD1 consists of 626 amino acids (72.2 kDa) organized in two major domains. The conserved SAM domain, implicated in still poorly known protein–protein and protein–RNA interactions, and the HD domain, necessary to achieve potent HIV-1 restriction (Fig. 1). The dNTPase activity is expressed by symmetric homo-tetrameric form of the enzyme and the assembly process is regulated by a complex allosteric mechanism, mediated by the collaboration of many cofactors such as GTP, dNTPs and metal ions (Fig 1). The equilibrium between the monomeric and dimeric form is modulated by GTP the cofactor [4] that also triggers the formation of a loose inactive, unstable and asymmetric tetramer [5]. The dNTP represents the substrate of the enzyme as well as the allosteric cofactor, permitting to reach the fully active symmetric tetrameric structure (Fig 1) [6]. Although it is clear which are the cofactors that initiate the enzymatic tetramerization process, it still remains unknown how SAMHD1 shifts from one equilibrium form to another one in a dynamic manner.

Biophysics and computational biology, two disciplines strictly related to each other, are powerful tools widely used to study the motion protein dynamics, conformational changes and assembly of macromolecules in solution. In this work, a coarse grained molecular dynamics (CG-MD) approach has been chosen to investigate the dynamical self-assembly process of SAMHD1 in a long-time simulation scale. The CG computational model of the four separated subunits of SAMHD1, in presence of GTP cofactor in the allosteric site and zinc ions in the catalytic site, has been created with MARTINI 2.0 force field [7] and it has been fixed in a simulation cubic box with water solvent. The CG beads, describing the chemical groups within each monomer, are constrained through elastic networks. The same procedure has been used to constrain the GTP inside each monomer. The model has been simulated for six microseconds on MARCONI HPC supercomputer (CINECA, Italy) with Gromacs 5.1.2 package. A snapshot of three different time states of the SAMHD1 assembly process during the simulation is reported and preliminary results are shown (Fig. 2). The simulation does not permit to reach the SAMHD1 crystallographic loose tetrameric structure (PDB ID code 4Q7H) [5], but an initial arrangement of the monomers can be seen. The four subunits take contact one with the other and the RMSD analysis shows that the four chains reach the convergence in a similar manner indicating the formation of a stable conformation (Fig. 3).

The results suggest that the coarse grained approach is able to build a realistic model of the SAMHD1 assembly process that can be used to prevent infections from large range of retroviruses.

[1] D.C. Goldstone et al., (2011) Nature 480:379-382.

[2] H. Lahouassa et al., (2012) Nat Immunol 13:223-228.

[3] G.I. Rice et al., (2009) Nat Genet 41:829-832.

[4] S.M. Amie et al., (2013) J Biol Chem 288:25001-25006.

[5] Y. Li et al., (2015) J Biol Chem 290:29428-29437.

[6] X. Ji et al., (2014) Proc Natl Acad Sci 111:E4305-E4314.

[7] S.J Marrink et al., (2007) J Phys Chem 111:7812-7824.

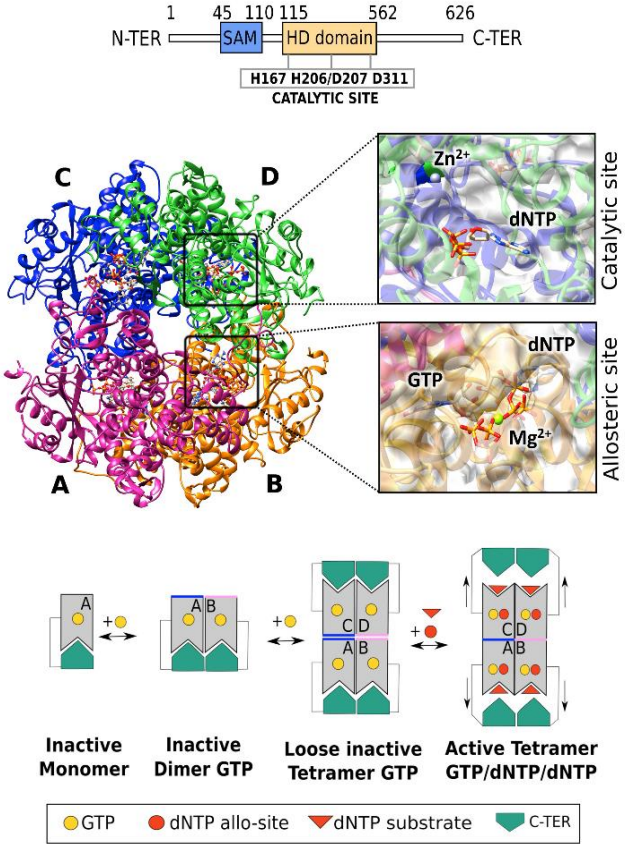

Figure 1. In the top, the SAMHD1 primary sequence with the two principal domains highlighting the catalytic residues of the enzyme. In the middle, a ribbon representation of SAMHD1 homo-tetrameric active structure. The catalytic and allosteric site are zoomed in square panels. At the bottom, a schematic representation of the monomer/tetramer equilibrium modulated by the binding of the substrate and cofactors, is reported as proposed by the crystallographic studies.

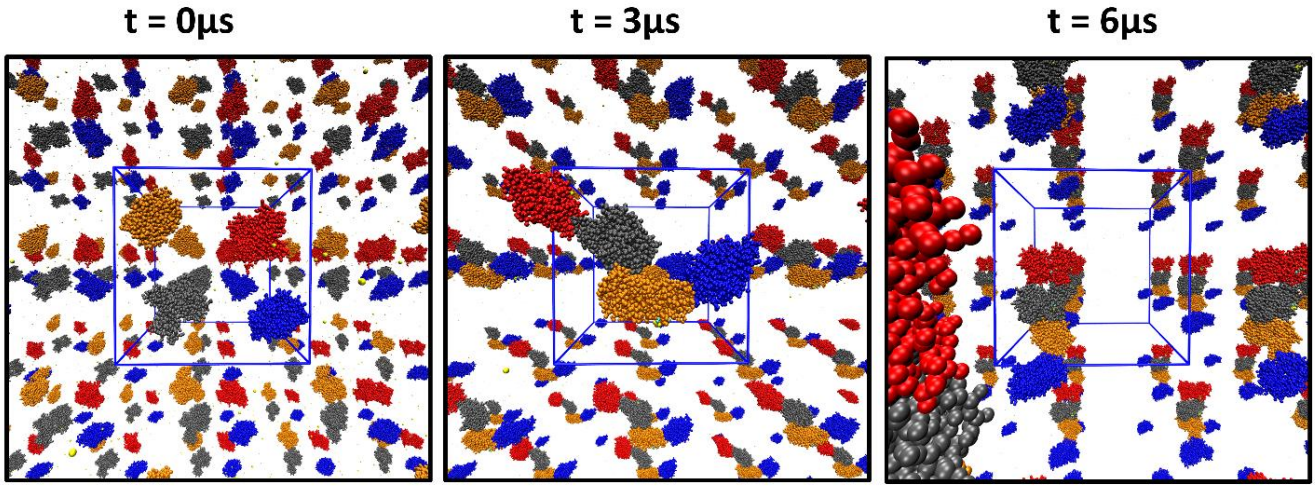

Figure 2. Three snapshots at different times during SAMHD1 CG simulation self-assembly process.

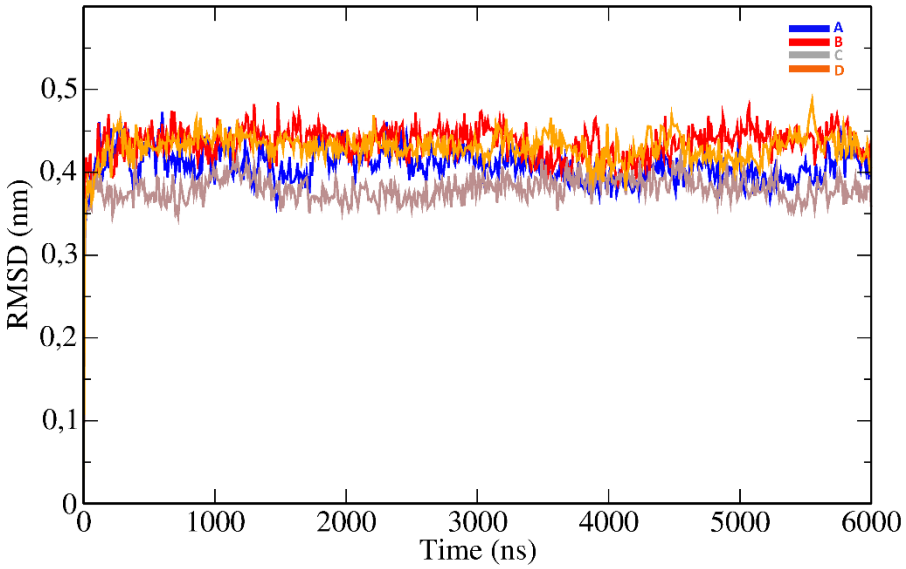

Figure 3. RMSD values during CG simulation time for each chains.

In silico structural and dynamic study of Laminin111

Giorgio Ripani[a], Gianfranco Bocchinfuso[a], Giovanni Marletta[b], Antonio Palleschi[a]

[a] Department of Chemical Sciences and Technologies, University of Rome Tor Vergata, Rome, Italy.
[b]Dipartimento di Scienze Chimiche. Università degli studi di Catania. Catania, Italy
e-mail: g.ripani93@gmail.com

Keywords: Laminin, ECM, Self-Assembly, Molecular Dynamics Simulations

Extra Cellular Matrix (ECM) has an important role in the development, function and homeostasis of the eukaryotic cells, by giving them physical support. Furthermore, ECM plays a role in the stability, separation and maintenance of different tissues and organs, by regulating levels of growing factors, hydration levels and pH of the local environment.
Laminin111 (L1) is a protein complex formed by three different chains (α1, β1, γ1), and it is one of the main components of the ECM. L1 interacts with Collagen, Integrin and other Laminin complexes by forming a sheet surrounding the cell wall. L1 is composed by roughly 6500 amino acids with a molecular weight of 800 kDa and it is composed by 54 different domains and a Coiled-Coil motif comprising roughly 1500 residues [1]. A structure of the whole complex is missing. In this Poster, we present, for the first time, the tridimensional structure of L1 and several dynamic aspects of the main functional regions will be discussed.
To obtain the structure of the whole protein we have used a hierarchical approach, by independently determining the structure of each single domain and then by connecting these structures to obtain the final model. Only for 13 of 54 domains experimental structural data were available. For the remaining ones the structures have been obtained by homology modeling followed by molecular dynamics simulations, when needed. The structure of the coiled coil motif has been obtained by matching the length of this tract observed in the AFM images [2]. The structure so obtained has been optimized by means of molecular dynamics (MD). The MD simulations have been carried out by using the GROMACS software package [3]. Fig. 1 reports the structure of the obtained model. The structures of the domains involved in the inter-proteins interactions are also reported, and the net charges of these domains are explicitly shown.
From a dynamical point of view, we have investigated the flexibility of a region composed by EGF-like domains. In particular, the domains numbered as 7, 8 and 9 in the chain γ1 have been analyzed by means of all-atoms(aa) and coarse-grained(cg) MD. Of note, these three domains are important for the binding with Nidogen. Fig. 2 reports the angle formed by EGF-like domains 7 and 8 during the CG simulation. These data show that a flexibility in the relative orientation of these domains is possible.
Finally, to investigate the mechanism of self-assembling of different laminin complexes, we have investigated the interaction between the cohesive N-terminal domains of the three different chains. To this end, we have performed MD simulations of a model of a trimeric complex obtained by using the CLUSPRO docking software [4]. Fig. 3 reports the structure of the ternary node of this region. This structure is coherent with the available experiments [5].

References
1) A K. Mouw et al. Nature Reviews Molecular Cell Biology 2014 15:771–785
2) C.H. Chen et al. Biochemistry 1998, 37, 8262-8267
3) B. Hess et al. J. Chem. Theory Comput. 2008, 4: 435-447
4)D. Kozakov et all. *Nature Protocols.* 2017 Feb;12(2):255-278
5)A. Purvis et. All.J. Biol. Chem. 2012 287, 53, pp. 44270 –44277

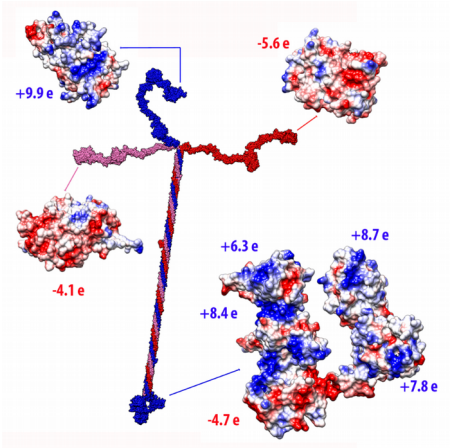

Figure 1: Complete structure of the murine laminin 111. The α1, β1 and γ1 chains are colored in blue, red and pink, respectively. The five G-like domains at the C-terminus of the α1 chain and the N-terminal domains of the α1, β1 and γ1chains are reported as solid surfaces colored for the electrostatic potential.

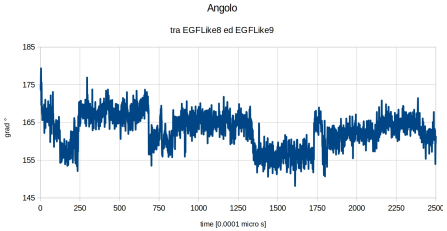

Figure 2: Value of the angle between the EGF-like8 and EGF-like9 domains measured respect the last and the first Cα during 2.5 μs of the molecular dynamics simulation.

.

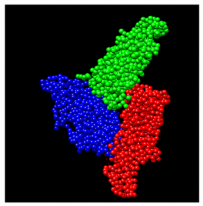

Figure 3: Most representative cluster of the simulation of the ternary node, showing the relative orientation of the cohesive N-terminal domains. The α1, β1 and γ1 chains are colored in green, red and blue.

Optimisation of a bioinformatic pipeline to study microbial communities trough 16S amplicons

Pietrucci D [a], De Marino A [a], Gruber CEM [b], Desideri A [a]

[a] Department of Biology, University of Rome Tor Vergata, Rome, 00133, Rome

[b] Laboratory of Virology, National Institute for Infectious Disease "L. Spallanzani", Rome, 00185, Italy

e-mail: daniele.pietrucci.89@gmail.com

Keywords: (metagenetics , pipeline , simulation)

The 16S rDNA gene encodes for a ribosomal RNA, which is a component of the small subunit (30S) of the prokaryotic ribosome. The 3D structure of this molecule is highly conserved, due to its essential structural role, therefore the sequence is characterized by a slow mutation rate, making it ideal for phylogenetic analysis. The study of prokaryotic composition of sample trough an high-throughput sequencing approach of the 16S rDNA gene is often referred has "metagenetics" [1] and it has been applied in different fields, moving from ecology [2] to medicine [3]. These analyses are tricky and are highly dependent on the computational methods used: different algorithms may lead to different results. The selection of the algorithm is important to reducing the False Positive Rate and increase the True Positive Rate. The choice of a well annotated reference database and threshold values for the algorithms represent key factors for an optimal assignment.

QIIME (Quantitative Insights Into Microbial Ecology) is one of the common pipeline used and it is based on the clustering approach. Sequences are clustered in Operational Taxonomic Unit (OTU) and the centroid of each cluster is assigned to a taxonomy trough the comparison with a reference database [4] . Here we propose an evaluation protocol of the combination of different algorithms and databases, used in two key steps of the QIIME pipeline, namely OTU clustering and taxonomic identification of the sequences using different databases. We evaluated the efficiency of different algorithms by the generation of an artificial dataset having a known taxonomy. Ribosomal sequences were downloaded from the manually curated database BioProject and an artificial set of Illumina reads was created using Grinder [5]. These sequences were used as input for the QIIME pipeline. Sequences were clustered using the usearch61 algorithm with a reference-free or a reference-based approach. The centroid of each cluster was assigned to a taxonomy using three different algorithms, each one based on a different strategy: RDP (Bayesian approach), UCLUST (fast global alignment approach) and BLAST (local alignment approach) [6-7-8]. Different threshold parameters were evaluated for each clustering and taxonomy assignement. We also tested the effect of the use of two different database, namely SILVA [9] and GreenGenes [10] that have been previously formatted and corrected using the NCBI taxonomy as a template. The taxonomic assignment coming from a total of 600 simulations was compared with the known taxonomy and two different metrics were used to assess the quality of the assignment. The clustering algorithms were evaluated using the Normalized Mutual Information (NMI). The assignment algorithms were evaluated using the F-measure, which is the harmonic mean of precision and recall values. The computation time was reported for each algorithm.

The NMI parameter shows that the clustering is independent of the selected database, when an higher percentage value is selected as threshold of sequence identity. The selection of the database has a great impact on the quality of taxonomic assignments and the selection of SILVA leads to better results. Among the three algorithm the Bayesian approach (RDP) results to be the best solution, showing a precision comparable to that of the alignment approach (BLAST, UCLUST) and the best recall value.

[1] S.H. Suenaga, Hikaru. Environmental microbiology 14.1 (2012): 13-22.

[2] M.L. Cuvelier et al. Proceedings of the National Academy of Sciences 107.33 (2010): 14679-14684.

[3] A.A. Althani et al., Journal of cellular physiology (2016).

[4] J.G. Caporaso et al., Nature Methods 7.5 (2010) 335-336

[5] F.E. Angly et al., Nucleic Acid Research. 40 (2012) gsk251

[6] J.R. Cole et al., Nucleic Acid Research. 37 suppl1 (2009) D141-D145

[7] R.C. Edgar, Bioinformatics 26.19 (2010) 2460-2461.

[8] S.F. Altschul et al., Journal of molecular biology 215.3 (1990) 403-410.

[9] E. Pruesse et al, Nucleic Acids Research 35.21 (2007) 7188-7196.

[10] T.Z. DeSantis et al., Applied and environmental microbiology 72.7 (2006) 5069-5072.

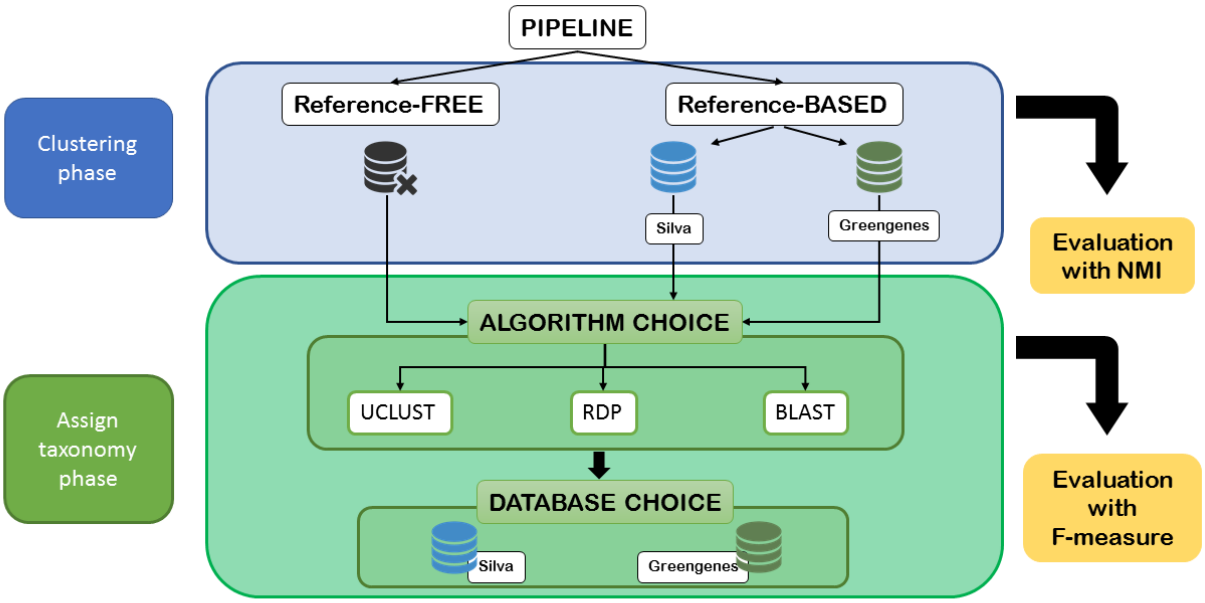

Image 1. Schematic rapresentation of the whole pipeline. The clustering phase was performed with a reference-free and a reference-based approach. In the latter case the SILVA and the Greengenes database were used to perform the clustering. The clustering was evaluated with the NMI parameter. The taxonomic assignment phase was performed with three different algorithm and with two databases. The taxonomic assignment were evaluated with the F-measure.

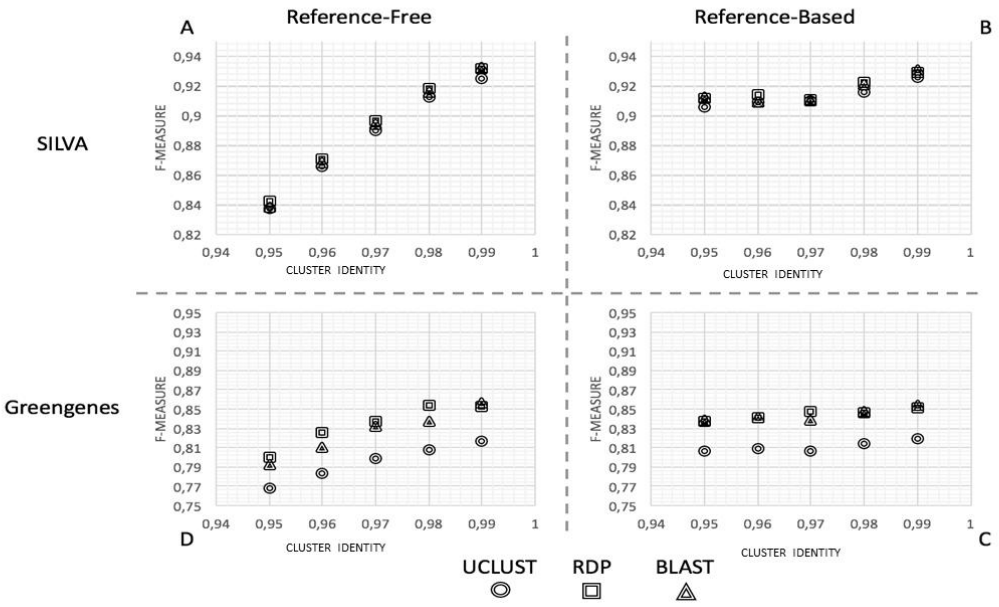

Image 2. F-measure parameter for taxonomic assignment with SILVA (first row) and Greengenes (second row) with a Reference-Free (first column) or a Reference-Based approach (second column). UCLUST, RDP and BLAST are marked with a circle, a square and a triangle respectively.

Essentiality, conservation and codon bias in bacterial genes.

Maddalena Dilucca[1], Giulio Cimini [2], Sergio Forcelloni [1] and Andrea Giansanti [1,3].
[1] Dipartimento di fisica, Università Sapienza, Rome, Italy
[2] Istituto di sistemi complessi (ISC-CNR) UoS Università Sapienza, Rome, Italy
[3] INFN Roma1 unit, Rome, Italy
e-mail: maddalena.dilucca@roma1.infn.it

Keywords: (essential genes, ERI, codon bias, bacteria).

Essential genes constitute the core of genes which cannot be mutated too much nor lost along the adaptive evolutionary history of a species. The natural selection is expected to be stricter on essential genes than on non essential ones. In order to shed light on this point, we study here how essentiality of a gene is connected with its degree of conservation among several unrelated bacterial species, each one characterised by its own codon bias. We show, confirming previous results on E.coli, that the essentiality of a bacterial gene, on average, exponentially increases as a function of its degree of conservation. Moreover, within each bacterium there are at least two groups of functionally distinct genes, with different levels of conservation and codon bias: an almost conserved core of highly selected, essential genes on the one side, and a set of less essential, less conserved and more mutable genes on the other, which are peculiar to the species. The core of essential genes is close to the minimal bacterial genome, which is in the focus of recent studies in synthetic biology. We also investigate the correlation between these parameters and codon bias, measured with statistical indices. We show that each bacteria has a different level of average codon bias index, that characterizes the patterns of codons usage for that species, as a "finger print". We also investigate the correlation between these parameters and codon bias, as measured with different indices. Each bacteria has a different level of average codon bias index, that characterizes the patterns of codons usage for that species. In particular, we find that conserved and more essential genes have, in general, an adapted codon usage. Finally, we analyze gene essentiality within functional clusters of orthologus groups (COGs), and find that the essential genes in bacteria are predominant in COG classes J (translation, ribosomal structure and biogenesis) and M (cell wall, membrane, envelope biogenesis). Nonessential genes instead mainly populate class E (amino acid metabolism and transport), P (inorganic ion transport and metabolism) and C (energy production and conversion). We can consider these parameters to make some considerations on the bacteria life and how the information from bacterial genome sequences can help in choosing of appropriate targets for searching new antibiotics.

[1] Peng C and Gao F Protein Localization Analysis of Essential Genes in Prokaryotes. Scientific Reports 4, Article number: 6001 (2014) doi:10.1038/srep06001.
[2] H,Gao F and Lin Y. Evolutionary conservation analysis between the essential and nonessential genes in bacterial genomes. Scientific Reports 5 (2015): 13210.
[3] S. Y. Gerdes, M. D. Scholle, J. W. Campbell, G. Balzsi, E. Ravasz, M. D. Daugherty, A. L. Somera, N. C. Kyrpides, I. Anderson, M. S. Gelfand, A. Bhattacharya, V. Kapatral, M. D'Souza, M. V.Baev, Y. Grechkin, F. Mseeh, M. Y. Fonstein, R. Overbeek, A-L. Barabsi, Z. N. Oltvai, and A. L.Osterman. Experimental determination and system level analysis of essential genes in Escherichia coli mg1655. J Bacteriol, 185(19):5673{5684, Oct 2003.
[4] Dilucca M, Cimini G, Semmoloni A, Deiana A, Giansanti A. Codon Bias Patterns of E. coli's Interacting Proteins PLoS ONE 10(11): e0142127. doi:10.1371/journal.pone.0142127.

.

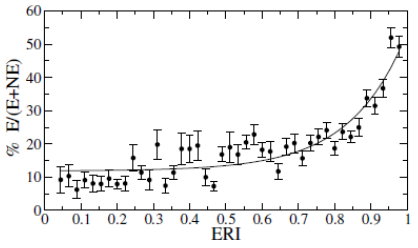

Figure 1. Correlation between essentiality and ERI.

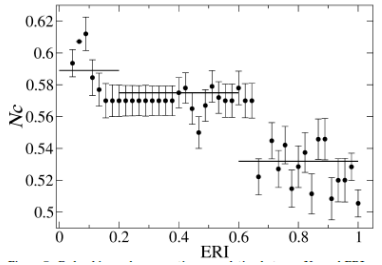

Figure 2. Codon bias and conservation:correlation between a codon bias index (Nc) and ERI.

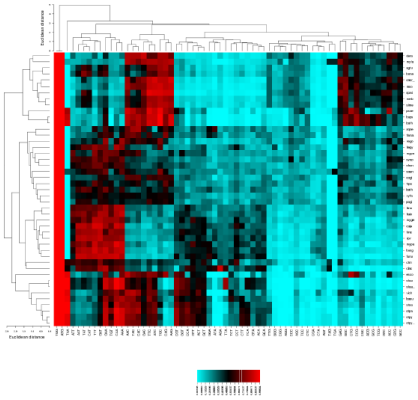

Figure 3. Heat map of RSCU vectors.

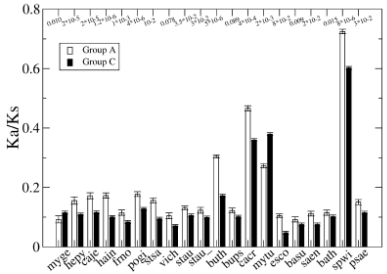

Figure 4. Histogram of Ka/Ks for specific and conserved genes in each bacteria.

New insight into the interaction of TRAF2 C-terminal domain with lipid rafts microdomains

Almerinda Di Venere[a,c], Eleonora Nicolai[a], Arianna Ceccarelli[a], Anastasia De Luca[a], Nicola Rosato[a,c], Enrico Gratton[b], Anna Maria Caccuri[a,c], Giampiero Mei[a,c]

[a]Department of Experimental Medicine and Surgery, University of Rome Tor Vergata, Via Montpellier 1, 00133 Rome, Italy

[b]Laboratory for Fluorescence Dynamics, Biomedical Engineering Department, University of California at Irvine, Irvine, CA, USA.

[c] Center NAST, Nanoscience, Nanotechnology, Innovative Instrumentation, University of Rome Tor Vergata, 00133 Rome, Italy

Email: mei@med.uniroma2.it

Keywords: fluorescence microscopy, general polarization, lipid rafts, protein – lipid interaction

In this study we provide the first evidence of the interaction of a truncated-TRAF2 with lipid rafts microdomains. We have analized this interaction by measuring the diffusion coefficient of the protein in large and giant unilamellar vesicles (LUVs and GUVs, respectively) obtained both from synthetic lipid mixtures and from natural extracts. Steady-state fluorescence measurements performed with synthetic vesicles indicate that this truncated form of TRAF2 displays a tighter binding to raft-like LUVs with respect to the control (POPC-containing LUVs), and that this process depends on the protein oligomeric state. Generalized Polarization measurements and Spectral Phasor Analysis revealed that truncated-TRAF2 affects the membrane fluidity, especially when vesicles are heated up at physiological temperature. The addition of nanomolar concentration of TRAF2 in GUVs also seems to exert a mechanical action, as demonstrated by the formation of intraluminal vesicles, a process in which ganglioside GM1 plays a crucial role.

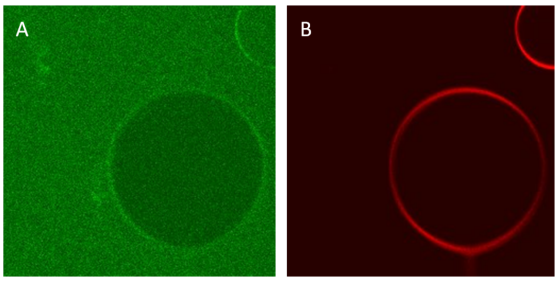

Figure 1– Panel a: binding of alexa-labeled TRAF2 to a POPC-GUV (diameter 20 μm); panel b: visualization of the GUV through the membrane marker CellMask Orange.

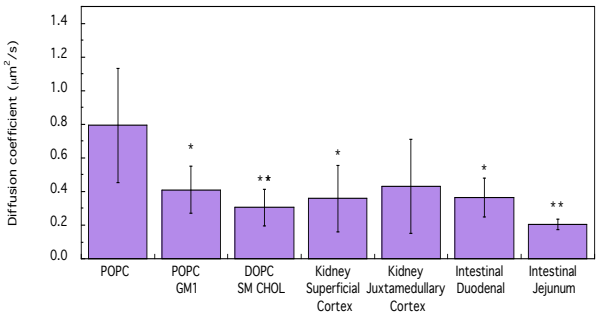

Figure 2 – Diffusion coefficients of labeled TRAF2 bound to GUVs. Vesicles were obtained from 1-palmitoyl-2-oleoyl-sn-glycero-3-phosphocholine (POPC), raft-like mixture (i.e. 1,2-dioleoyl-sn-glycero-3-phosphocholine/sphingomyelin/cholesterol (DOPC/SM/Cholesterol), BBM samples (Kidney Juxtamedullary Cortex (JMC), Kidney Superficial Cortex (SC), Intestinal Duodenum (ID), and Intestinal Jejunum (IJ)) and POPC + 1 % GM1. Data are expressed as mean ± SD values of three independent experiments; * and ** denote $p < 0.05$ and $p < 0.01$, respectively, versus TRAF2 bound to POPC - GUVs.

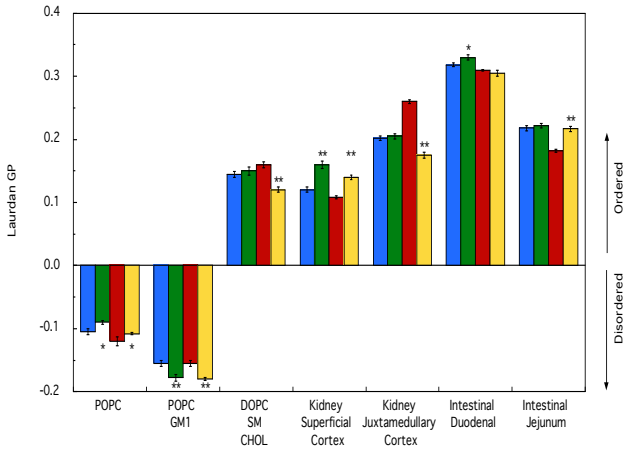

Figure 3 – Laurdan GP values calculated at room temperature (blue and green) and body temperature (red and yellow) for all samples, before (blue and red) and after the addition of non-labeled TRAF2 (green and yellow). Data are expressed as mean ± SD values calculated from at least 15 – 20 GUVs of two different preparations. * and ** denote $p < 0.05$ and $p < 0.01$, of green and yellow samples versus the blue and red ones, respectively.

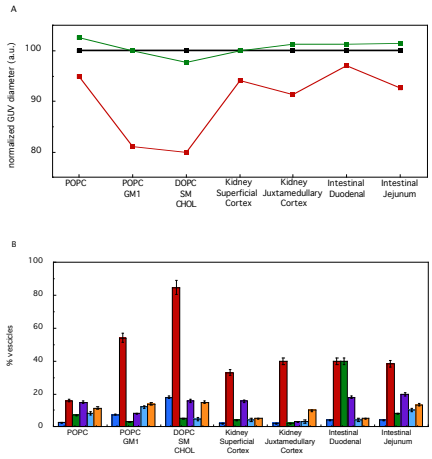

Figure 4 – Panel A: GUVs diameter changes observed after TRAF2 addition (red). Control experiments have been conducted adding KB (black horizontal line) and BSA (green). Points have been connected only to guide the eye. Panel B: Percentage of intraluminal vesicles occurring in GUVs in the absence of TRAF2 (blue, green, cyan), after TRAF2 addition (red) and in control experiments in which KB (purple) or BSA (orange) have been added.

Probing the dynamic fingerprint of insulin secretory granules in living cells by spatiotemporal fluctuation spectroscopy

Gianmarco Ferri [a], Luca Digiacomo [b], Lorenzo Scipioni [c], Marco Bugliani [d], Luca Lanzano [c], Piero Marchetti [d], Giulio Caracciolo [b], and Francesco Cardarelli [a]

[a]NEST - Scuola Normale Superiore, Istituto Nanoscienze - CNR (CNR-NANO), Pisa, Italy.
[b] Department of Molecular Medicine, "La Sapienza" University of Rome, Italy.
[c] Nanoscopy, Nanophysics Dept., Istituto Italiano di Tecnologia, Genoa, Italy.
[d] Dept. of Clinical and Experimental Medicine, University of Pisa, Italy

e-mail: francesco.cardarelli@nano.cnr.it

Keywords: fluorescence correlation spectroscopy, GFP, Insulin secretory granule, β-cell, Phogrin

Insulin secretory granules (ISGs) are cytoplasmic organelles (200–400 nm in linear size) containing a dense core consisting of insulin molecules arranged in crystalline-like arrays. They are naturally present in the β-cells of Langerhans islets within Pancreas and in several tumor-derived cell lines commonly used as models of β-cell biology. They exert the complex function of insulin secretion through tight regulation of key structural and functional properties, such as size, speed, mode of motion, number, etc. Quantitative description of these parameters in living matter is crucial for our understanding of insulin granule function in physiology and its alterations in pathology. Yet, despite the efforts, a systematic characterization of the dynamic behaviour of ISGs remains largely elusive. We addressed this hot topic by fluctuation microscopy, a strategy capable of adding a dynamic molecular dimension to standard fluorescence imaging of living matter. In particular, we started from a fluorescence-based spatiotemporal fluctuation analysis method that makes possible to probe the actual molecular "diffusion law" directly from imaging, in the form of a mean square displacement (MSD) versus time-delay plot (image-derived MSD, hereafter referred to as *i*MSD) [1,2] (Figure 1a-b), with no need to preliminarily assume any interpretative model. By fitting the *i*MSD curve (Figure 1c), relevant parameters describing the average dynamic behavior of ISGs can be extracted, such as short- and long-range diffusion coefficients, confinement strength (in case of confined diffusion), anomalous diffusion coefficient (α). Of note, a further relevant feature of the *i*MSD plot is that its y-axis intercept (obtained after subtraction of the PSF value) readily provides a quantitative estimate of the average size of the diffusing ISGs. From each analyzed *i*MSD, the aforementioned set of parameters is extracted and represented in a parametric space, in such a way that that each cell corresponds to one point in the plot. Thus, the clustering of single-cell points readily depicts what we define as the "dynamic fingerprint" of ISGs at the whole cell population level. As a first test, we used GFP-tagged Insulin and GFP-tagged Phogrin (a granule transmembrane phosphatase) transfected into insulinoma-1 (INS-1) cells, a recognized experimental model for the study of β-cell biology. Remarkably, as reported in Figure 2, the dynamic fingerprint of ISGs appear different depending on the GFP-tagged protein chosen for imaging. In particular, Insulin-EGFP transfected cells are characterized by lower average size and slower diffusion coefficient as compared to the Phogrin-EGFP transfected ones. This result highlights the hitherto neglected impact of labelling on granule structure/function. To further test the potency of ISG fingerprinting, we treated Insulin-EGFP transfected INS-1 cells with cholesterol-loaded Methyl-β-cyclodextrin (MβCD-Chol) to deliver exogenous cholesterol to cell membranes. In this case, we observed an expected shift of the fingerprint position towards an average larger size and faster average diffusivity (Figure 3). Finally, in order to study the dynamic fingerprint of ISGs in a mostly unperturbed intracellular environment, we dissociated human pancreatic islets and transfected the obtained isolated cells with Insulin-EGFP. In Figure 4 the comparison between INS-1 and Human β cells is reported: not surprisingly, the two fingerprints appear as distinct. Of note, a sensibly narrower range of size and diffusivity values are observed for Human β cell ISGs as compared to INS-1 ones. In our knowledge, this is the first time that the cytoplasmic dynamic behavior of ISGs in Human cells is described. In conclusion, this approach does not require the extraction of individual molecular trajectories nor the use of particularly bright fluorophores (e.g., GFP-tagged molecules transiently transfected into cells) and allows to describe the dynamic behavior of granules at a whole-cell level and rapidly highlight any possible alteration.

[1] C. Di Rienzo et al., PNAS (2013). 12307-12312.
[2] L. Digiacomo et al., Acta biomaterialia (2016). 189-198.

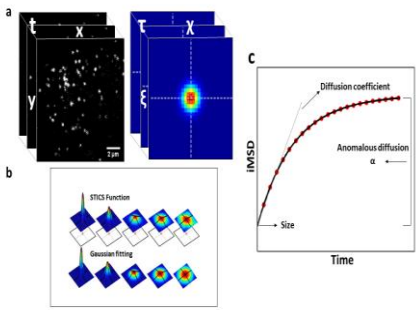

Figure 1. a) A stack of intensity image of labelled ISGs is analyzed by STICS algorithm to obtain the spatio-temporal correlation function. b) a 2D Gaussian fitting of STICS function is then performed to obtain the *i*MSD curve (c), from which dynamic relevant parameters and size of ISGs are obtained.

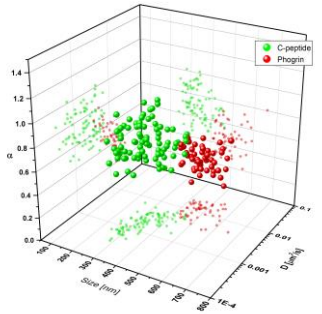

Figure 2. Two distinct dynamic fingerprints obtained by data clusterization of INS-1 E transfected with Insulin-GFP and Phogrin GFP.

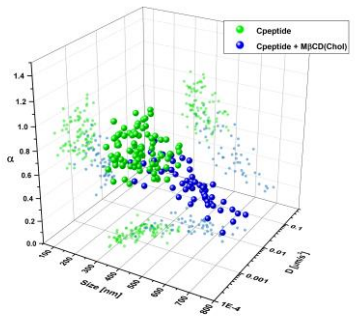

Figure 3. Cholesterol treatment induces an increasing of size and diffusivity of ISGs labelled with Insulin-GFP.

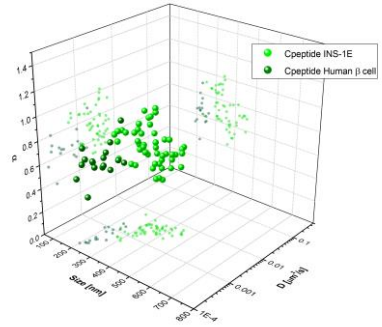

Figure 4. Insulin-EGFP labelled ISGs in INS-1 E and human β cell.

H-D exchange kinetics in β-lactoglobulin-(-)epicatechin complexes revealed by FTIR spectroscopy and PCA methods

Marina Carbonaro[a], Francesca Caporaletti[b], Paola Maselli[b], Alessandro Nucara[b]

[a]Council for Agricultural Research and Economics, Food and Nutrition Research Center, Rome, 00178, Italy
[b]Department of Physics, Sapienza University of Rome, Rome, 00185, Italy

e-mail: marina.carbonaro@crea.gov.it

Keywords: (epicatechin, β-lactoglobulin, deuteration, secondary structure, PCA)

Flavonoids are plant secondary metabolites with different chemical structures, responsible for multiple biological and pharmacological properties [1]. Besides to the antioxidant activity mainly ascribed to the phenolic moiety, flavonoids can bind to enzymes or proteins, either covalently or non-covalently. The binding changes structural and physico-chemical properties (solubility, thermal stability), lowers susceptibility to digestion in the gastrointestinal tract and modulates biological activities of either protein or polyphenol [2]. Among flavonoids, (-)epicatechin (EC) is a monomeric flavanol widely spread in the diet and present in red wine, tea, cocoa, apple, pea, cherries. Its health-promoting effects in humans include cardiovascular diseases, diabetes and cancer prevention. β-Lactoglobulin (BLG), a protein with high potential applications in the food and pharmaceutical fields, can bind several small molecules -vitamins, fatty acids, polyphenols (epicatechins included), into its large hydrophobic site, with specific conformational changes involving protein dissociation [3]. Notably, mechanism of hindrance to fibril formation by EC binding to BLG has recently been investigated [3]. In studying drug-protein interaction, FTIR spectroscopy is a powerful tool in the identification of structure-activity relationship by quantifying the modifications in secondary structure elements that underly biological or pathological effects, i.e. fibril formation in the development of neurodegenerative disorders (Alzheimer's and Parkinson's diseases) [4]. FTIR data of BLG-EC complexes have been reported, but information on protein conformation in the complexes are not conclusive [5]. In the present study, the kinetics of Hydrogen-Deuterium (HD) exchange in BLG and BLG-EC solutions was analyzed at a molecular level by the analysis of the amide I absorption band at 1650 cm^{-1}. The slight red-shifts and intensity changes in the amide-I components were revealed at different concentrations and at physiological pH by applying the Principal Components Analysis (PCA) methods. Three different kinetics for the HD exchange were identified in BLG and discussed in the framework of the Linderström-Lang model for multimers and stable aggregates. The constant rates measured were compared with those observed in the BLG-EC complexes. The overall data assign to EC an effectiveness to form stable high MW aggregates, a role that might be central in studies on food science. The present information about the mechanism of interaction between BLG and small phenolic compounds may help in clarifying the physiological role of the protein and in planning strategies for improving bioavailability of micronutrients and bioactive compounds through protein binding.

[1] C. Manach et al. Am. J. Clin. Nutr. 81 (2005) 230S-242S.
[2] M. Carbonaro et al. Eur. J. Nutr. 40 (2001) 84-90.
[3] A. Nucara et al. SpringerPlus 2 (2013) 661.
[4] M. Carbonaro et al. Biochim. Biophys. Acta 1864 (2016) 766-772.
[5] C. Kanakis et al. Food Chem. 127 (2011) 1046-1055.

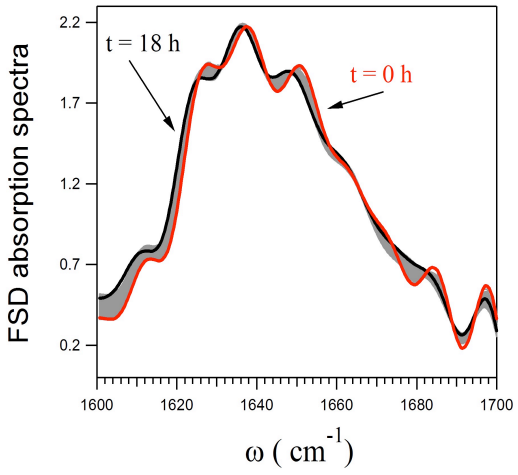

Figure 1. Amide I spectra of BLG at 1 mM in D_2O buffer as a function of the time. The first spectrum is reported in red, the the last one at t=18 h in black. Spectra acquired at intermediate times are shown in grey. FSD deconvolution has been performed using a bandwidth of 4 cm^{-1} and a resolution enhancement of 2.5.

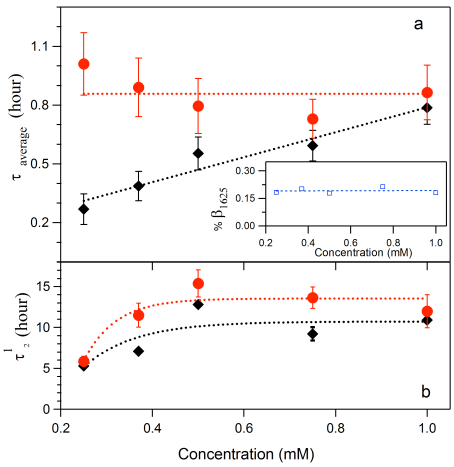

Figure 2. Average lifetimes of the HD exchange in BLG (black diamonds) and BLG-EC solutions (red dots), for the slow (panel b) and the fast HD kinetics (a) . In the inset of panel a the intensity of the β-sheet components at 1625 cm^{-1} is reported for the BLG samples.

Cell-Density Dependence of Host-Defense Peptide Activity and Selectivity in the Presence of Host Cells

Filippo Savini [a], Vincenzo Luca [b], Alessio Bocedi [a], Renato Massoud [c], Yoonkyung Park [d], Maria Luisa Mangoni [b], Lorenzo Stella[a]

[a] University of Rome Tor Vergata, Department of Chemical Sciences and Technologies, Rome, 00133, Italy.
[b] Sapienza Rome University, Department of Biochemical Sciences "A. Rossi Fanelli", Rome , 00185, Italy
[c] Department of Experimental Medicine and Surgery, University of Rome Tor Vergata, Rome , 00133, Italy
[d]Chosun University, Department of Biotechnology, 501-759 Gwangju, Korea

e-mail: stella@stc.uniroma2.it

Keywords: (host-defense peptides, selectivity, red blood cells, hemolysis, bacterial killing)

Host-defense peptides (HDPs) are promising compounds to fight multidrug-resistant microbes. In vitro, their bactericidal and toxic concentrations are significantly different, but this might be due to the use of separate assays, with different cell densities. For experiments with a single cell type, the cell-density dependence of the active concentration of the DNS-PMAP23 HDP could be predicted based on the water/cell-membrane partition equilibrium and exhibited a lower bound at low cell counts (fig 1). On the basis of these data, in the simultaneous presence of both bacteria and an excess of human cells, one would expect no significant toxicity, but also inhibition of the bactericidal activity due to peptide sequestration by host cells. However, this inhibition did not take place in assays with mixed cell populations (fig 2a), showing that for the HDP esculentin-1a(1−21)NH2, a range of bactericidal, nontoxic concentrations exists and confirming the effective selectivity of HDPs (fig 2b). Mixed-cell assays might be necessary to effectively asses HDP selectivity.

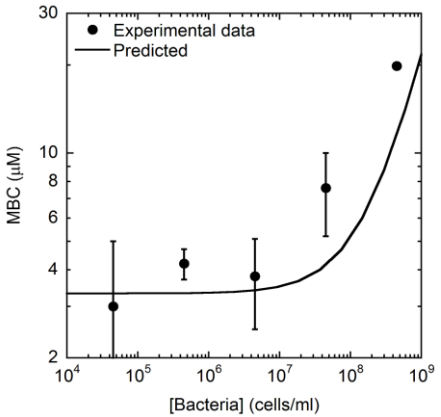

Figure 1. Predicted and experimental cell-density dependence of the MBC (defined as the concentration that causes the death of 99.9% of bacteria)

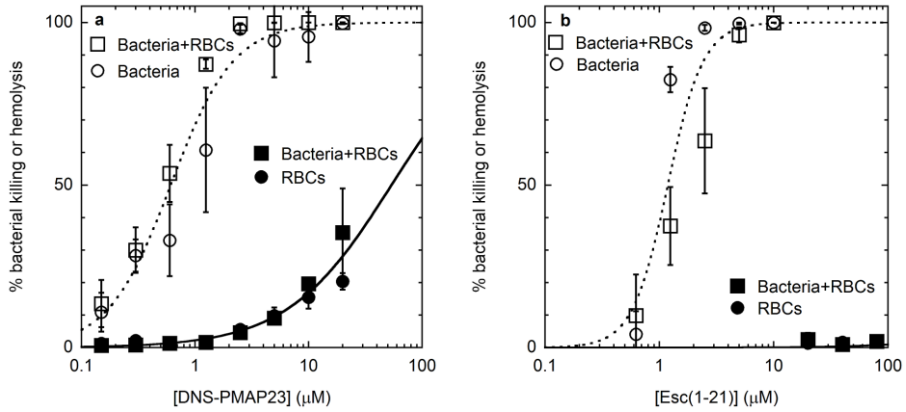

Figure 2: Bactericidal (dotted line) and hemolytic (solid line) activities of DNS-PMAP23 (a) and Esc(1−21) (b) in the presence of both bacteria and erythrocytes or of one cell type only. 4.5×10^7 *E. coli* cells/mL, 4.5×10^8 RBCs/mL

Fluorescence studies of the mechanism of action of host defense peptides

Annalisa Bortolotti [a], Valerio Santucci [a], Lorenzo Stella[a]

[a]Department of Chemical Sciences and Technologies, University of Rome Tor Vergata, 00133 Rome, Italy.

e-mail: stella@stc.uniroma2.it

Keywords: Antimicrobial peptides, peptaibols, peptidomimetics

Many bacteria are showing increasing resistance against available antibiotics. Natural host defense peptides (HDPs) are promising molecules to fight these multiresistant microbes. HDPs are usually cationic and amphipathic and show strong antimicrobial activity, killing bacteria mainly by perturbing their membranes. At the same time, they are not significantly toxic towards human cells. Due to the fact that HDPs target cell membranes, development of bacterial resistance against them is difficult.

Notwithstanding the potential of HDPs in the fight against drug resistance, the pharmaceutical application of peptides is hindered by several limitations. At the same time, the rational design of peptidomimetic molecules with the same properties of HDPs has met with limited success. One of the main reasons for these difficulties is that multiple equilibria (conformational transitions, self-assembly, water-membrane partition, insertion in the bilayer, pore formation, etc.) are involved in the interaction of HDPs with membranes (Figure 1). All these phenomena influence the peptide pore-forming activity, and any modification in peptide properties perturbs all of them to different extents.

Spectroscopic approaches, in particular fluorescence methods, are extremely powerful in the characterization of the behavior of HDPs or peptidomimetic molecules in interaction with lipid bilayers. Fluorescence spectra and lifetime measurements allow the quantification of peptide aggregation (Figure 2) and water-membrane partition (Figure 3). Quenching methods can be used to determine the depth of insertion of the peptide in the bilayer, oriented circular dichroism to investigate HDP orientation with respect to the membrane plane. Fluorophore leakage experiments allow a quantification of peptide-induced pore formation (Figure 4). Examples of these approaches, applied to HDPs (e.g. chalciporin A) or peptidomimetics, will be presented, illustrating the insights that can be obtained in the mechanisms of pore formation by the application of these methods.

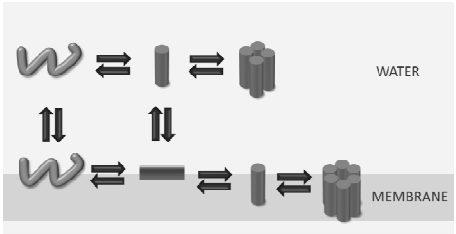

Figure 1. Scheme of equilibria involved in peptide interaction with membranes.

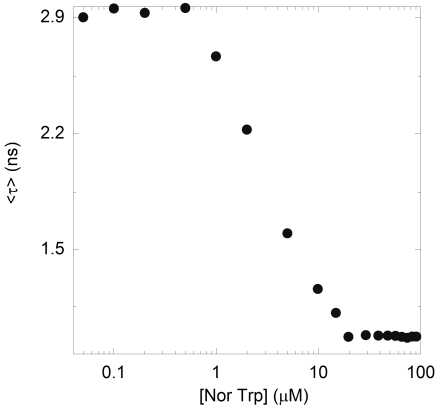

Figure 2. Effect of the aggregation of the antibacterial peptidomimetic NorTrp on its average fluorescence lifetime. The molecule is completely aggregated above 20 μM.

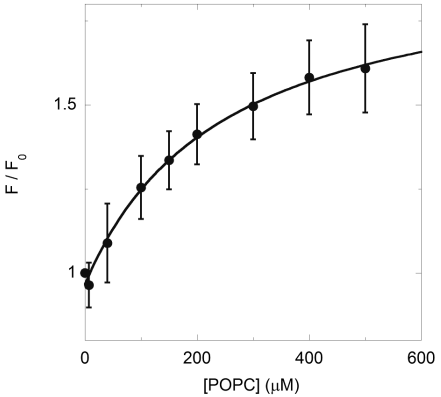

Figure 3. Water-membrane partition followed by the increase in the fluorescence intensity of Chalciporin A caused by titration with POPC liposomes

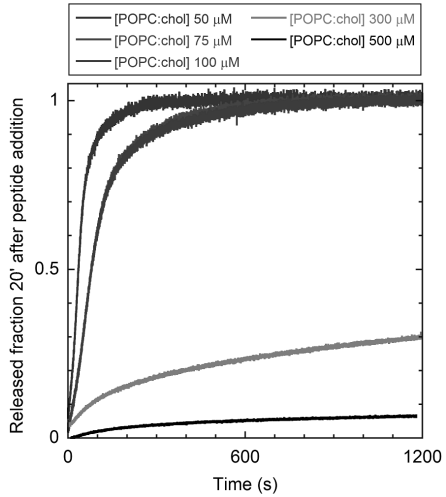

Figure 4. Kinetics of carboxyfluorescein release from POPC/cholesterol liposomes after addition of the antibacterial peptidomimetic NorTrp.